Amplitude analysis and search for CP violation with $D^0 \to \pi^+\pi^-\pi^0$ decay with Run-II data

Lanxing Li

Supervisor: Evelina Gersabeck

A dissertation submitted to the University of Manchester for the degree

of

Master of Science by Research

in the Faculty of Science and Engineering

Department of Physics and Astronomy

University of Manchester

UK

2022

Contents

This dissertation is 16,669 words in length, not including references.

List of Figures

List of Tables

Abstract

This thesis investigates the resonant structure of the Cabibbo-suppressed decay $D^0 \to \pi^+\pi^-\pi^0$, the needed theoretical approach and the relevant experimental techniques to measure the time-integrated CP asymmetries using an amplitude analysis. The measurement uses a sample of pp collisions recorded by the LHCb experiment during 2015-2018, corresponding to an integrated luminosity of 5.7 fb^{-1}. The D^0 mesons are reconstructed from prompt D^{*+} meson decaying into $D^0\pi^+$, allowing the flavour at production to be assigned from the pion charge. The selected sample contains more than 2350×10^{-3} signal events with a signal purity of about 90%, allowing the most precise amplitude modelling of this D^0 decay to date. An amplitude analysis exploiting the rich intermediate resonant structure provided by the three body phase space is performed. The magnitudes and phases for various decay channels are extracted from data using an unbinned maximum likelihood fit, from which their fractions can be inferred. The variations of the model acceptance across the phase space are also corrected from the theoretical formulation. The obtained amplitude model identifies a total of 10 intermediate resonant components and one non-resonant $\pi^+\pi^-$ S-wave component. The prominent contributions are found to be the $\rho(770)$ resonances, with fit fractions 74.28% ($\rho^+(770)$), 26.88% ($\rho^0(770)$), 40.25% ($\rho^-(770)$).

Declaration

I declare that no portion of the work referred to in the dissertation has been submitted in support of an application for another degree or qualification of this or any other university or other institute of learning.

Lanxing Li

Copyright Statement

Acknowledgements

may you always be safe and happy.

Chapter 1

Introduction

The validity of the Standard Model (SM), which is the fundamental theory describing elementary particles and their interactions, has been proven successful in decades of experiments. However, there are still phenomena the SM cannot explain well, which implies a significant gap in the theory. There is no known mechanism for the unification of gravity and the other fundamental forces. The neutrino oscillation discovered at the Super-K [1] and other neutrino detection experiments such as SNO [2] and the KamLand experiment [3], strongly rejected the massless neutrino in the SM. No candidates for dark matter have been discovered. All of these mysteries point to the new theoretical framework needed to cover the deficiencies of the SM, also known as new physics beyond the SM, which is a key direction in the field of particle physics experiments today.

Among all the phenomena the SM can not explain well, the violation of Charge conjugation and parity symmetry (CP violation) is needed to explain the dominance of matter that we observe in the universe. However, the size of CP violation in the SM is much smaller than the expected value to account for the observed matter-antimatter asymmetry, which indicates that there must be a new theory beyond the SM to predict the larger source of CP violation.

In the SM, the size of the CP violation is predicted to be tiny $\mathcal{O}(10^{-3} - 10^{-4})$ [4, 5] in the charm sector (the charm quark is the only up-type quark that can form bound states to observe the CP violation). Its theoretical computation is severely restricted

by the low-energy strong-interaction effect [6], originating from the mass region of the charmed meson, making the non-perturbative hadronic physics operative but with larger uncertainties [7]. Any new physics contribution could alter the size of CP violation, which inspires the search for CP violation in the charm sector for decades.

The lightest particle containing a charm quark is the D^0 meson. The CP violation in the charm sector has been observed in $D^0 \rightarrow hh$ (where h denotes a hadron) decays by the LHCb experiment after decades of experimental searches [6]. Its magnitude is consistent with the upper end of the SM prediction [4–12]. There is no unanimous agreement in the theory community whether the result is compatible with the SM predictions [13] or not. The large CP violation result compiles with the prediction based on the flavour SU (3) symmetry via enhancement of the penguin amplitudes [12]. The penguin diagram refers to the electroweak one-loop Feynman diagram, in which a quark change its flavour. Contributions from new particles or an additional penguin amplitude predicted by extensions of the SM can also introduce a substantial contribution to enhance the CP violation expected by the SM [14]. Thus, further measurements of other decays of charm mesons will be essential to understand the CP violation in the charm sector and help to probe new physics effect.

So far, no evidence for CP violation in multibody charm decays has been reported, and the two body decay $D^0 \rightarrow hh$ is the only charm meson decay in which CP violation has been observed at present. Thus, multibody decays have a huge potential to provide a unique probe of new physics. Firstly, multibody decays have a non-trivial phase space due to their rich resonant structure, in which the relative strong phases originating from interference between intermediate states of the decay vary significantly in different regions [15]. Considering the CP violation in decay is sensitive to the change of the strong phase, the multibody decays thus have a higher sensitivity to CP violation in local regions of phase space, compared with the phase space integrated search [16].

Singly Cabibbo suppressed (SCS) transitions $c \rightarrow uq\bar{q}$, which will be explained in Chapter 2.3, are sensitive to CP violation. The decay amplitudes contain an admixture of both leading order tree-level and penguin amplitudes, and their interference can give

18

rise to the CP violation. New physics contributions can manifest in the penguin diagrams which in turn can introduce new contributions to CP violation [4]. Considering the CP violation in $c \to uq\bar{q}$ transition is strongly suppressed in the SM, any obvious deviation from the SM predictions could signal new physics.

The three body charm decay of $D^0 \to \pi^-\pi^+\pi^0$ is a SCS decay with a rich intermediate resonant structure, which undergoes an SCS $c \to uq\bar{q}$ transition. The relevant Feynman (tree level and penguin) diagrams of the decay are illustrated in Figure 1.1. In addition to the high sensitivity to CP violation in decay and information about the strong phase difference, an amplitude analysis allows to further disentangle the contribution from CP asymmetries in mixing and to separately determine the neutral D-meson mass and lifetime differences, up to discrete ambiguities [4].
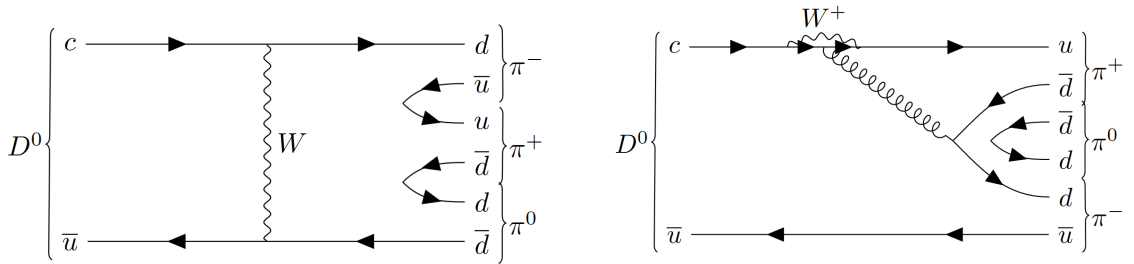
Figure. 1.1: Quark level Feynman diagrams. A colour-favoured tree diagram (left) and the penguin diagram (right) for the decay $D^0 \to \pi^-\pi^+\pi^0$.

The BaBar collaboration has performed the first amplitude analysis on $D^0 \to \pi^-\pi^+\pi^0$ using $D^{(*\pm)} \to D^0(\to \pi^-\pi^+\pi^0)\pi^\pm$ decays and a search for CP violation based on this model using $B^\pm \to D^0(\to \pi^-\pi^+\pi^0)K^\pm$ decays with a signal yield of about 170 events [17]. A search for CP asymmetry in this channel has been performed using a binned χ^2-method and the Energy Test method by the BaBar and LHCb collaborations [16, 18], respectively. Though no significant asymmetry was observed, the p-value quantifying the consistency of the data with the hypothesis of CP symmetry has been measured to a few percent [15]. The analysis presented in this thesis will be based on LHCb data collected in 2015-2018, corresponding to an integrated luminosity of $5.7\,\mathrm{fb}^{-1}$, which is a

sixty times larger data sample of signal candidates compared to the BaBar result. This will allow us to significantly reduce the uncertainties on the amplitude analysis results, and, consequently, on CP violation parameters.

This thesis describes the search for CP violation based on the amplitude analysis on the Cabibbo-suppressed decay $D^0 \to \pi^+\pi^-\pi^0$. The structure is expressed as follows. The main theory used in this analysis, mainly focusing on the CP violation and the theoretical formalism of the amplitude analysis, is discussed in Chapter 2. An overview of the LHCb detector, and the detailed description of all the subdetector systems during the Run-II period is introduced in Chapter 3. The LHCb Trigger system is also introduced as the key component of the LHCb selection framework. Chapter 4 gives a summary of the analysis method and we used in this analysis. It mainly discusses the techniques of the search for the CP violation using amplitude analysis. The analysis strategy is also discussed, combined with the introduction of the real data sample and the MC simulation sample we rely on for the analysis. The data selection is described in Chapter 5. Chapter 6 describe the amplitude fit on the $D^0 \to \pi^+\pi^-\pi^0$ decay performed by the AmpGen package to obtain a preliminary CP-averaged model. The associated systematic uncertainties is described in Chapter 7. This analysis developed during the MSc period is the first phase of the project, which will be continued as my PhD project.

Chapter 2

Theory

2.1 The Standard Model

The Standard Model is the most successful theory in particle physics which correctly predicts the classification of all known elementary particles and the fundamental interactions between them. In the SM, all elementary particles can be classified as the spin-1/2 fermions or the spin-1 or 0 bosons, where the fermions are always seen as the fundamental component of matter, and the spin-1 bosons are the mediators of the fundamental strong, weak and electromagnetic forces. The fermions can be further classified into six quarks and six leptons, while only the quarks participate in the strong interaction. The six quarks include the up, down, charm, strange, top, and bottom quarks (also known as the beauty quarks). In addition, the six leptons are the electron, muon, tau and the corresponding neutrinos. Each of them has an antiparticle with the same mass but with the opposite electric charge. The bosons consist of four spin-1 gauge bosons: gluon (for strong interactions), $W^{\pm}$, Z^0 bosons (for weak interactions), photon (for electromagnetic interactions) and one spin-0 scalar boson: the Higgs boson, which is conceived to provide the mass to the gauge bosons via the Higgs mechanism. Figure 2.1 summarises the particles of the SM along with their measured masses, charges and spins.

The six quarks and leptons can be further classified into three generations of flavours in pairs. For quarks, each generation has an up-type quark with a charge of $+\frac{2}{3}$ (up,
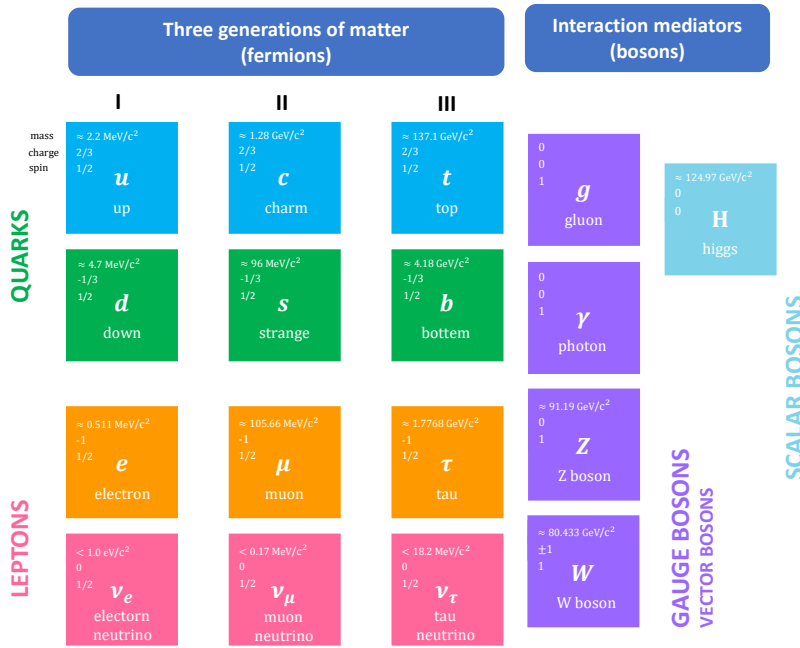
Figure. 2.1: Fundamental particles of the SM with their measured masses, charges and spins [14].

charm, top) and a down-type quark with a charge of $-\frac{1}{3}$ (down, strange, bottom). For leptons, one generation consists of a lepton with charge of -1 (electron, muon, tau) and a corresponding uncharged neutrino (ν_e, ν_μ, ν_τ). Besides flavours, each quark also carries a colour charge to undergo strong interactions and bind into hadrons. Hadrons are composite subatomic particles such as mesons (consisting of a quark-antiquark pairs) and baryons (consisting of three quarks). Hadron decays provide access to various key parameters of the SM, such as the constraints on the Cabibbo-Kobayashi-Maskawa (CKM) six-quark flavour-mixing matrix or the Yukawa sector of the SM, and therefore play a important role in particle physics.

The SM has been built on a series of symmetry groups. Except for the electric, flavour and colour charge conservation constrained by the gauge invariance of the SM Lagrangian, three key discrete symmetries also exist in the SM: Parity (P), Charge (C) and Time (T) symmetry. The symmetry under the parity transformation, which reverses any spatial coordinates, is referred to as P symmetry. Charge symmetry requires

symmetry under charge conjugation which transforms particles into antiparticles. A time symmetry is a symmetry under time reversal, which reverses any motion-related vectors. Charge conjugation and parity symmetry (CP symmetry) describes the invariance of the physics system after the transformation of particles into their antiparticles with inverted spatial coordinates.

2.2 Quark flavour transitions

In the SM, the CP violation is introduced by a complex phase in the CKM matrix describing the quark mixing:

$$V_{CKM} = \begin{pmatrix} V_{ud} & V_{us} & V_{ub} \\ V_{cd} & V_{cs} & V_{cb} \\ V_{td} & V_{ts} & V_{tb} \end{pmatrix}. \tag{1}$$

The mass eigenstate of a quark is a linear combination of the flavour eigenstates, which means it can mix via the weak interaction. An up-type quark q can transition to a down-type quark q$'$ mediated by a $W^{\pm}$ boson via the weak interaction $q \to W^{\pm} q'$. The CKM matrix then describes the coupling factors $V_{qq'}$ of two quarks.

Considering the CKM matrix is a unitarity matrix describing the transitions between three quark generations, there are only four independent degrees of freedom. One of the common parametrisations for the CKM matrix is described based on three mixing angles $(\theta_{12}, \theta_{23}, \theta_{13})$ and one complex phase (δ):

$$V_{CKM} = \begin{pmatrix} c_{12}c_{13} & s_{12}s_{13} & s_{13}e^{-i\delta} \\ -s_{12}c_{23} - c_{12}s_{23}s_{13}e^{i\delta} & -c_{12}c_{23} - s12s_{23}s_{13}e^{i\delta} & s_{23}c_{13} \\ s_{12}s_{23} - c12c_{23}s_{13}e^{i\delta} & -c_{12}s_{23} - s12c_{23}s13e^{i\delta} & c_{23}c_{13} \end{pmatrix}, \tag{2}$$

where $s_{ij} = sin\theta_{ij}$ and $c_{ij} = cos\theta_{ij}$. The CP violation in the SM is introduced by the complex phase of δ. It is also common to describe the CKM matrix in terms of the

Wolfenstein parametrisation based on the real parameters A, λ, ρ and η:

$$V_{CKM} = \begin{pmatrix} 1 - \frac{\lambda^2}{2} & \lambda & A\lambda^3(\rho - i\eta) \\ -\lambda & 1 - \frac{\lambda^2}{2} & A\lambda^2 \\ A\lambda^3(1 - \rho - i\eta) & -A\lambda^2 & 1 \end{pmatrix}. \tag{3}$$

With this parametrisation, the hierarchy structure of the CKM matrix driven by the expansion factor λ, which is constrained to be $\lambda \approx 0.22$ [14], can be demonstrated. The off-diagonal elements in the CKM matrix are strongly suppressed compared to the diagonal elements, such as $|V_{us}| \approx 1 - \lambda < |V_{ud}| \approx \lambda$. The transition of $u \to s$ is governed by $|V_{us}|$, and that of $u \to d$ is governed by $|V_{ud}|$. This indicates the suppression of the flavour-changing process, also known as the Cabibbo suppression. In particular, the first leading order tree-level Feynman diagram of $D^0(\to \pi^-\pi^+\pi^0)$ shown in Figure 1.1 proceeds via the transition of $u \to d$ and $c \to d$. Its amplitude is then determined by the CKM matrix element of $|V_{ud}||V_{cd}| \approx \lambda$. This is the definition of a SCS decay.

The unitarity of the CKM matrix, $V_{CKM}^\dagger V_{CKM} = 1$, constrains the product of off-diagonal matrix elements to cancel out. This leads to construction of unitarity triangles in the complex plane. One of the common triangles is shown in Figure 2.2, which derives from the quark flavour transition involving b and d quarks:

$$V_{ud}V_{ub}^* + V_{cd}V_{cb}^* + V_{td}V_{tb}^* = 0. \tag{4}$$

Three CKM angles of the unitarity triangle are then defined as

$$\alpha = arg(-\frac{V_{td}V_{tb}^*}{V_{ud}V_{ub}^*}), \quad \beta = arg(-\frac{V_{cd}V_{cb}^*}{V_{td}V_{tb}^*}), \quad \gamma = arg(-\frac{V_{ud}V_{ub}^*}{V_{cd}V_{cb}^*}). \tag{5}$$

The unitarity triangle related to the charm decays is shown in Figure 2.3, which derives from the $c \leftrightarrow u$ transition. The charm triangle has an extreme shape with a tiny
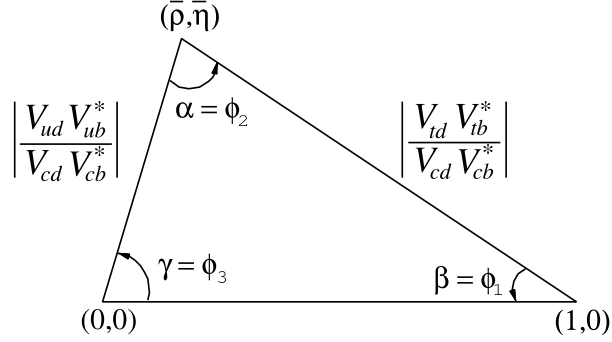
Figure. 2.2: Sketch of the best known unitarity triangle [14].

CKM angle [19], which can be expressed as

$$\left|\frac{V_{cd}V_{ud}^*}{V_{cs}V_{cs}^*}\right| = 1 + \mathcal{O}(\lambda^4), \left|\frac{V_{cb}V_{ub}^*}{V_{cs}V_{us}^*}\right| = \mathcal{O}(\lambda^4), \tag{6}$$

$$\gamma_D = arg\left(-\frac{V_{cd}V_{ud}^*}{V_{cs}V_{us}^*}\right) \simeq A^2\lambda^4\eta \simeq 6.3 \times 10^{-4}. \tag{7}$$
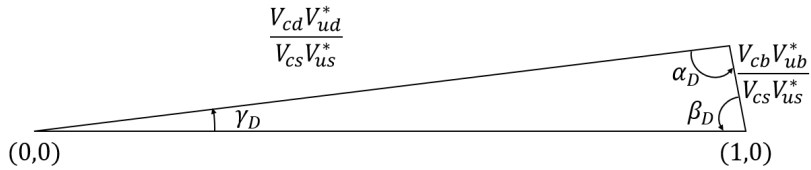
Figure. 2.3: Sketch of the unitarity triangle related to the charm decays.

2.3   Mixing of neutral mesons

The time-dependent transition from a neutral particle to its antiparticle is referred to as mixing in the neutral meson system. This process is governed by a flavour-changing neutral current (FCNC). However, as the neutral current interaction mediated by the Z boson constrains the flavour conservation, the leading order FCNC processes are not allowed in the SM. The higher order transitions involving loop diagrams of multiple W bosons, also named box diagrams, are then required. One of the examples for charm mesons is shown in Figure 2.4. The neutral meson mixing has been well studied in the kaon and beauty sectors. However, in the charm sector we have down-type quarks

25

involved in the loop. The contribution from the down and strange quarks mostly cancel each other out due to their similar magnitude but opposite sign. This is also known as the Glashow-Iliopoulos-Maiani (GIM) mechanism [20]. Moreover, the contribution of virtual quarks in the loop suffers from the suppression by the mass factor of $\frac{m_q^2}{m_W^2}$ and the Cabibbo suppression in the flavour changing interaction. This means that the only contribution from the bottom quark is also strongly suppressed. Therefore, the charm meson mixing is highly suppressed compared to neutral kaons and B mesons, and requires higher experimental precision. Considering new virtual particles beyond the SM may contribute to the mixing, any sizable enhancement from the SM prediction would therefore be a hint for new physics contribution beyond the SM.
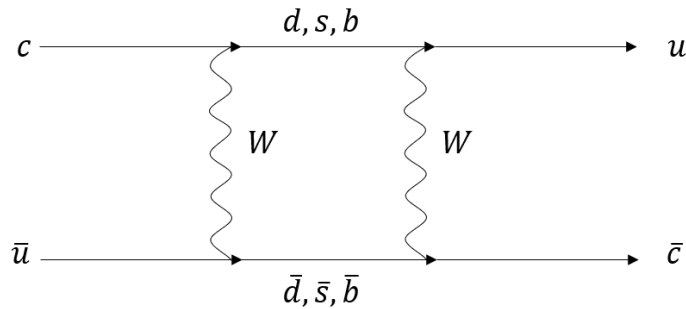
Figure. 2.4: Feynman box diagram for the D^0 meson mixing transition.

Due to the mixing, the mass eigenstate of the charm meson is then a linear combination of the flavour eigenstates. Taking the D^0 meson as a example, we can express the physics state (Hamiltonian eigenstate) $|D_{1,2}\rangle$ in terms of the flavour eigenstates $|D^0\rangle$ and $|\bar{D}^0\rangle$ under CPT symmetry:

$$|D_{1,2}\rangle = p\,|D^0\rangle \pm q\,|\bar{D}^0\rangle\,, \tag{8}$$

where the complex coefficients p and q satisfy the normalisation condition $|p^2| + |q^2| = 1$. Using the effective Hamiltonian $\mathcal{H} = \mathcal{M} - \frac{i}{2}\Gamma$ describing the relevant interaction, where $\mathcal{M}$ and Γ represent the mass and decay term of mesons, the corresponding eigenstates are

$$\mathcal{H}\,|D_{1,2}\rangle = \lambda_{1,2}\,|D_{1,2}\rangle\,, \tag{9}$$

where the eigenvalues $\lambda_{1,2} = m_{1,2} = i\Gamma_{1,2}/2$, $m_{1,2}$ and $\Gamma_{1,2}$ are the masses and decay widths of the eigenstates, respectively. The time evolution of such a state is then given by

$$|D_{1,2}(t)\rangle = e^{-im_{1,2}t - \Gamma_{1,2}\frac{t}{2}} |D_{1,2}(0)\rangle , \tag{10}$$

where the $|D_{1,2}(0)\rangle$ represents the initial state of the meson. Combined with Equation 8, we can then derive the time evolution of the flavour eigenstates, which are directly relevant to the decay, as

$$|D^0(t)\rangle = \frac{1}{2p}\left[(e^{-im_1 t - \Gamma_2 t/2} + e^{-im_2 t - \Gamma_2 t/2})p |D^0\rangle + (e^{-im_1 t - \Gamma_1 t/2} - e^{-im_2 t - \Gamma_2 t/2})q |\bar{D}^0\rangle)\right]. \tag{11}$$

We can introduce two dimensionless quantities x and y, which are also known as the mixing parameters, to simplify the equation:

$$x = \frac{\Delta m}{\Gamma}, \quad y = \frac{\Delta\Gamma}{2\Gamma}, \tag{12}$$

where $\Delta m = m_2 - m_1$ and $\Delta\Gamma = \Gamma_2 - \Gamma_1$ represent the mass and width differences, respectively, and $\Gamma = \frac{\Gamma_1 + \Gamma_2}{2}$ represents the average width. Using the mixing parameters, we can then describe the time evolution Equation 11 as

$$|D^0(t)\rangle = f_+(t) |D^0\rangle + \frac{q}{p}f_-(t) |\bar{M}^0\rangle , \tag{13}$$

where

$$f_\pm(t) = \frac{1}{2}e^{-imt - \Gamma t/2}(e^{(ix+y)\Gamma t/2} \pm e^{-(-ix+y)\Gamma t/2}), \tag{14}$$

where m is defined as the average mass $m = \frac{m_1 + m_2}{2}$. The time evolution of $\bar{D}^0$ can be equivalently written as

$$|\bar{D}^0(t)\rangle = \frac{p}{q}f_-(t) |D^0\rangle + f_+(t) |\bar{D}^0\rangle . \tag{15}$$

Using the orthogonality on the eigenstates and Equations 11 and 15, we can express the measurable probability of initially pure D^0 and $\bar{D}^0$ states at time t as

$$P(D^0 \to D^0, t) = P(\bar{D}^0 \to \bar{D}^0, t) = |f_+(t)|^2 = \frac{1}{2}e^{-\Gamma t}[cosh(y\Gamma t) + cos(x\Gamma t)] \qquad (16)$$

$$P(D^0 \to \bar{D}^0, t) = \left|\frac{q}{p}\right|^2 |f_-(t)|^2 = \frac{1}{2}\left|\frac{q}{p}\right|^2 e^{-\Gamma t}[cosh(y\Gamma t) - cos(x\Gamma t)] \qquad (17)$$

$$P(\bar{D}^0 \to D^0, t) = \left|\frac{p}{q}\right|^2 |f_-(t)|^2 = \frac{1}{2}\left|\frac{p}{q}\right|^2 e^{-\Gamma t}[cosh(y\Gamma t) - cos(x\Gamma t)], \qquad (18)$$

which shows the process of mixing between the flavour eigenstates. The mass difference Δm is responsible for the sinusoidal mixing frequency, while the width difference $\Delta\Gamma$ is related to the decay time. The mixing parameters relevant to the common neutral mesons are summarised in Table 2.1, while the illustration of their time evolution calculated from Equations 16, 17 is shown in Figure 2.5. The tiny scale of the mass and width differences of charm meson compared with the other mesons can explain the strong suppression of its mixing.
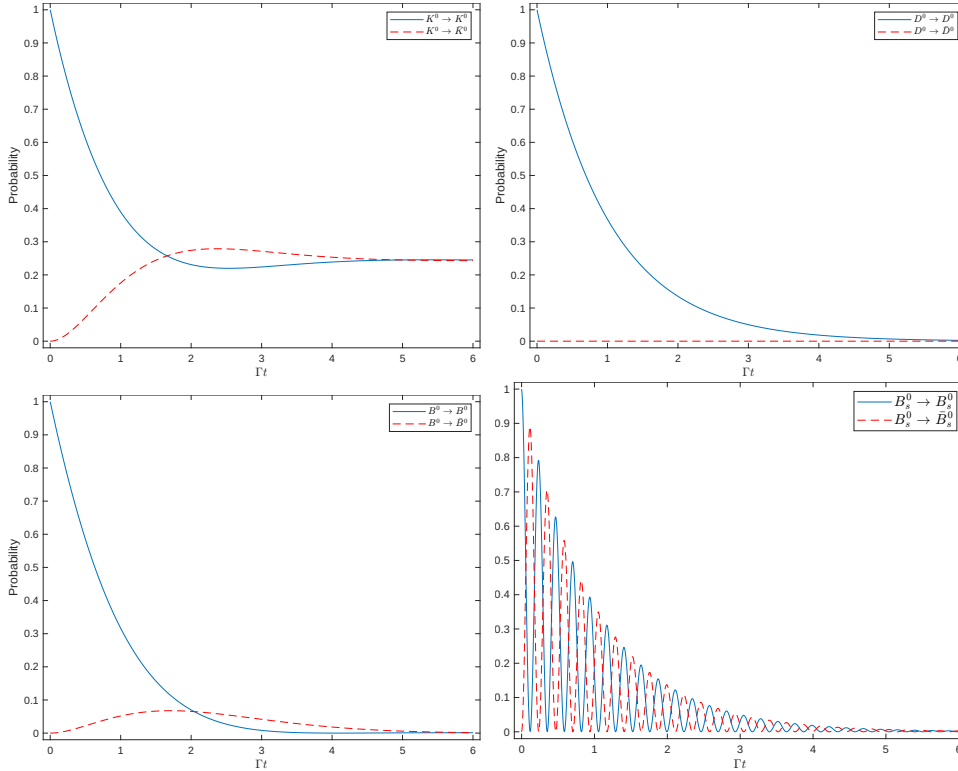
Figure. 2.5: Time evolution of four neutral mesons.

Table. 2.1: Mixing parameters for K^0, D^0, B^0 and B_s^0 mesons, taken from Ref [14]. The mass and width are taken from Ref [19].

Parameters	K^0	D^0	B^0	B_s^0
m [GeV]	0.49761(1)	1.86484(5)	5.27965(12)	5.36688(14)
Width [ps^{-1}]	0.005594(2)	2.438(9)	0.658(2)	0.660(3)
τ [ps]	89.54(4) [K_S^0] 51160(210) [K_L^0]	0.4101(15)	1.519(4)	1.509(4)
x	0.946(2)	0.0041(5)	0.769(4)	26.89(11)
y	-0.996(1)	0.0062(6)	0.001(5)	-0.062(4)

2.4 CP violation

As the fundamental discrete symmetries in the SM, the CP symmetry is seen to be conserved in the electromagnetic and strong interaction. However, since the first observation of Parity violation in the weak interaction in the Wu experiment [21], it has been proved that the weak charged currents couple only to the left-handed fermions and right-handed anti-fermions in the SM, which maximally violate C and P symmetries individually. The combined CP operator transforms a left-handed fermion into a right-handed anti-fermion and hence avoid the individual violation, so the weak interactions were generally believed to be invariant under the CP transformation. However, this turned out to be wrong after the discovery of CP violation in the kaon system [22].

The significant excess of matter over anti-matter in the currently observed universe requires a relative excess of baryons produced in the interactions of fundamental particles in the early universe [23, 24]. One necessary condition for this matter-antimatter asymmetry is CP violation. It has been postulated as one of three independent conditions, known as the Sakharov conditions [25] for such a scenario. To form the dominance of matter in the current universe, a process resulting in the imbalance of particles over antiparticles is necessary. The CP symmetry will allow to rebalance the system, and hence must be violated.

The CP symmetry is believed to be exact in the strong interaction but is violated in the weak interaction. However, the reason for CP symmetry to be conserved in the strong interaction is still unclear and regarded as an unsolved problem, known as the strong CP

problem. The CP violation is well established in decays of kaon [14,22] and beauty [14,26] meson decays, but its known scale is insufficient by several orders of magnitude to explain the baryon asymmetry. The huge discrepancy in the prediction suggests that there may be an additional CP violation contribution originating from new physics beyond the SM. The precise measurement of CP violation in leptons (neutrino), bosons (Higgs) and other mesons (charm) therefore is crucial for discovering new physics [5, 27, 28].

The operator of combined CP symmetries will transform a particle into its antiparticle and vice-versa. In the case of charm mesons, the relevant transformation related to the flavour eigenstate $|D^0\rangle$ and $|\bar{D}^0\rangle$ is then written as

$$
\begin{aligned}
CP\,|D^0\rangle &= \eta_{CP}\,|\bar{D}^0\rangle\,, \\
CP\,|\bar{D}^0\rangle &= \eta_{CP}^*\,|D^0\rangle\,,
\end{aligned}
\tag{19}
$$

where η_{CP} is the relevant phase factor of the CP operator, $\eta_{CP} = e^{i\xi_{CP}/2}$, and is often set to $\xi_{CP} = 0$. The eigenstates of CP $|D_\pm\rangle$ can then be defined as

$$
CP\,|D_\pm\rangle = \pm\,|D_\pm\rangle = \frac{1}{\sqrt{2}}(|D^0\rangle \pm |\bar{D}^0\rangle),
\tag{20}
$$

which coincides with the Hamiltonian eigenstate of the D^0 meson if $p = q$, which means the CP symmetry in mixing.

The CP violation in the SM can be CP violation in decay (also known as direct CP violation), or mixing of the particles or the interference between them (known as indirect CP violation). The CP violation in the decay originates from the asymmetries between the decay rate of a particle to a final state f and the decay rate of its antiparticle to the conjugated final states $\bar{f}$. This asymmetry is different for each decay model. For a D^0 meson decaying into a final state f, the direct CP violation can be expressed as

$$
\Gamma(D^0 \to f) \neq \Gamma(\bar{D}^0 \to \bar{f}),
\tag{21}
$$

which therefore represents the asymmetry of decay amplitudes as

$$\Gamma(D^0 \rightarrow f) = |\mathcal{A}(D^0 \rightarrow f)|^2. \tag{22}$$

The amplitude for a charm meson decaying into a final state f can be defined as [29]

$$\mathcal{A}_f = \langle f | \mathcal{H} | D^0 \rangle = \sum_i A_i e^{i\delta_i} e^{i\phi_i}, \tag{23}$$

and for the conjugated process,

$$\bar{\mathcal{A}}_{\bar{f}} = \langle \bar{f} | \mathcal{H} | \bar{D}^0 \rangle = \sum_i A_i e^{i\delta_i} e^{i-\phi_i}, \tag{24}$$

where the index i correspond to the individual amplitude, δ is the strong phase originating from the strong interaction and thus preserves the invariance under CP conjugation, and ϕ is the weak phase entering through the relevant CKM matrix elements which is inverted under CP conjugation. The strong phase is generally different for every amplitude and strongly depends on the available phase space for the multibody decay. As the weak phase originates from the CKM matrix elements associated with the quark transition, it can also change for the different amplitudes. Thus, the direct CP violation requires more than one amplitude to contribute to the decay process with the same final state, which can be shown in terms of the two relevant amplitudes as

$$|\mathcal{A}(D^0 \rightarrow f)|^2 - |\bar{\mathcal{A}}(\bar{D}^0 \rightarrow \bar{f})|^2 \propto sin(\phi_1 - \phi_2)sin(\delta_1 - \delta_2), \tag{25}$$

which also requires a non-zero weak and strong phase difference between the two amplitudes. As the strong phase varies across the phase space, the measurement of the direct CP violation is usually based on the analysis of the amplitudes of the relevant decay modes, which will be discussed further in the following chapters.

The CP violation occurring in the mixing of the neutral meson originates from the rate asymmetry of the transitions of a meson to its antimeson, which is independent of the decay mode of the particle. Considering the related probability of the transitions in

Equations 17 and 18, the violation occurs if $|\frac{q}{p}| \neq 1$, which also means the noncoincidence between the Hamiltonian eigenstates and the CP eigenstates, as shown in Equation 20.

The third type of CP violation originates from the interference between the decay and mixing of neutral mesons. This kind of CP violation can also be represented as the decay rate asymmetry between a meson decaying into the final state directly and its CP conjugate decaying after undergoing a mixing process. For the D^0 meson, the process is

$$\Gamma(\bar{D}^0 \to f, t) \neq \Gamma(D^0 \to f, t), \tag{26}$$

where both $\bar{D}^0$ and D^0 are time-dependent flavour eigenstates. Reviewing the time evolution of the flavour eigenstates and the definition of the decay amplitudes shown in Equation 13 and Equations 23 and 24, the time-dependent decay amplitude for $D^0(t)$ is

$$\mathcal{A}_f \equiv \langle f| \mathcal{H} |D^0\rangle = f_+(t)\mathcal{A}_f + \frac{q}{p} f_-(t)\bar{\mathcal{A}}_f, \tag{27}$$

$$\bar{\mathcal{A}}_{\bar{f}} \equiv \langle \bar{f}| \mathcal{H} |\bar{D}^0\rangle = \frac{p}{q} f_-(t)\bar{\mathcal{A}}_f + f_+(t)\mathcal{A}_f. \tag{28}$$

The magnitude of CP violation in the interference can therefore be characterised by the relative weak phase between the mixing part of $\frac{q}{p}$ and the amplitude ratio $\frac{\bar{\mathcal{A}}_f}{\mathcal{A}_f}$. In general, this can be summarised by introducing a complex variables $\lambda_f = \frac{q}{p} \frac{\bar{\mathcal{A}}_f}{\mathcal{A}_f}$. The CP violation in the interference for the CP eigenstate can then be expressed as

$$arg(\lambda_f) \neq 0. \tag{29}$$

2.5 Amplitude analysis

Based on Fermi's golden rule, the decay rate for an n-body decay from an initial particle can be expressed as

$$\Gamma = \frac{1}{2m_0} \int |\mathcal{A}|^2 d\phi_n, \tag{30}$$

where $\mathcal{A}$ represents the sum of all individual decay amplitudes contributing to the process and $d\phi_n$ is the relevant n-body phase space, which is defined as

$$d\phi_n = (2\pi)^{4-3n} \delta^4 \Big(p_0 - \sum_{i=1}^{n} p_i \Big) \prod_{i=1}^{n} d^4 p_i \delta(p_i^2 - m_i^2), \qquad (31)$$

where m_0 and p_0 are the mass and four-momentum of the initial particle, respectively, and m_i and p_i are the relevant kinematical variables for the final state particles. Though the phase space has $4n$ possible degrees of freedom originating from n final-state particles, many of them are not independent. In total, 3n-7 Lorentz-invariant degrees of freedom are required to describe the kinematics of the decay, given constraints from conservation of four-momentum and spacial orientation invariance as a result of spinless particles in the initial and final state. One of the common settings for the phase space observables is the invariant mass combinations of the final state particles, which is more relevant to the properties of the decay chain and able to provide a more intuitive description for the measurement.

In general, an n-body decay of $a \rightarrow nb$ can proceed through many intermediate resonances or scattering processes, which contribute to different individual decay amplitudes related to the phase space. All of these amplitudes exist and overlap with each other, causing a rather complex kinematical distribution of the final state. To study such a decay process, a model encoding different intermediate states with their specific shape and magnitudes is then needed to best fit the real distribution from the experimental data. The description of these complex amplitude variations over the phase space refers to an amplitude model for the corresponding decay [30], which is used to distinguish all the contributions from various intermediate states.

In this analysis, we mainly focus on the three body decay $D^0 \rightarrow \pi^-\pi^+\pi^0$, which receives contributions from various possible intermediate resonance decays or processes such as $\rho^\pm \rightarrow \pi^\pm\pi^0$ and complicated scattering processes such as isoscalar $\pi\pi \rightarrow \pi\pi$ scattering. The dynamics of such decay model $D^0 \rightarrow abc$ can be then fully described by the two squared invariant mass combinations of final state particles m_{ab}^2 and m_{ac}^2, as all involved particles are pseudoscalar mesons. The two-dimensional distribution of these

variables, the so-called Dalitz Plot [14], is introduced to visualise the decay dynamics. An example illustration for a Dalitz plot is shown in Figure 2.6. Except for the kinematic boundaries constrained by the momentum conservation, any of the characteristics in the Dalitz plot will reveal information on the dynamics of the decay process. Specifically, a uniform distribution is seen if the amplitude of the direct three body decay is constant. Any deviation from that then originates from the contribution from the intermediate process including resonances or other states. Their distributions depend on both the spin of the resonance and the phase difference between two interfering amplitudes. The total amplitude for a multibody decay with different intermediate states is then described by a sum over all the individual amplitudes, which is written based on the Equations 23 and 24,
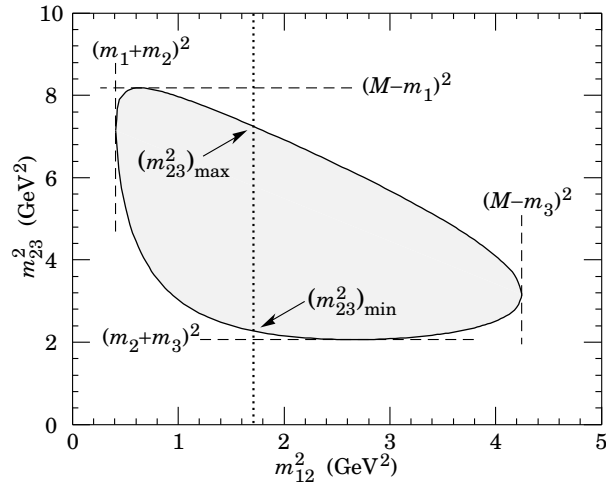
Figure. 2.6: Illustration of a Dalitz plot for a three body final state [14].

$$\mathcal{A}(m_{ab}^2, m_{ac}^2) = a_{NR}e^{i\delta_{NR}(m_{ab}^2,m_{ac}^2)}e^{i\phi_{NR}} + \sum_r a_r(m_{ab}^2, m_{ac}^2)e^{i\delta_r(m_{ab}^2,m_{ac}^2)}e^{i\phi_r}, \qquad (32)$$

where a_{NR} refers to the magnitudes of the non-resonant amplitude, and a_r corresponds to that of the resonant intermediate state r. δ_{NR} (δ_r) and ϕ_{NR} (ϕ_r) refer to the strong and weak phases of the non-resonant amplitude (resonant amplitude), respectively. As the local density in the Dalitz plot is proportional to the squared total amplitudes,

the density distribution over the Dalitz plot represent the variation of the strong phase difference as shown in Equation 32. We can obtain the relative strong phase difference between various interfering amplitudes via an amplitude analysis based on the Dalitz plot, which is key for the measurement of the direct CP violation. The total amplitude for
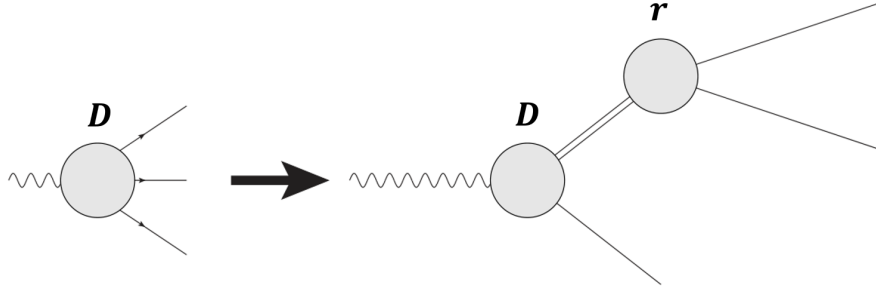
Figure. 2.7: Illustration of the isobar model description of the process $D \to abc$. The figure is taken from Ref [32].

a multibody decay can be modelled using various quasi-independent two body processes. Such formalism is known as the isobar model [31] and these two body processes are usually named isobars. The isobar model is typically used as the formalism of the three body decay, which is illustrated in Figure 2.7. In such formalism, each decay process is associated with an intermediate resonance r which will decay to the two final state particles, forming linear superpositions of the two body amplitudes as $D \to ar(r \to bc)$. Any higher-order topologies describing the rescattering process, which refers to the interaction between the remnant particle with the products of the isobar, are assumed to be negligible in the isobar model. The amplitude for an isobar can be then written as

$$\mathcal{A}_r(m_{ab}^2, m_{ac}^2) = F_D^{(L)}(q, q_0) Z_L(m_{ab}^2, m_{ac}^2) \mathcal{T}_r(m_{bc}) F_r^{(L)}(p, p_0), \tag{33}$$

where the form factors $F_D^{(L)}$ and $F_r^{(L)}$ describe the production and decay of a resonance and L is the relative orbital angular momentum between the resonance r and its accompanying particle a. In a normal case where the spin of a is 0, L is then the spin of the resonance. In Equation 33, q (p) is the momentum of the transfer, defined as the three-momentum of either final state particle in the rest frame of the decaying particle D (r),

and q_0 (p_0) is then the three-momentum at the pole mass of the D meson (resonance). In our case, where the resonance decays via $r \to bc$, q can be expressed as

$$q^2 = \frac{\sqrt{[m_r^2 - (m_a^2 + m_b^2)^2][m_r^2 - (m_a^2 - m_b^2)^2]}}{2m_r}. \tag{34}$$

In Equation 33, Z_L is the spin factor for a resonance with spin L, which is the coherent sum over all the polarisation states for the intermediate amplitudes related to the phase space. Finally, T_r is the propagator describing the dynamics of the resonance decay, which is dependent on the phase space variables m_{bc} as $r \to bc$.

The form factors $F^{(L)}$ are used to describe the realistic centrifugal barriers for the final state particles decaying from the resonance. An amplitude is dampened at a large momentum transfer or higher angular momentum. Furthermore, as the angular momentum is limited by the magnitude of momentum transfer, decay particles with lower momentum will not have sufficient angular momentum to account for the resonance spin [33]. The Blatt-Weisskopf functions [34] $F^{(L)}$ are then used to weight the related amplitudes accounting for such spin-dependent effect, which has been normalised to give $F^{(L)} = 1$ for $q = q_0$. The Blatt-Weisskopf form factors generally used are given in Table 2.2.

Table. 2.2:   Blatt-Weisskopf coefficients for the first three values of the angular momentum L between the decay products. The parameter r is the radius of the resonance.

L	$F^{(L)}(q, q_0)$
0	1
1	$\sqrt{\dfrac{1+q_0^2 r^2}{1+q^2 r^2}}$
2	$\sqrt{\dfrac{(q_0^2 r^2 - 3)^2 + 9q_0^2 r^2}{(q^2 r^2 - 3)^2 + 9q^2 r^2}}$

The Zemach formalism [35] is used to describe the spin factors accounting for the angular distribution of the final state particles with spin-0. The formalism uses the pure spin tensors to avoid the explicit construction of the spin wave functions and is only appropriate for the decays of spinless particles into spinless final states. For final state particles with non-zero spin, the helicity formalism [36] is further required. The general

expression for the Zemach function is

$$Z_L = (-2|p_b||p_a|)^L P_L(cos\theta_{ab}), \tag{35}$$

where θ_{ab} is the angle between the momentum of two final state particles a and b in the rest frame of the resonance and P_L is the Legendre polynomial of order L. For scalar resonances, no polarisation vectors associated with the decay vertices exists and thus the angular distribution is $Z_0 = 1$. The other angular distributions typically used from the Zemach formalism can be expressed as

$$L = 1 : Z_1 = -2\vec{p}_b \cdot \vec{p}_a, \tag{36}$$

$$L = 2 : Z_2 = \frac{4}{3}[3(\vec{p}_b \cdot \vec{p}_a)^2 - (|\vec{p}_b| \cdot |\vec{p}_a|)^2]. \tag{37}$$

We can also express the angular distribution based on the Lorentz invariant Dalitz variables. The sum over all the polarisation states can be derived using the spin-sum rule. For the vector intermediate state, this can be written as

$$\sum_\lambda \epsilon_\lambda^{*\mu} \epsilon_\lambda^\nu = -g_{\mu\nu} + \frac{q^\mu q^\nu}{m^2}, \tag{38}$$

where λ specifies the helicity state and $g_{\mu\nu}$ is the metric tensor and ϵ^μ and ϵ^ν are the relevant polarisation vectors. For the tensor intermediate state, the sum can be more complicated, and is calculated to be [37]

$$\sum_\lambda \epsilon_\lambda^{*\mu\nu} \epsilon_\lambda^{\alpha\beta} = \frac{1}{2}(T^{\mu\alpha}T^{\nu\beta} + T^{\mu\beta}T^{\nu\alpha}) - \frac{1}{3}T^{\mu\nu}T^{\alpha\beta}, \tag{39}$$

where

$$T^{\mu\nu} = g^{\mu\nu} + \frac{q^\mu q^\nu}{m^2}. \tag{40}$$

After inserting the spin-sum expression into the matrix element of the decay amplitudes and sum over all the repeated indices, the angular distribution can be summarised as

$$L = 0 : Z_0 = 1, \tag{41}$$

$$L = 1 : Z_1 = m_{ab}^2 - m_{ac}^2 - \frac{(m_D^2 - m_a^2)(m_b^2 - m_c^2)}{m_{bc}^2}, \tag{42}$$

$$L = 2 : Z_2 = Z_1^2 - \frac{1}{3}\left[m_{bc}^2 - 2(m_D^2 + m_a^2) + \frac{(m_D^2 + m_a^2)^2}{m_{bc}^2}\right]\left[m_{bc}^2 - 2(m_b^2 + m_c^2) + \frac{(m_b^2 + m_c^2)^2}{m_{bc}^2}\right], \tag{43}$$

which can be now parameterised in the amplitude fit.

The propagator $\mathcal{T}_r$ describes the dynamics of the resonance decay. One of the common formulas used for the propagator is the relativistic Breit-Wigner (RBW) propagator [38] written as

$$\mathcal{T}_r(m) = \frac{1}{(m_0^2 - m^2) - im_0\Gamma(m)}, \tag{44}$$

where m_0 is the pole mass of the resonance, Γ is the related width, which is expressed as

$$\Gamma(m) = \frac{\Gamma_0 q m_0}{q_0 \sqrt{s}}\left(\frac{q}{q_0}\right)^{2L} F^{(L)}, \tag{45}$$

and Γ_0 is the width of the resonance. There are also other propagators used in the analysis, which will be introduced in detail in Chapter 6.

Chapter 3

The LHCb detector

The Large Hadron Collider beauty (LHCb) detector [39] is a forward-arm detector specifically designed for the precision measurements of CP violation and rare decays of beauty and charm hadrons. It is one of the main experiments at the Large Hadron Collider (LHC). The LHC is a synchrotron with a circumference of 27 km at the European Organization of Nuclear Research (CERN), located at the French-Swiss border. The main goal of the LHC is fundamental particle physics research using p-p collision data including precision tests of the SM and also the search for new physics, conducted by the four main collaborations ATLAS [40], CMS [41], LHCb [39] and ALICE [42]. The LHCb has three periods of operations until now, with the first one (Run-I) from 2010-2012 collecting p-p collisions at the LHCb experiment with an integrated luminosity of 3 fb^{-1} at a centre-of-mass energy ($\sqrt{s}$) of 7 TeV for 2011 and 8 TeV for 2012, the second period (Run-II) from 2015-2018 collecting 5.7 fb^{-1} p-p collisions at centre-of-mass energy of 13 TeV, and the third period (Run-III) operating until the end of 2025 at a centre-of-mass energy of 13.6 TeV. The analysis discussed in the thesis is based on the data set collected during Run-II.

In addition to the precise measurement of CP violation and rare decays such as FCNC processes, LHCb has also performed extensive studies of lepton universality, searches for exotic hadron states and also particle candidates beyond the SM. As a forward single-arm spectrometer, LHCb is optimised to have a pseudorapidity range from $1.9 < \eta < 4.9$,

where the pseudorapidity is defined using the radial angle θ of a particle relative to the beam axis:

$$\eta \equiv -ln\left[tan\left(\frac{\theta}{2}\right)\right]. \tag{46}$$

The pseudorapidity range corresponds to an angular coverage of $10 < \theta < 300$ mrad, which accounts for only 4% of the full solid angle. Such optimisation is motivated by the corresponding production method of the beauty and charm quarks. As the primary production of these heavy quarks is gluon-gluon fusion, which has a significant asymmetry on the momentum, the heavy quarks pair will be highly boosted in the direction of the beam axis. Thus, a quarter of the heavy quarks will be produced in the coverage region of the LHCb detector despite its small angular acceptance. The relevant angular distribution for the $b\bar{b}$ quarks in terms of production cross-section is shown in Figure 3.1.
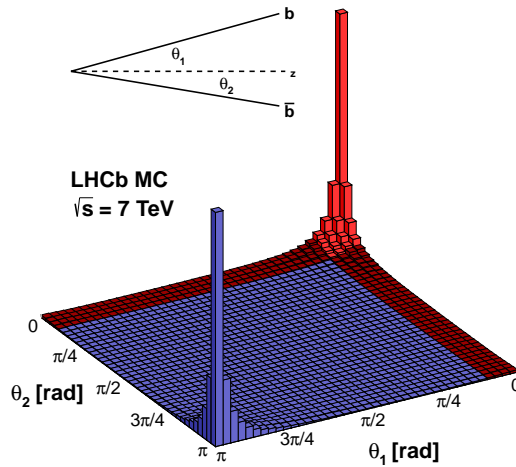
Figure. 3.1: Angular distribution of $b\bar{b}$ production at $\sqrt{s} = 7$ TeV in the LHCb detector, where the detector acceptance is shown by the red shaded area [43].

Figure 3.2 shows the cross-section of the LHCb detector. The subdetectors are: Vertex Locator (VELO), the Ring Imaging Cherenkov (RICH), a tracking system on both sides of a dipole magnet, the calorimeter system and the muon system. Each subdetector

has different design goals and detection ranges and is responsible for detecting and collecting the physical information of various particles produced at the LHCb detector. We will introduce the design and function of each subdetector in the following chapters.
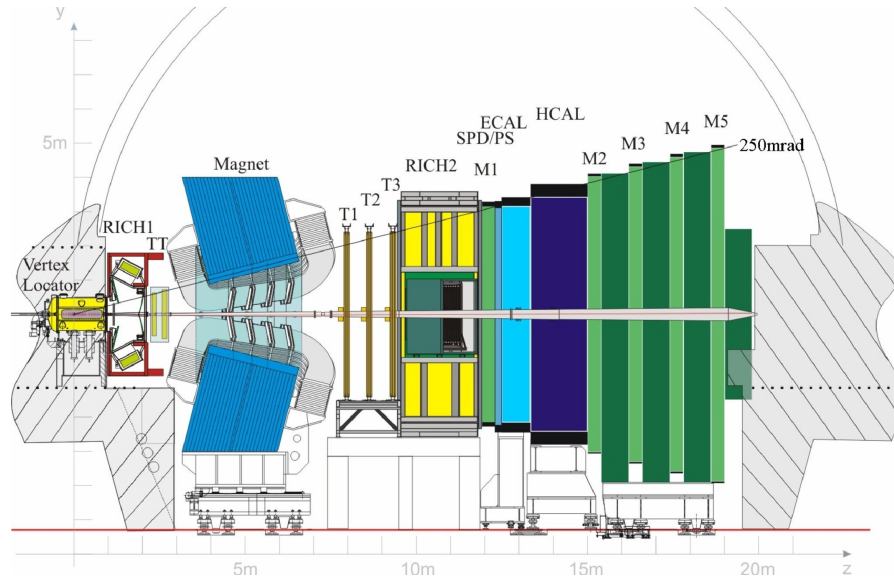
Figure. 3.2: Diagram of the LHCb detector, showing the different subdetector systems [39]

.

3.1 Vertex Locator

The VELO is the closest detector surrounding the interaction point in the LHCb experiment, which is designed to reconstruct the primary vertex (PV) of the p-p collision and also the displaced secondary vertices (SV) from the decays of long-lived hadrons containing b or c quarks. The latter is a distinctive characteristic for the reconstruction of the hadrons.

The VELO consists of 21 pairs of silicon modules placed along the beam direction, each of which contains two sensors, with the first sensor called the R sensor measuring the radius coordinate to the beam axis and the other one called the ϕ sensor used to measure the azimuthal direction [44]. The VELO is unique due to its feature of being retractable from the beam axis. The general distance between the modules and the

41

beamline is set to be 7 mm but can increase to 35 mm during the initial injection of the beams which is used to protect the detector from unstable beams. The detailed cross section of the VELO silicon sensors is shown in Figure 3.3.
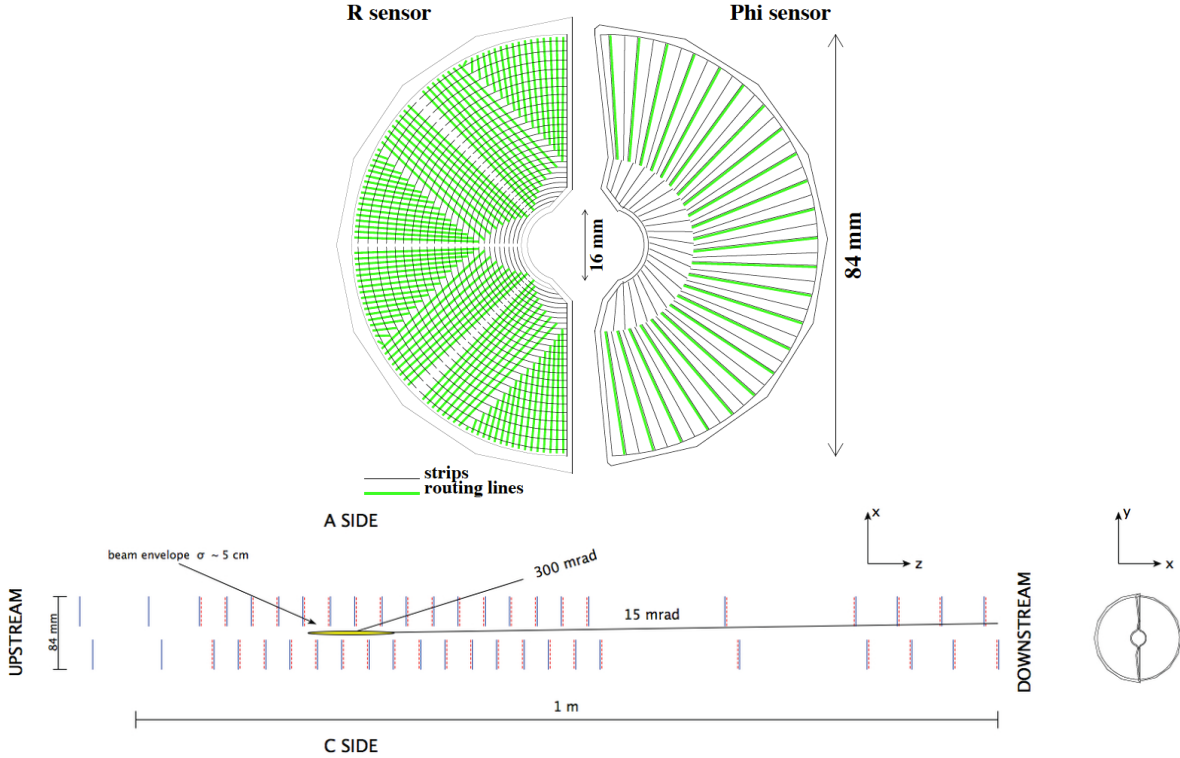
Figure. 3.3: A schematic of the LHCb VELO; the R and ϕ sensors and dimensions are shown in the top and the positions of the modules with respect to the beam axis are shown in the bottom [44].

The VELO has a good PV resolution of a 13 μm in the transverse plane and 71 μm along the beam direction, which provides a precise measurement of the impact parameter (IP) defined as the shortest distance between the extrapolated track and the PV. The excellent resolution of the IP is crucial for the separation of the tracks originating at the SV from tracks originating at the PV as the typical flight distance of the long-lived hadrons is $\mathcal{O}(1)$ cm, which makes the IP an important parameter used in most of the LHCb analyses. In LHCb, the resolution of IP is measured to be $[15 + 29/p_T(GeV/c)]\mu$m [45] and is shown in Figure 3.4, which also shows the PV resolution as a function of track multiplicity.
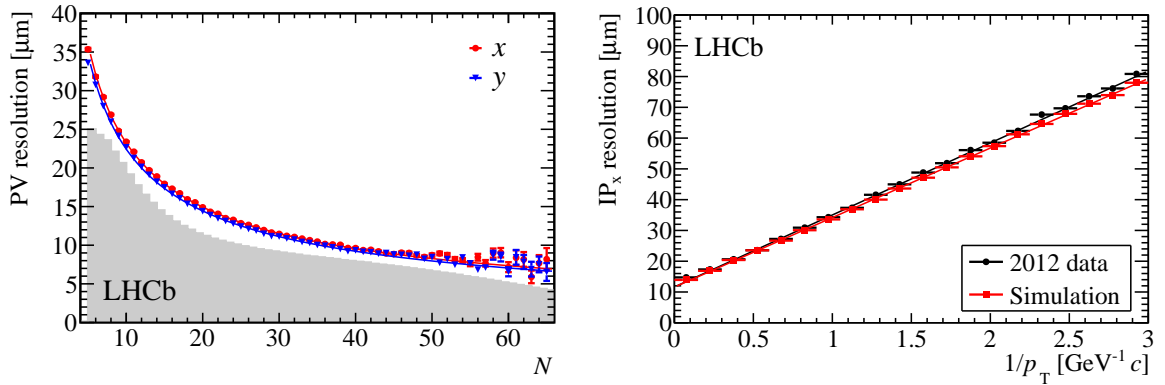
Figure. 3.4:   Performance plots for the VELO subdetector. Left: Position resolution as a function of the number of tracks (N) included in the vertex fit. The x (y) resolution are shown in red (blue) lines. The histogram shows the distribution of N per reconstructed primary vertex for all events that pass the high level trigger. Right: Impact parameter resolution in the x direction. Both figures are reproduced from Ref [46].

3.2   Tracking system

The tracking system consists of the Tracker Turicenis (TT), the T1-T3 tracking stations and a dipole magnet with an integrated magnetic field strength of 4 Tm between them, used to bend tracks in the horizontal plane. Via the reconstruction of the trajectories of the charged particles passing through the tracking detector, the system can determine the momentum of the particle with a resolution between 0.5% to 1% depending on the track's momentum [47]. The configuration of the polarity of the magnet can change at regular intervals from the magnet up with positive polarity to the magnet down with a negative polarity and vice versa. Combined with the fact that oppositely charged particles bend in the opposite directions for a given polarity, this can mitigate the possible biases from the detector asymmetries.

The TT, as the first part of the tracking system located upstream of the magnet, consists of four layers in an $x - u - v - x$ layout, each with a row of silicon strip sensors, covering the full acceptance of the LHCb detector. The two outer layers x are aligned vertically whereas the two inner layers u and v are rotated by a small angle of $-5°$ and $5°$, respectively, to maximise spatial resolution. The readout strips differ in size because of the high hit occupancy in the inner region of the detector, which allows a single hit

resolution of approximately 50 μm. Figure 3.5 shows the layout of one silicon strip layer.
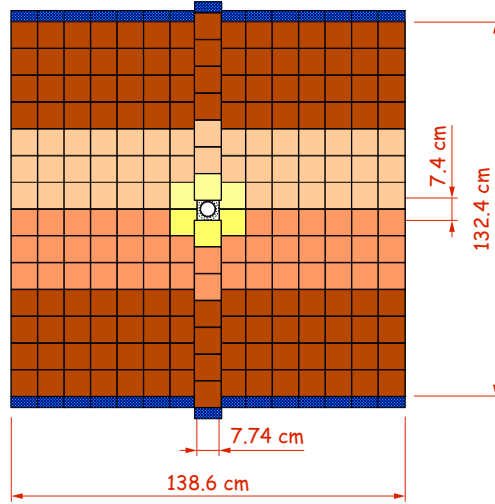
Figure. 3.5:   Layout of the first detection layer of the TT station [48].

The T1-T3 tracking system consists of two subsystems with different detector technologies: the inner region made up of silicon microstrip detectors with long readout strips known as the Inner Tracker (IT) and the larger outer region made up of straw-tube drift chambers known as the Outer Tracker (OT). The IT consists of four layers of silicon strip sensors located in the innermost region with the same setting in an $x - u - v - x$ layout as the layers of the TT. The OT is a drift-time detector designed with an array of straw-tube drift chambers, filled with a mixture of argon (70%), carbon dioxide (28.5%) and oxygen (1.5%) to guarantee a fast drift time below 50 ns. The gas mixture can ionise when a charged particle passes through the tubes. The reconstruction of the charged particles' trajectory is then determined from the drift time of the drift electrons ionising along the track. The OT covers a large angular acceptance with 300 mrad in the horizontal direction and 250 mrad in the vertical direction. It has an excellent performance with an average single-hit efficiency of about 99.2% and a spatial resolution of about 200 μm [49].

3.3 Particle identification

The separation of the different species of charged particles is done by the particle identification (PID) system. The information from several subdetector systems is combined to reach the final identification. In LHCb, the main component of the PID system are two Ring Imaging Cherenkov (RICH) detectors, with one upstream from the magnet called RICH1 and the other one downstream from the magnet called RICH2. The operation principle of the RICH detectors is detecting the Cherenkov radiation of the charged particles. A cone of photons emitted from the Cherenkov radiation is produced when a charged particle passes through the medium with a velocity faster than the speed of light in the medium. The opening angle of the cone θ_c, known as the Cherenkov angle, is then measured. It is related to the velocity of the charged particles as

$$cos\theta_c = \frac{1}{n\beta}, \qquad \beta = \frac{v}{c}, \tag{47}$$

where n is the refractive index of the material. Combined with the momentum measured by the tracking system and additional information from the calorimeters and muon system, the identification of the particle can then be done with a likelihood that the particle candidate is identified as a given type. Figure 3.6 shows the Cherenkov angle distribution for the mass hypotheses of different particles. Two RICH detectors in LHCb cover a whole range of track momentum from 1-100 GeV/c, each optimised with a specific range via a different selection of the radiator medium. The RICH1 is optimised for the low momentum range of charged particles of approximately 1-60 GeV/c, which uses C_4F_{10} as the radiator in Run-II period. The RICH2 then covers the high momentum range from 15 GeV/c to 100 GeV/c, using a CF_4 radiator [39].

3.4 Calorimeter system

The calorimeter system is used to measure the energies and positions of the hadrons, electrons and photons, and provides particle identification based on the energy loss of
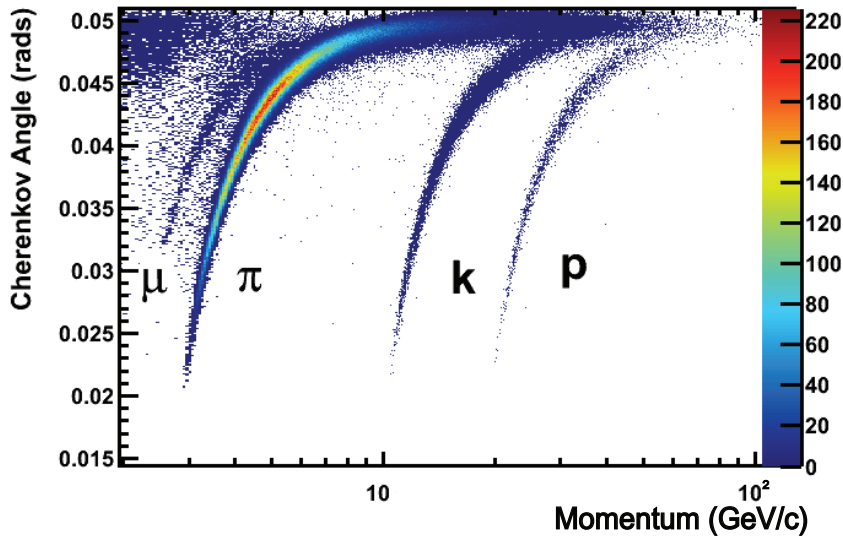
Figure. 3.6: Reconstructed Cherenkov angle as a function of track momentum in the C_4F_{10} radiator for different mass hypotheses of particles [46].

these particles. The general principle of the LHCb calorimeters is the detection of the scintillation light emitted from the ionising radiation when particles traverse the detector, which is then collected as the signal by photomultiplier tubes (PMTs). In LHCb, the calorimeter system consists of four subdetectors built along the beam axis. All four detectors are optimised for the identification of specific particle species. The Charged particle densities increase by two orders of magnitude when getting closer to the beam pipe [39]. To follow such variations, the Scintillator Pad Detector (SPD), Preshower (PS) and Electromagnetic Calorimeter (ECAL) are further divided into several regions with different cell sizes. The size decreases with decreasing distance to the beam pipe because the innermost region close to the beam is subject to the highest multiplicity. The SPD and PS built foremost downstream are made up of a wall of scintillating pads, where the light is collected via wavelength-shifting fibres (WLS) grooved inside. A lead converter of about 15 mm is interspaced between them. The SPD can discriminate between charged and neutral particles as only the former ones deposit energy in it, while the PS can detect electromagnetic showers and measure the energy. The two detectors combined can provide a good separation between electrons, photons and pions. The ECAL next

to the PS is composed of alternating layers of absorber (lead) and scintillator. It has a prominent thickness of 25 radiation lengths to fully contain the electromagnetic shower from a high-energy photon. It can measure the energy of lighter particles, such as electrons and photons, and provide identification for them. The energy resolution for a given cell is $\frac{\sigma(E)}{E} = \frac{(9.0\pm0.5)\%}{\sqrt{E}} \oplus (0.8 \pm 0.2)\%$ [39]. The segmentation can be seen in Figure 3.7. The Hadronic Calorimeter (HCAL) built furthest downstream has the same alternating design as the ECAL with iron absorbers, while the thickness is only 5.6 interaction lengths limited by the available space in the experimental setting. It has a similar segmentation as the other calorimeters, which is shown in Figure 3.7. The HCAL can measure the energy of hadrons with a worse energy resolution of $\frac{\sigma(E)}{E} = \frac{(69\pm5)\%}{\sqrt{E}} \oplus (5 \pm 2)\%$ [39], compared to the ECAL. However, it is still crucial for the hardware trigger where it is used to provide a quick identification of the purely hadronic final states.
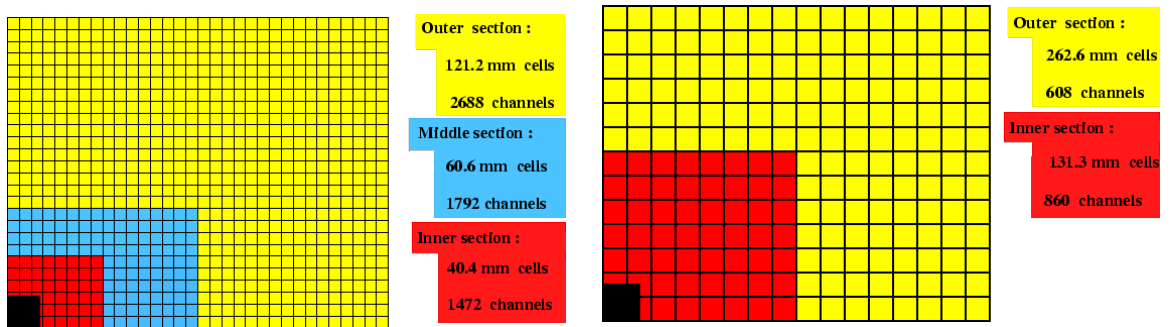
Figure. 3.7: Calorimeter cells segmentation of the SPD , PS , and ECAL (left) and the HCAL (right) [50].

3.5 Muon system

The muon system provides the main particle identification of the muons as well as a good estimation of its transverse momentum. The system is built furthest from the interaction point. This is motivated by the fact that a large fraction of the muons are minimum ionising particles, which means they can mostly pass through the whole

detector with limited energy loss. The muon system consists of five stations with one upstream of the calorimeter system called M1 and others named M2-M5 situated downstream. All stations are equipped with multi-wire proportional chambers (MWPC) filled with a mixture of argon, carbon dioxide and CF_4, except for the inner part of the M1 equipped with Gas Electron Multiplier (GEM) subject to the highest hit occupancy from radiation. The M2-M5 stations are also interleaved with 80 cm thick iron absorbers to select muons, as they are the only particle that can highly penetrate with minimum ionisation. A muon with a minimum momentum of about 10 GeV/c is expected to pass through all the stations [51]. Each station is divided into four regions called R1-R4 with increasing distance from the beam axis. Their segmentation show a scale in the ratio of 1:2:4:8. This geometry ensures the channel occupancies in each region are then comparable [52]. Figure 3.8 shows a diagram of the muon system. As only a small part of other species of particles can penetrate the entire detector, the muon system can provide both a positive identification of muons and a negative identification of the other particles if the tracks are not associated with a hit in the muon system. The information obtained from the muon system is then combined with the RICH and calorimeter system to improve particle identification. The M1-M3 stations also have a good spatial resolution along the bending plane, and are used to calculate the transverse momentum of the muon candidate with a resolution of 20%. The estimation of the transverse momentum is extensively used in the muon trigger described in Chapter 3.6.

3.6   LHCb Trigger system

The LHC's proton bunch crossing rate during Run-II is 40 MHz, which is impossible and unnecessary for the experiment to record as not all events are of interest. The LHCb trigger system is designed to reduce the rate to kHz and only save those data relevant to our physics programme to storage. The trigger system is composed of three separate levels: a hardware Level-0 (L0) trigger and software High-Level triggers (HLT1, HLT2). Each trigger is implemented using a combination of readouts from different detectors
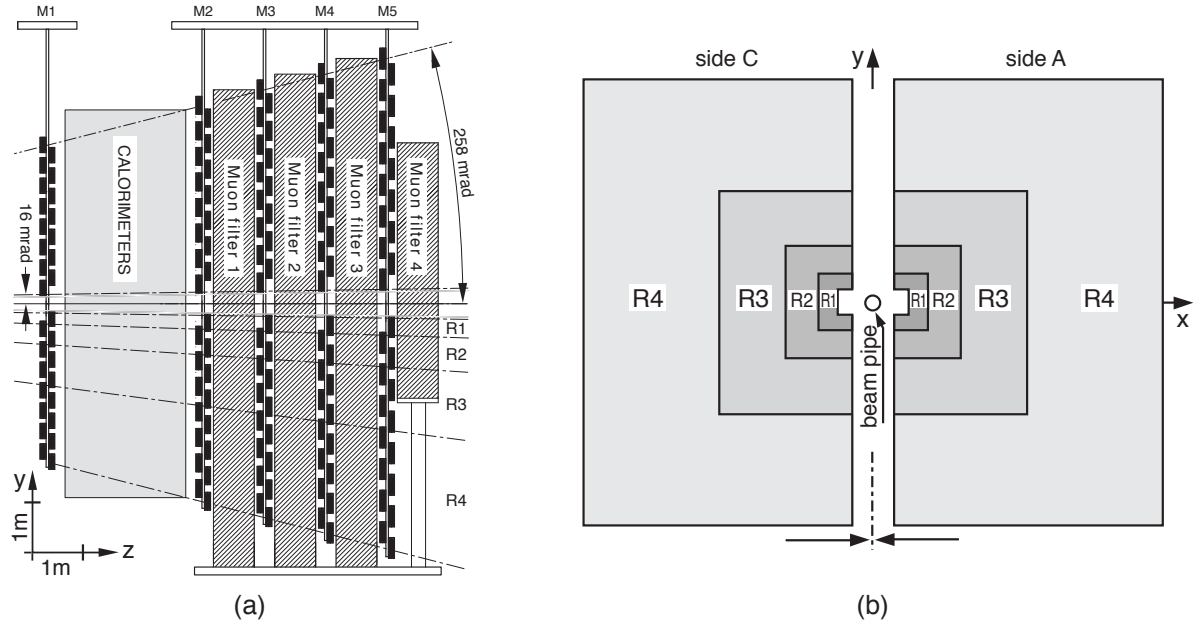
Figure. 3.8: (a): The sideview of the LHCb muon system including five stations M1-M5 divided into regions R1-R4. (b): The layout of the station with four regions [53].

and has specific selection criteria. Figure 3.9 shows a summary of the LHCb data flow through the trigger system in Run-II.

The L0 trigger is designed to reduce the LHC raw proton bunch crossing rate of 40 MHz to a manageable level of 1 MHz for the later stages, where only some of the detectors are used in consideration of speed. It mainly uses the calorimeter system to provide signatures of tracks with large transverse energy, which are typically produced from the decay of heavy flavoured particles. It also uses the muon system to provide a first determination of the transverse momentum of muons.

The HLTs in LHCb are software triggers run on the CPU farm of Event Filter Farm (EFF), which is designed to reduce the data rate of 1 MHz from the L0 trigger to the kHz level based on the full detector information. In the first stage, HLT1 uses the tracking system to perform a partial track reconstruction. The VELO information is also used to reconstruct the PV, where at least 5 VELO tracks are used to construct it and the IPs for the other tracks are also measured. Tracks with high IP are typically the signature of particles originating from the SV, which include the decay of hadrons we are interested

LHCb 2015 Trigger Diagram

40 MHz bunch crossing rate

**L0 Hardware Trigger : 1 MHz
readout, high E_T/P_T signatures**

| 450 kHz | 400 kHz | 150 kHz |
| $h^{\pm}$ | $\mu/\mu\mu$ | e/γ |

Software High Level Trigger

**Partial event reconstruction, select
displaced tracks/vertices and dimuons**

**Buffer events to disk, perform online
detector calibration and alignment**

**Full offline-like event selection, mixture
of inclusive and exclusive triggers**

12.5 kHz (0.6 GB/s) to storage

Figure. 3.9: The scheme for the LHCb trigger system during the Run-II data taking
period [54].

in. The HLT1 also uses the muon system to perform a fast muon identification of single
or dimuon events. The data rate after the HLT1 stage reduces to about 40 kHz. The
second stage, HLT2 will perform a full selection of the event based on all the available
particle identification and reconstruction of tracks. It includes both the exclusive criteria
dependent on the particular requirements of a given analysis and the inclusive criteria
from the general characteristics of decay products. The output rate after the HLT2 is
about 10 kHz, which is then written to disk and used for further offline analysis.

Events written to disk after the trigger selection will be processed with a real-time
calibration and alignment of the full detector, which includes the reconstruction of all
tracks and vertices. In addition, many loose offline preselection processes, known as
stripping, which consists of a range of different dedicated selections, will be applied
to each event. Each of the stripping processes represents a particular decay channel.
The dedicated selection criteria, known as stripping lines, perform the centralised offline
selection using the Worldwide LHC Computing Grid (WLCG) [55]. After all the steps

described above, the events are ready for an offline analysis.

Chapter 4

Analysis method

The search for local CP violation in multibody decays can be broadly separated into model-independent and model-dependent approaches, where the model provides a description of all contributing amplitudes to the decay. In a model-independent approach, the overall decay picture is considered without reliance on the amplitude model. The search for CP violation is based on measuring asymmetries in regions of phase space of the decay regardless of the origin, which has the advantage that the sensitivity does not rely on the detailed understanding of the underlying decay dynamics. On the other hand, the CP violation in a specific decay amplitude could be diluted below the analysis sensitivity, which is calculated from the whole phase space. The selection of the binning scheme in the binned method also constrains the sensitivity of CP violation. In general, the bins are distributed nonuniformly based on the initial assumed amplitude model to ensure the regions with higher sensitivity are selected appropriately. The sensitivity of CP violation is diluted by bins with too large sizes, while bins with too small sizes have limited statistics to measure CP violation.

In contrast, in a model-dependent approach, the search for CP violation is based on a thorough understanding of the decay dynamics based on the amplitude model, where the decay is described as the sum of individual resonant and nonresonant amplitudes, as well as the interference between them. Any CP-violating asymmetries for specific decay paths can be directly measured via the variance between two CP conjugates. In our

analysis, we will make use of an amplitude analysis method to search for CP violation, which is described below.

The total amplitudes for neutral D^0 and $\bar{D}^0$ meson decaying into multibody final states can be written as (repeated from Equation 32)

$$\mathcal{A}(m_{ab}^2, m_{ac}^2) = a_{NR}e^{i\delta_{NR}(m_{ab}^2, m_{ac}^2)}e^{i\phi_{NR}} + \sum_r A_r(m_{ab}^2, m_{ac}^2)e^{i\delta_r(m_{ab}^2, m_{ac}^2)}e^{i\phi_r}, \qquad (48)$$

$$\bar{\mathcal{A}}(m_{ab}^2, m_{ac}^2) = \bar{a}_{NR}e^{i\delta_{NR}(m_{ab}^2, m_{ac}^2)}e^{-i\phi_{NR}} + \sum_r \bar{A}_r(m_{ab}^2, m_{ac}^2)e^{i\delta_r(m_{ab}^2, m_{ac}^2)}e^{-i\phi_r}, \qquad (49)$$

where δ and ϕ represent the strong and weak interaction phase, respectively. The CP symmetry constrains $\mathcal{A} = \bar{\mathcal{A}}$, which means the phase space of D^0 and $\bar{D}^0$ is mirrored. We can combine these two amplitudes and develop a "CP-averaged" model based on their simultaneous dependence on the phase space, which is blind to any possible CP violation effects. In the case of the decay $D^0 \to \pi^+\pi^-\pi^0$, we can express the Dalitz variables as $m_{ac} = m_{\pi^-\pi^0}$, and $m_{bc} = m_{\pi^+\pi^0}$ for D^0 and $m_{ac} = m_{\pi^+\pi^0}$ and $m_{bc} = m_{\pi^-\pi^0}$ for $\bar{D}^0$ and $m_{ab} = m_{\pi^-\pi^+}$ in both cases.

Due to the rich intermediate resonant structure in the phase space, the amplitude fitting requires many tests on each possible resonance and their shapes with associated uncertainties. A preliminary model from the BaBar collaboration [17] is used as the starting point, while the final model is determined on the LHCb data itself after multiple iterations. The data-driven technique is also used to improve the parametrisation of amplitudes, which is discussed in Chapter 6. The full amplitude fit is based on a software package developed at LHCb called AmpGen [56]. The validity has been fully tested and verified against other well-known fitters in other amplitude analysis in LHCb [57, 58].

As the CP violation requires non-zero weak and strong phase difference between two amplitudes, any asymmetries can directly influence the phase space of two CP conjugates differently, causing $\mathcal{A} \neq \bar{\mathcal{A}}$. Thus, after the CP averaged model is finalised, we can split the combined data sample in two, for D^0 and $\bar{D}^0$ candidates, and perform separate amplitude analyses with these sub-samples. We can then parameterise the CP

violation with the average modulus $\overline{|a_r|}$, the modulus asymmetry $A_{|a_r|}$, the average phase of $\overline{arg(a_r)}$ and phase difference $\Delta arg(a_r)$ defined as [59]

$$\overline{|a_r|} = \frac{|a_r|_{D^0} + |a_r|_{\bar{D}_0}}{2}; \qquad A_{|a_r|} = \frac{|a_r|_{D^0} - |a_r|_{\bar{D}^0}}{|a_r|_{D^0} + |a_r|_{\bar{D}^0}}, \tag{50}$$

$$\overline{arg(a_r)} = \frac{arg(a_r)_{D^0} + arg(a_r)_{\bar{D}_0}}{2}; \qquad \Delta arg(a_r) = \frac{arg(a_r)_{D^0} - arg(a_r)_{\bar{D}^0}}{2}, \tag{51}$$

where $|a_r|$ and $arg(a_r)$ are the relevant coordinates (modulus and phase) of the complex amplitude r, which is extracted from the individual fit of two sub-samples. We can also express the normal coordinates for each amplitude in terms of the CP violation parameters as

$$|a_r|_{D^0} = \overline{|a_r|}(1 + A_{|a_r|}); \qquad\qquad arg(a_r)_{D^0} = \overline{arg(a_r)} + \Delta arg(a_r), \tag{52}$$

$$|a_r|_{\bar{D}^0} = \overline{|a_r|}(1 - A_{|a_r|}); \qquad\qquad arg(a_r)_{\bar{D}^0} = \overline{arg(a_r)} - \Delta arg(a_r). \tag{53}$$

These CP violation parameters can be measured directly from a simultaneous amplitude fit on two sub-samples, which takes both samples into consideration and thus minimises the sum of the two negative log-likelihoods.

Instead of the CP parameters, the information on the CP violation can be obtained additionally from the fit fractions of each amplitude, which refers to the relative component of each amplitude and will be described detailed in Chapter 6.3. The asymmetry can be written as

$$A_{\mathcal{F}_r} = \frac{\mathcal{F}_r^{D^0} - \mathcal{F}_r^{\bar{D}^0}}{\mathcal{F}_r^{D^0} + \mathcal{F}_r^{\bar{D}^0}}, \tag{54}$$

where $\mathcal{F}_r^{D^0}$ and $\mathcal{F}_r^{\bar{D}^0}$ refer to the fit fractions for amplitude r in the D^0 and $\bar{D}^0$ samples, respectively.

In an amplitude analysis, the detector effects, including the efficiencies and the resolution, should be accounted for. There is a variation in the acceptance for each event due to the detector geometry, imperfect reconstruction of the particle and customised

selection criteria including stripping, trigger and offline selection. This will lead to a deviation of the kinematic distributions of the decay with respect to their true distributions. This needs to be corrected for in our amplitude analysis, also known as the phase space acceptance correction. This main correction will be obtained with the simulation sample generated for the signal decay. Furthermore, decays with similar kinematics to the signal channel, or random combination of particles from the underlying p-p interaction, can form a non-negligible background component after all the selection criteria are applied. The signal/background discrimination is vital for our amplitude analysis. The details of the efficiency correction and background suppression will be described in Chapter 5.

The analysis strategy can be summarised as follows. The flavour-tagged D^0 meson is reconstructed by selecting $D^{*+} \to D^0 (\to \pi^- \pi^+ \pi^0)\pi^+$ decays of promptly produced D^{*+} mesons, where the charge of the soft π^+, named due to its relatively small momentum, is used to tag the D^0 meson flavour at production. A positively charged soft pion detected means the D^0 is produced and a negatively charged soft pion detected means the $\bar{D}^0$ is produced. All events are required to pass the LHCb trigger selection criteria at first, and then specific stripping lines to choose the particular physics channel. To effectively separate signal from background, we then apply different selection criteria to the data samples. All of the selections are built on constraints on the relevant kinematic variables of the final state particles. Separate multivariable analysis (MVA) based classifiers are developed to minimise the background contributions, where S-weight (signal weight used to extract the pure signal distribution) calculated with the sPlot technique [60] is used. The sPlot technique is a statistical method which can reweight a data set and separate it into its signal and background components. This separation does not rely on the selection criteria applied, which means there is no need to sort events into different categories. The procedure mainly relies on the analysis of a probability density function (PDF) describing the total data sample with different components. In our analysis, this PDF is obtained via a binned maximum likelihood fit on the Δm distribution, where the S-weight corresponding to the pure signal or background components is then

calculated, of which the sum equals one [60]. The fit will be described in detail in Chapter 5.4. The weight is directly calculated from a mass fit of the data sample using the sPlot technique [60]. With a relatively pure signal sample, we can then perform an amplitude analysis of the phase space of the final state to search for CP violation in each amplitude contribution. A CP-averaged amplitude model will be developed at first to best describe all possible amplitudes contributing to the $D^0 \to \pi^-\pi^+\pi^0$ decay. Then, the signal candidate sample will be split into two flavours D^0 and $\bar{D}^0$ with the help of the soft pion tag. The $\bar{D}^0$ and D^0 sub-samples will be fitted simultaneously with the same CP-average model, and each amplitude of the model will then be compared. The CP violation could be diluted in different parts of the phase space but can be observed in specific amplitudes. Thus, a significant difference between the magnitudes and phases of each amplitude in the two sub-samples would indicate the existence of CP violation. This thesis will focus on developing a CP-averaged amplitude model. The separation of the flavoured sample and the search of the CP violation based on the simultaneously fit will be done in the future.

The data used in this analysis is collected during the Run-II period. The detailed numbers of events for each year in different magnet configurations after passing the stripping line requirements are given in Table 4.1.

Table. 4.1: The number of reconstructed $D^0 \to \pi^-\pi^+\pi^0$ candidates in data samples filtered by the stripping line in different years and magnet polarities.

| Year/Polarity | $D^0 \to \pi^-\pi^+\pi^0$ | | Luminosity $\int \mathcal{L}dt$ $[fb^{-1}]$ |
	Merged	Resolved	
2015 MagUp	566,436	16,425,192	0.122
2015 MagDown	708,842	22,550,090	0.162
2016 MagUp	4,666,880	105,610,065	0.775
2016 MagDown	4,920,805	124,837,389	0.825
2017 MagUp	5,033,764	131,460,430	0.820
2017 MagDown	5,273,950	137,125,239	0.862
2018 MagUp	8,514,805	168,959,408	1.101
2018 MagDown	7,937,461	158,187,000	1.024

In addition to the data sample, several simulation samples, which include a description of the detector geometry and its response, are also utilised in this analysis to better

understand the detector effects and obtain the correction coefficiencies. This is based on Monte Carlo (MC) simulation and done via the LHCb simulation framework called Gauss [61]. It consists of a generation phase describing the generation of the p-p collisions and the decay of its product particles, followed by a simulation of the tracking and other physics processes of the particles in the detector. The underlying p-p collision and the hadronisation of its valence quarks are simulated by the PYTHIA package [62]. The decay of the generated hadrons is simulated by the EvtGen package [63], which will make sure that all the particles decay into a specified channel in which we are interested. The detailed amplitude model is supplemented to EvtGen to constrain the specific kinematics of the decay. There are also some generation level requirements applied before the simulation, which can remove those events outside the acceptance range of the detector or produced with kinematics out of interest, and thus sufficiently reduce the processing time.

The propagation of the generated particles, as well as their interaction with the detectors, are simulated by the Geant4 framework [64, 65]. The digitisation of the detectors, including the alignment and calibration, and the hardware trigger effect is then simulated independently. These processes may not be reproduced correctly during the simulation and we need to use an external database to correct them. After that, all the simulated events will be required to pass the same software trigger, stripping line and offline selection criteria as the data sample to emulate the data closely, while their truth-level information, such as the momenta they were generated with, will also be recorded along with the reconstructed information. The truth-level information will play an important role in the calculation of the efficiency map used to correct the phase space acceptance.

In this analysis, the main MC simulation sample of $D^{*+} \to D^0(\to \pi^-\pi^+\pi^0)\pi^+$ used is based on the preliminary BaBar model [17]. The number of events generated for each year is given in Table 4.2, while the amplitude model from the BaBar analysis is summarised in Table 4.3. The discrepancy between the MC simulation and the data samples will be considered as one of the systematic uncertainties, which will be discussed

later.

Table. 4.2:   The number of generated and reconstructed candidates filtered by the stripping line in different years and magnet polarities for MC simulation samples.

Year/Polarity	$D^0 \to \pi^- \pi^+ \pi^0$		
	Merged	Resolved	Generation [$\times 10^6$]
2015 MagUp	38,613	362,400	5
2015 MagDown	39,218	362,494	
2016 MagUp	200,869	1,868,513	27.5
2016 MagDown	201,877	1,868,513	
2017 MagUp	215,263	2,121,651	30
2017 MagDown	216,420	2,134,503	
2018 MagUp	284,952	2,554,347	37.5
2018 MagDown	288,298	2,581,088	

Table. 4.3: The amplitude model of the $B^{\pm} \to D^0(\to \pi^-\pi^+\pi^0)K^{\pm}$ decay from the BaBar analysis [17]. The listed parameters including the modulus and phase of the fit parameters along with the fit fractions of the amplitudes are used in EvtGen for the corresponding MC simulation.

Resonance	Amplitude a_n	Phase ϕ_n ($\circ$)	Fit Fraction f_n (%)
$\rho(770)^+$	0.823	0	67.8
$\rho(770)^0$	0.512	16.2	26.2
$\rho(770)^-$	0.588	-2.0	34.6
$\rho(1450)^+$	0.033	-146	0.11
$\rho(1450)^0$	0.055	10	0.30
$\rho(1450)^-$	0.134	16	1.79
$\rho(1700)^+$	2.250	-17	4.10
$\rho(1700)^0$	2.510	-17	5.00
$\rho(1700)^-$	2.000	-50	3.20
$f_0(980)$	0.015	-59	0.25
$f_0(1370)$	0.063	156	0.37
$f_0(1500)$	0.058	12	0.39
$f_0(1710)$	0.112	51	0.31
$f_2(1270)$	1.040	-171	1.32
$\sigma(400)$	0.069	8	0.82
Non-Res	0.570	-11	0.84

Chapter 5

Data Selection

This analysis uses the data sample collected during the Run-II period from 2015-2018 at $\sqrt{s} = 13$ TeV, corresponding to an integrated luminosity of 5.7 fb^{-1}. A sample of $D^0 \to \pi^-\pi^+\pi^0$ decays are obtained by selecting prompt D^{*+} candidates via the strong decay of $D^{*+} \to D^0(\to \pi^-\pi^+\pi^0)\pi^+$. A schematic of the decay topology is shown in Figure 5.1. Charm (c)-quarks are produced at the PV where the p-p collision happens. The c-quarks then hadronise to one of the charm mesons (D^{*+}). Two-thirds of the D^{*+} meson will then decay to the $D^0\pi^+$ final state. The D^0 meson will fly on average 0.5 cm in the detector before decay, which is a distinct characteristic separate from the PV. This is the main decay mode of $\pi^0 \to \gamma\gamma$ is used to reconstruct the neutral pion candidate based on the photons energy deposit in the LHCb electromagnetic calorimeter. The $D^0 \to \pi^-\pi^+\pi^0$ sample is then separated into two categories according to the two different types of reconstruction of neutral pions: merged π^0 where the two photons deposit energy within a single calorimeter cell and resolved π^0 where the two photons are well separated and derived from individual energy clusters present in separate cells [46]. The two samples have different Dalitz Plot distributions and will be selected with different selection criteria. The offline requirements have been optimised and re-used from the CP violation search of $D^0 \to \pi^-\pi^+\pi^0$ using the Energy Test method [66]. In both analysis, we introduce the following variables to identify the signal candidates in the selection process:
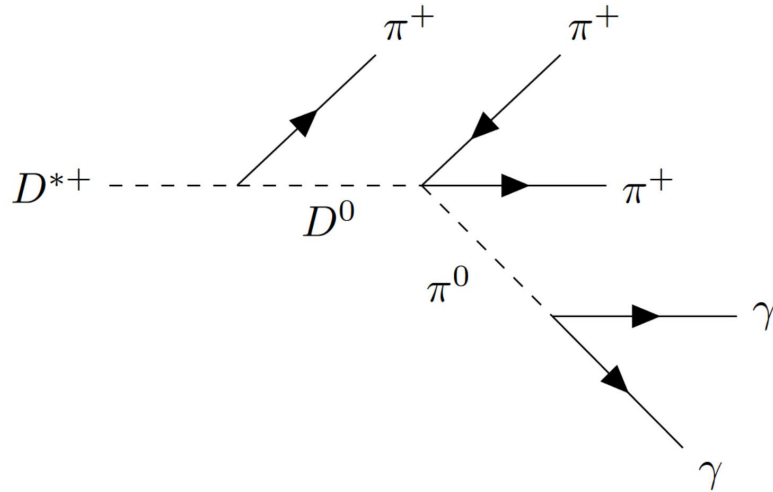
Figure. 5.1: A schematic of the decay topology. Particles which are detected and used in the reconstruction procedure are shown using solid lines. Particles which decay but do not interact with the detector directly are shown using dashed lines.

- DOCA is the minimum distance between two tracks, which shows the vertex information of tracks. A small DOCA implies a common vertex for the two tracks, which we usually constrain early in the selection process such as the stripping line to reduce the number of combinations of tracks. The χ^2_{DOCA} is defined as the DOCA in units of its uncertainty, which is used instead as a discriminating variable in this analysis.

- IP is the impact parameter, which is defined as the shortest distance between the extrapolated track and the PV. A large IP value for a track relative to the PV implies it originates from SV, which is used to discriminate the tracks originating from the PV and thus strongly relies on the lifetime of the decaying particle. The difference of the χ^2 in the vertex-fit for a PV including or excluding a given track, labelled as χ^2_{IP}, is used as a discriminator in this analysis.

- DV (decay vertex) is the SV of relatively short-lived particles reconstructed from the final state particles. The χ^2_{DV} defined as the fit quality with respect to DV is used in this analysis.

- DIRA is defined as the cosine angle between the flight path of the short-lived particle measured from two vertices and its total momentum reconstructed from the final state particles, which implies the reconstruction status of all decaying particles. If all the final state particles are fully reconstructed and have a good identification of the vertices, the DIRA will get close to 1. It is useful to discriminate the background events where the vertices can not be correctly identified.

- A ghost track is a kind of track where a certain ratio of the associated hits does not truly originate from the track, which can happen due to the high track densities in the LHCb detector. The ghost probability calculated with an MVA-based classifier is used to identify the ghost tracks [67], labelled as the P_{ghost}.

In general, all the candidates will be selected via several stages of the LHCb data selection processes successively, which can be expressed as

- Hardware and software trigger selection on a large amount of p-p collision data;

- Loose centralised offline preselection with a Stripping line for the specific decay channel;

- Further decay-based offline preselection to better constrain the signal candidates;

- A multivariate analysis to further eliminate background candidates;

- Other selections requirements including the removal of multiple candidates and cloned tracks.

The details of each stage will be described in the following.

5.1 Trigger selection

All of the trigger selections imposed in this analysis are summarised in Table 5.1. We first require all the candidates to pass at least one of four hardware-based L0 trigger lines, which aims to retain a high efficiency without introducing charge asymmetries.

Partial event reconstruction is then finalised on the HTL1 lines and three dedicated HLT2 lines specifically designed for the final states particles. Each line can be classified as Triggered On Signal (TOS) or the Triggered Independent of Signal (TIS) depending on whether or not the signal candidates' tracks are involved in the trigger decision. The L0 trigger lines can be further divided based on the specific particle species of hadrons, electrons, muons and photons. Compared to the LHCb analysis of this channel based on Run-I data [16], there is a more restrictive set of requirements in the L0 trigger for this analysis. Here we exclude the L0 trigger line designed for μ and e, because this trigger will significantly increase the background contamination and thus decrease the signal purity.

Table. 5.1:   The trigger lines used in the analysis.

Trigger level	Trigger line
L0	**Dstr_L0_Global_TIS** OR **H1_L0HadronDecision_TOS** OR **H2_L0HadronDecision_TOS** OR **pi0_L0PhotonDecision_TOS**
HLT1	**HLT1TwoTrackMVA** OR **HLT1TrackMVA**
HLT2	**Dstr_Hlt2CharmHadDstp2D0Pip_D02PimPipPi0_Pi0_[M,R]_Decision_TOS** OR **Dstr_Hlt2CharmHadInclDstr2PiD02HHXBDTDecision_TOS**

The HLT1 trigger consists of several lines mainly focusing on the properties of single tracks instead of the combination of all candidates, where the MVA-based classifiers using a boosted decision tree [68] are also used to improve the quality of the constraints. In this analysis, there is no dedicated L1 trigger requirement on the specific particle species. All the HLT1 trigger lines exist as an implicit requirement within the HLT2 lines. In detail, at least one of the final state particles originated from the D^0 candidate should pass the **HLT1TrackMVA**, or any combination of two final state particles should pass the **HLT1TwoTrackMVA** line. These lines constrain the thresholds of the IP of reconstructed tracks in different transverse momentum regions, which can be expressed

as

$$\chi^2_{IP} > 7.4 \quad (p_T > 25.0),$$

$$ln(\chi^2_{IP}) > ln(7.4) + \frac{1.0}{(p_T - 1.0)^2} + \lambda\Big(1 - \frac{p_T}{25.0}\Big) \quad \Big(p_T \in [1.0, 25.0]\Big),$$

where the momenta are expressed in GeV/c and λ is a constant corresponding to different years' conditions. It varies from 1.1 (2015, 2016) to 1.2 (2017, 2018). The **HLT1TwoTrackMVA** line also determines the quality of the two final state tracks by requiring the following inputs:

- The χ^2_{FD} known as the distance between the PV and DV of the short-lived particle (D^0 in our analysis),

- The sum of the transverse momenta of both final state particles,

- The number of tracks with $\chi^2_{IP} < 16$,

- The χ^2 of the vertex fit of both final state particles.

The HLT2 trigger performs the full event reconstruction of $D^{*+} \to D^0(\to \pi^-\pi^+\pi^0)\pi^+$ based on the information from the entire detector, which has a further precise requirement depending on the particle species of π, D^0 and D^{*+}. There are two exclusive lines designed for the merged and resolved π^0 candidates, respectively, and also an inclusive trigger line used to further increase the signal yield. The exclusive line mainly constrains the invariant mass of combined tracks and sets requirements on the quality of single tracks, which can be seen in Table 5.2. The inclusive line is based on a BDT to maximise the signal efficiency as well as reject fake tracks [45].

5.2 Stripping selection

The stripping selection in this analysis consists of two lines designed for the merged and resolved π^0 candidates, respectively. Resolved pions have a larger opening angle between the two photons, which is associated with lower π^0 transverse momentum. Thus,

Table. 5.2: HLT2 requirements for the **HLT2CharmHadDstp2D0Pip_D02PimPipPi0_Pi0 line**

Particle	Quantity	Selection criteria
$\pi^{\pm}$ pair	DOCA	< 0.08 mm
	$m_{\pi\pi}$	< 1900 MeV/c^2
	vertex χ^2	< 20
	χ^2 w.r.t best PV	> 25
	χ^2_{IP}	> 36
	Total p_T	> 1900 MeV/c^2
π^0	p_T	> 1700 MeV/c
	χ^2_{IP}	> 36
D^0	vertex χ^2	< 20
	p_T	> 1400 MeV/c
	$m_{\pi^-\pi^+\pi^0}$	$\in [1700,2020]$ MeV/c^2
	m_{D^0}	$\in [1745,1985]$ MeV/c^2
	χ^2 w.r.t best PV	< 50
	D^0 DIRA	> 0.9995
	τ_{D^0}	> 0.2 ps
$D^{*\pm}$	$m_{D^{*+}} - m_{D^0} - m_{\pi_s}$	$\in$ [-999, 45.43] MeV/c^2
	vertex χ^2	< 10
	$m_{\pi^-\pi^+\pi^0\pi_s} - m_{\pi^-\pi^+\pi^0} - m_{\pi_s}$	$\in$ [-185, 55.43] MeV/c^2

the resolved π^0 sample will comprise larger contamination from the combinatorial background, while the merged π^0 is purer due to the lower contamination from combinatorial background. On the other hand, due to the reconstruction of the deposited energy of photons, the merged π^0 sample also suffers from a worse resolution of the π^0 invariant mass than that of the resolved sample. Therefore, there is no requirement applied on the π^0 invariant mass for the merged sample in the stripping line. The stripping selection is presented in Table 5.3, which also shows the version used for each data-taking year.

5.3 Offline selection

After being filtered by the trigger system and a loose selection of the stripping line, the data sample will be saved to disk for further offline selection. At this stage, a decay-based offline preselection is firstly applied, after which an MVA classifier developed with the help of the S-weight technique will be used to eliminate background candidates.

Table. 5.3: Summary of the selection criteria of the stripping line used in this analysis. Here, π_s is the soft pion from the prompt D^{*+} meson decay.

Particle	Quantity	selection criteria
Global Selection	number of long tracks	< 180
$\pi^{\pm}$	p_T	> 500 MeV/c^2
	P_{ghost}	< 0.35
	PIDK	< 0
π^+orπ^-	p_T	> 1700 MeV/c
	χ^2 w.r.t best PV	> 36
$\pi^{\pm}$ pair	DOCA χ^2	< 15
	$m_{\pi\pi}$	< 1900 MeV/c^2
	vertex χ^2	< 3
	χ^2 w.r.t best PV	> 100
π^0 π^0 (resolved only)	p_T	> 500 MeV/c
	$|m_{\gamma\gamma} - 135\text{MeV/c}^2|$	< 15 MeV/c^2
D^0	vertex χ^2	< 20
	p_T	> 1400 MeV/c
	$|m_{\pi^-\pi^+\pi^0} - 1864.84|\text{MeV/c}^2$	< 160 MeV/c^2
	$|m_{D^0} - 1864.84|\text{MeV/c}^2$	< 150 MeV/c^2
π_s	p_T	> 300 MeV/c
	P_{ghost}	< 0.35
	PIDe	< 5
	min χ^2_{IP}	< 9
$D^{*\pm}$	$m_{D^{*\pm}} - m_{D^0}$	< 180 MeV/c^2
	vertex χ^2	< 9
	DOCA χ^2	< 20
	$m_{\pi^-\pi^+\pi^0\pi_s} - m_{\pi^-\pi^+\pi^0}$	< 185 MeV/c^2

The kinematic variables obtained by the DecayTreeFitter (DTF) algorithm [69], after refitting the decay chain with additional kinematic constraints, will be used in further steps. They are based on the fully reconstructed event and the knowledge of the decay topology. The DTF simultaneously considers all of the tracks within the decay topology. It then updates all the particle kinematics based on a set of external constraints, such as the known invariant mass of their vertex, to give the best vertex fit. Specifically, the full D^{*+} decay chain is reconstructed based on a basic constraint that D^{*+} originates from the p-p collision point (PV). The quantities for the final state particles originating from the D^0 meson will also be re-calculated with a mass constraint requiring that the reconstructed invariant mass of $m_{\pi^-\pi^+\pi^0}$ should match the known D^0 meson mass cited from the PDG [14]. The DTF algorithm ensures all the candidates will lie in the physically allowed Dalitz region, which improves the mass resolution of the D^{*+}, D^0 and other intermediate resonances.

In order to better discriminate the signal candidates of the combinatorial background, the difference between the reconstructed invariant mass of D^{*+} and D^0, labelled as Δm, is used. The mass difference of the two mesons corresponds to the reconstructed mass difference of $m_{\pi^-\pi^+\pi^0\pi_s^+} - m_{\pi^-\pi^+\pi^0}$. The low Q-value (with $Q \equiv m_{D^{*+}} - m_{D^0} - m_{\pi_s^+}$) of the decay results in a sharply peaked signal, which improves the signal purity of the data sample.

The details of the offline selection are as follows:

- arccos(DIRA) < 0.05 rad, which is defined from the DIRA of the D^0 meson to discriminate against the background events.

- $\log(\chi^2_{\mathrm{D}*}) < 2.3$, where the χ^2 represents the quality of the kinematic fit to the D^* vertex performed by the DTF algorithm, where the candidate is constrained to originate from the PV . The selection of the value is chosen based on the boundary of the signal and background distribution of $\log(\chi^2_{\mathrm{D}*})$, which is disentangled using the S-weight.

- $|m(\pi^0) - 135| < 28$ MeV/c^2, where m_{π^0} is the reconstructed invariant mass of the

neutral merged π^0 candidates. The selection of the value is chosen based on a mass fit to the m_{π^0} distribution, where the signal is parameterised by a Gaussian function and the selected region corresponds to about 2σ of the fitted Gaussian distribution. This requirement aims to remove the misidentified π^0 candidates from the resolved sample or the contamination from the converted e^+e^- pairs. A similar selection is applied to the resolved π^0 sample in the stripping line shown in Table 5.3.

- $|m(D^0) - 1864.84| < 60$ MeV/c^2, where $m(D^0)$ is the reconstructed mass of the D^0 candidates performed by the DTF algorithm. This selection is developed from the reconstructed D^0 mass distribution shown in Figure 5.2. The signal region is selected manually for $m(D^0)$, which corresponds to the loose boundary between the signal peak and the combinatorial background.
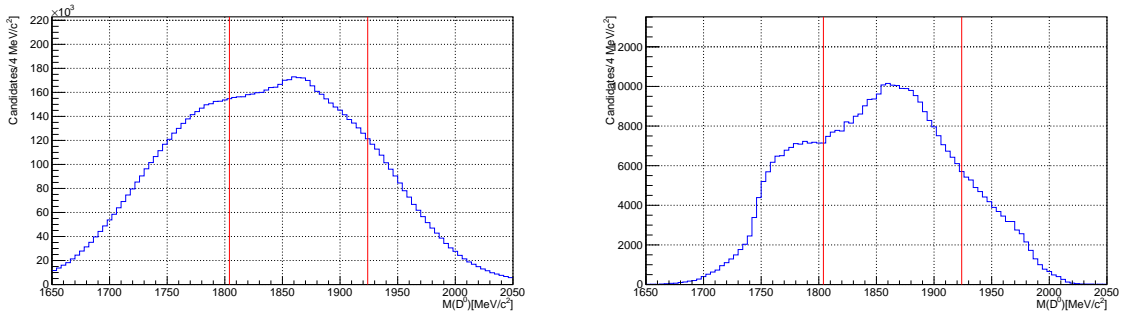
Figure. 5.2: The D^0 mass distribution for the resolved (left) and merged samples (right) after the offline selection except for $m(D^0)$ selection and the looser requirement on the DTF $\log(\chi^2_{D*}) < 4$ to illustrate the selection of the signal mass window which is in between the two vertical lines.

Moreover, two additional selection criteria are applied to remove the clone tracks and multiple candidates. Clone tracks originate from a single charged track mis-reconstructed as a bunch of near-collinear tracks. They can all be used in the particle identification algorithms and thus the same track can be double-counted. Such candidates will form a small background hidden in the signal region and is thus hard to separate from the signal sample directly in the mass fit. However, clone tracks can be characterised by having a

pair of charged tracks in the final state with a very small angular separation, and this pattern is used to remove these candidates. In this analysis, there are three charged final state tracks with two from the D^0 decay and one corresponding to the soft pion. Any combination of two of the three tracks can suffer from the contamination of cloned tracks, of which the angular separations are shown in Figure 5.3. The distribution for the correctly reconstructed tracks will fall to zero due to no angular separation between charged tracks, while the peaks near zero originate from the cloned tracks. The requirement of $\theta > 0.0005$ is then selected based on the boundary of the two distributions, which will reduce the contamination of cloned tracks to negligible levels.
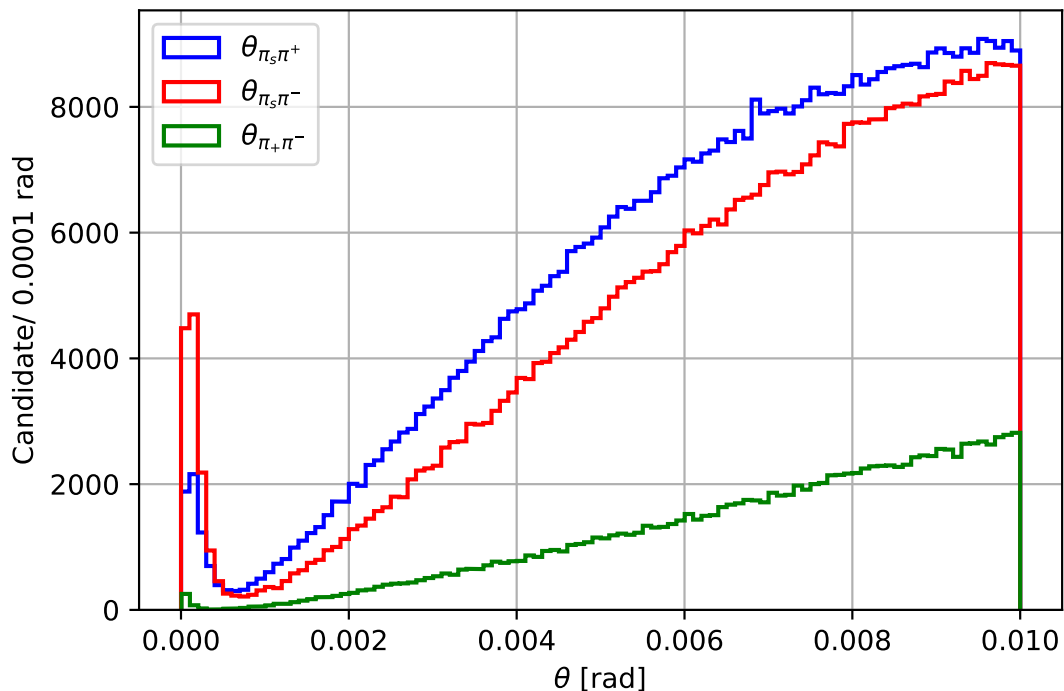
Figure. 5.3: Distributions of the angle between pairs of charged tracks.

Multiple candidates can be reconstructed in a single p-p collision event. They mostly originate from multiple reconstructed soft pion candidates, each of which is then associated with a single D^0 candidate and thus several prompt D^{*+} candidates are identified. All of these candidates have mostly identical kinematics and can enter the final signal

sample used for the amplitude fit. They are present in about 5.9% (2.5%) of events in the resolved (merged) samples. This can bias the CP violation measurement if the effect is different for both flavours. A constraint that at most one signal candidate is used per event is then applied, where the selection among the multiple candidates is random. This is done with the help of the internal LHCb IDs of the run number and the event number, and these numbers will be the same for all multiple candidates within the event.

5.4 Multivariate analysis

The signal yield of the data sample is obtained via the fit on the Δm distribution, which requires a clear separation between signal and background candidates. We develop separate MVA-based classifiers for the resolved and merged samples to further suppress the combinatorial background. The motivation for the use of MVA classifiers can be seen from the preliminary fit on the Δm distribution shown in Figure 5.4. The high transverse momentum of π^0 candidates in the merged sample ensures a relatively higher signal purity after the preselection without applying the MVA classifier. However, a significant component of combinatorial background can be seen in the resolved sample, which originates from the low transverse momentum of π^0 candidates. Thus, we develop and apply the MVA-based classifier only for the resolved sample in this analysis. Before training, the resolved sample will be separated into two subsets to avoid bias, which depends on the parity of the event number by convention in our analysis. One of the subsets will be used to train and evaluate the performance of the classifier. The classifier is then applied to the other subset to check for overtraining, which is known as cross-training. This method of cross-validation removes bias from the training by ensuring that the classifier is not applied to candidates used in the training [70].

The training process for the classifiers is based on the comparison of the characteristic variables between the signal and background samples, which is obtained with the help of S-weights calculated with the sPlot technique [60]. In the Δm fit, the signal component
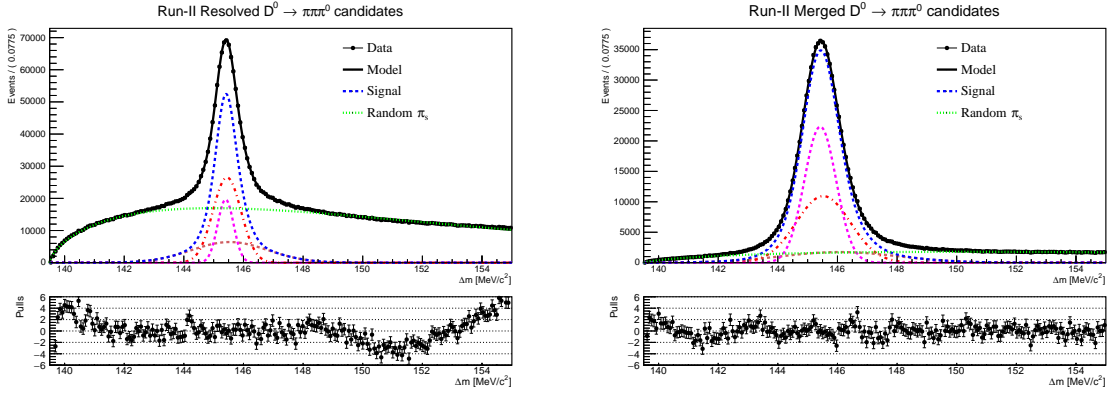
Figure. 5.4: The preliminary fits to the Δm distribution for 40% of the resolved sample (left) and merged sample (right) before multivariate analysis. The dots with error bars are data. The blue solid curves are the fit results. The blue dotted curves are the fitted signal, the green dot-dashed curves are the fitted combinatorial backgrounds. The brown, red dotted curves are two independent Gaussian functions, while the cyan dotted curves are the bifurcated Gaussian function.

is parameterised by the product of three independent Gaussian functions, which can be expressed as

$$F_{sig} = f_1 \cdot \frac{1}{\sqrt{2\pi\sigma_1^2}} \cdot e^{-\frac{(x-\mu_1)^2}{2\sigma_1^2}} + (f_2) \cdot \frac{1}{\sqrt{2\pi\sigma_2^2}} \cdot e^{-\frac{(x-\mu_2)^2}{2\sigma_2^2}} + (1-f_1-f_2) \cdot \frac{1}{\sqrt{2\pi\sigma_3^2}} \cdot e^{-\frac{(x-\mu_3)^2}{2\sigma_3^2}}, \quad (55)$$

where f_1, f_2 is the coefficients of the first two Gaussian functions, $\mu_1(\sigma_1)$, $\mu_2(\sigma_2)$ and $\mu_3(\sigma_3)$ are the center values (resolution) of the relevant Gaussian functions. The background component is parameterised using the empirical formula

$$F_{bkg} = (\Delta m - m_{th})^{\alpha} e^{-\beta(\Delta m - m_{th})}, \quad (56)$$

where m_{th} is a fixed threshold parameter defined as the charged pion rest mass. The factors α and β are all free parameters in the fit. As the resolved sample is very large, the sPlot technique is only applied to 40% of the sample to reduce the processing time. The preliminary fit projections for both resolved and merged samples are shown in Figure 5.4. In the fit, the small discrepancy between the PDF and the data sample is located in the background region, and is not expected to affect the selection performance. The fit

71

parameters are summarised in Table 5.4.

Table. 5.4: The fit parameters used in the preliminary fit to the Δm distribution shown in Figure 5.4 for both the resolved (40% of the sample) and full merged samples after the pre-selection process.

Parameter	Resolved	Merged
N(Signal) [10^3]	836.28 ± 3.10	800.71 ± 2.85
N(Background) [10^3]	2767.73 ± 3.38	281.87 ± 2.94
σ_1 [MeV/c^2]	0.470 ± 0.016	0.532 ± 0.009
σ_2 [MeV/c^2]	1.277 ± 0.023	1.953 ± 0.064
σ_3 [MeV/c^2]	0.263 ± 0.012	0.907 ± 0.034
μ_1 [MeV/c^2]	145.534 ± 0.012	145.424 ± 0.003
μ_2 [MeV/c^2]	145.453 ± 0.006	146.078 ± 0.049
μ_3 [MeV/c^2]	145.404 ± 0.003	145.525 ± 0.011
α	0.651 ± 0.003	0.697 ± 0.014
β	0.119 ± 0.001	0.065 ± 0.003

After separating the signal and background component, the classifier's training is processed, where different types of classifiers are considered for comparison. Here, we use the receiver-operator characteristic (ROC) curve as a figure of merit, where the area under the curve is used to judge the best classifier to be used. Each classifier is constructed with a variety of Boosted Decision Trees (BDTs) [71]. The Decision Tree (DT) is a binary tree-structured classifier, which is used to categorise the events as signal or background. A schematic of a decision tree is shown in Figure 5.5. It consists of layers of nodes which will iterate over every candidate. Starting from the root node, A successive application of binary splits is applied to the data, each corresponding to an output node which contains the most characteristic variable, for instance, the kinematic and/or angular distributions for each event, which has the best quality of separation between signal and background. The output then leads to a new node with updated criteria until all the events are iterated and assigned either signal or background property. As a single decision tree is unstable due to the influence of the statistical fluctuation of the training samples, The boosting technique is applied, extending one decision tree into a series of decision trees (decision forest). It will iterate the training process several times, and the resulting reweighted training sample in each iteration is then used to

train a new decision tree. A residual calculated by a loss function from the current tree will be used to improve the outcome of the new tree, where the misclassified events are given a larger weight. Each decision tree develops a specific classifier for the data set, while the final classifier is developed by combining these trees in series such that the errors are minimised [72].
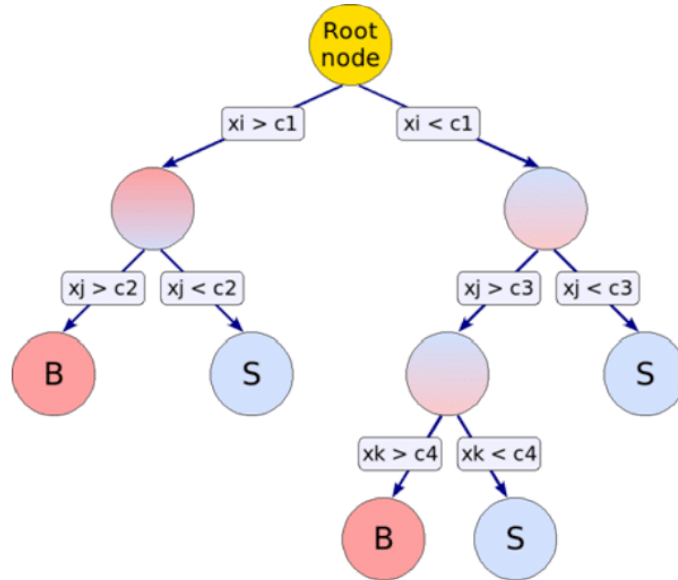
Figure. 5.5: Schematic view of a decision tree, reproduced from Ref [72]. A sequence of binary splits using the discriminating variables $\vec{x}$ is applied to the data to give the best separation between signal and background event.

The BDT input discriminating variables are

- $p_T(\pi^0)$ (Dstr_FIT_Pi0PT): The transverse momentum of the π^0 candidate.

- $cos(\theta_{\pi^0})$ (pi0_CosTheta): The cosine angle between the momentum of the π^0 candidate and that of the D^0 candidate (p_{π^0} in the rest frame of D^0 candidate while p_{D^0} in the lab frame.)

- $cos(\theta_{K^*})$ (Kstr_CosTheta): The cosine angle between the momentum of the $\pi^+\pi^-$ resonance and that of the D^0 candidate (p_{K^*} in the rest frame of the D^0 candidate while p_{D^0} is in the lab frame.)

- $p(\pi^0)$ (Dstr_FIT_Pi0P): The momentum of the π^0 candidate.

- $log[C.L.(\pi^0)]$ (log_pi0_CL): The logarithm of the confidence level of the π^0 candidate.

- $p_T(D^*)$ (Dstr_FIT_PT): The transverse momentum of the D^{*+} candidate.

- $p_T(D^0)$ (Dstr_FIT_DPT): The transverse momentum of the D^0 candidate.

- $log(\chi^2_{IP})$ (log_D_IPCHI2_OWNPV): The logarithm of the χ^2_{IP} for the D^0 candidate with respect to the PV.

- $acos(DIRA_{D^0})$ (acos_D_DIRA_OWNPV): The inverse cosine angle of DIRA for the D^0 candidate .

- $log(\chi^2)$ (log_FITCHI2): The logarithm of the fitting χ^2 probability calculated based on the DTF, which is constrained by the D^* candidate PV and the π^0 mass.

- χ^2_{FD} (D_FDCHI2_OWNPV): The χ^2 of the flight distance between the PV to DV of the D^0 candidate.

- $cos(\theta_D)$ (D_CosTheta): The cosine angle between the momentum of the D^0 candidate and that of the D^{*+} candidate (p_{D^0} in the rest frame of the D^{*+} candidate while $p_{D^{*+}}$ is in the lab frame.)

- $p_T(\pi^-\pi^+)$ (H_PT_SUM): The scalar sum of the transverse momenta of the π^- and π^+ candidates.

Figure 5.6 shows the ROC curves for different selected classifiers after the training processes based on all these input variables, where the classifiers constructed based on the Decorrelated BDT (BDTD) show the largest area under the ROC curve, averaged over the folds [72]. The ranking of the input variables is given in Table 5.5. The comparison of the discriminating variables between the signal and background distribution used in the classifier is shown in Figure 5.7.

74
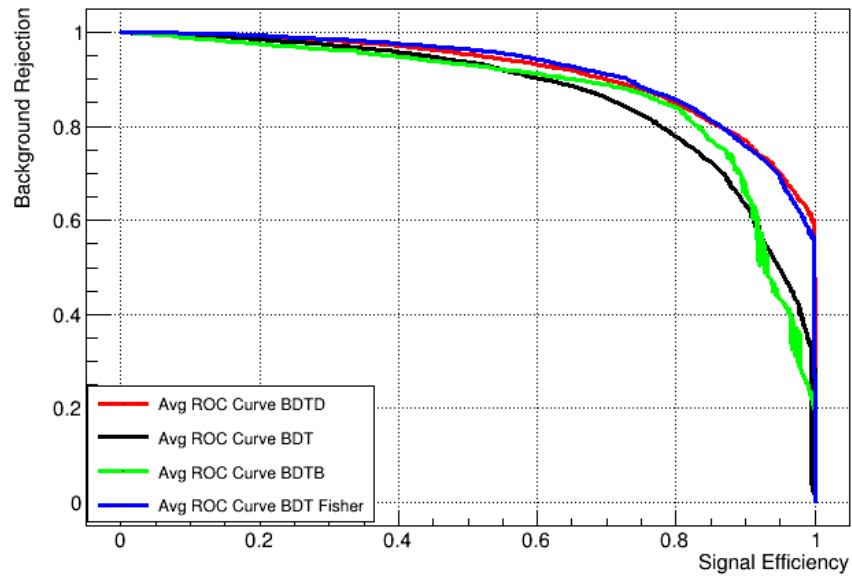
Figure. 5.6: The ROC curves for the different classifiers based on the resolved sample.

Table. 5.5: Rank of BDTD variables.

TMVA Rank	Input Variable	Separation (%)
1	Dstr_FIT_Pi0PT	40.25%
2	pi0_CosTheta	35.49%
3	Kstr_CosTheta	35.45%
4	Dstr_FIT_Pi0P	32.97%
5	log_pi0_CL	23.96%
6	Dstr_FIT_DPT	11.71%
7	Dstr_FIT_PT	11.13%
8	log_D_IPCHI2_OWNPV	10.45%
9	acos_D_DIRA_OWNPV	7.02%
10	log_FITCHI2_Prob	5.97%
11	D_FDCHI2_OWNPV	5.41%
12	D_CosTheta	3.30%
13	H_PT_SUM	2.32%
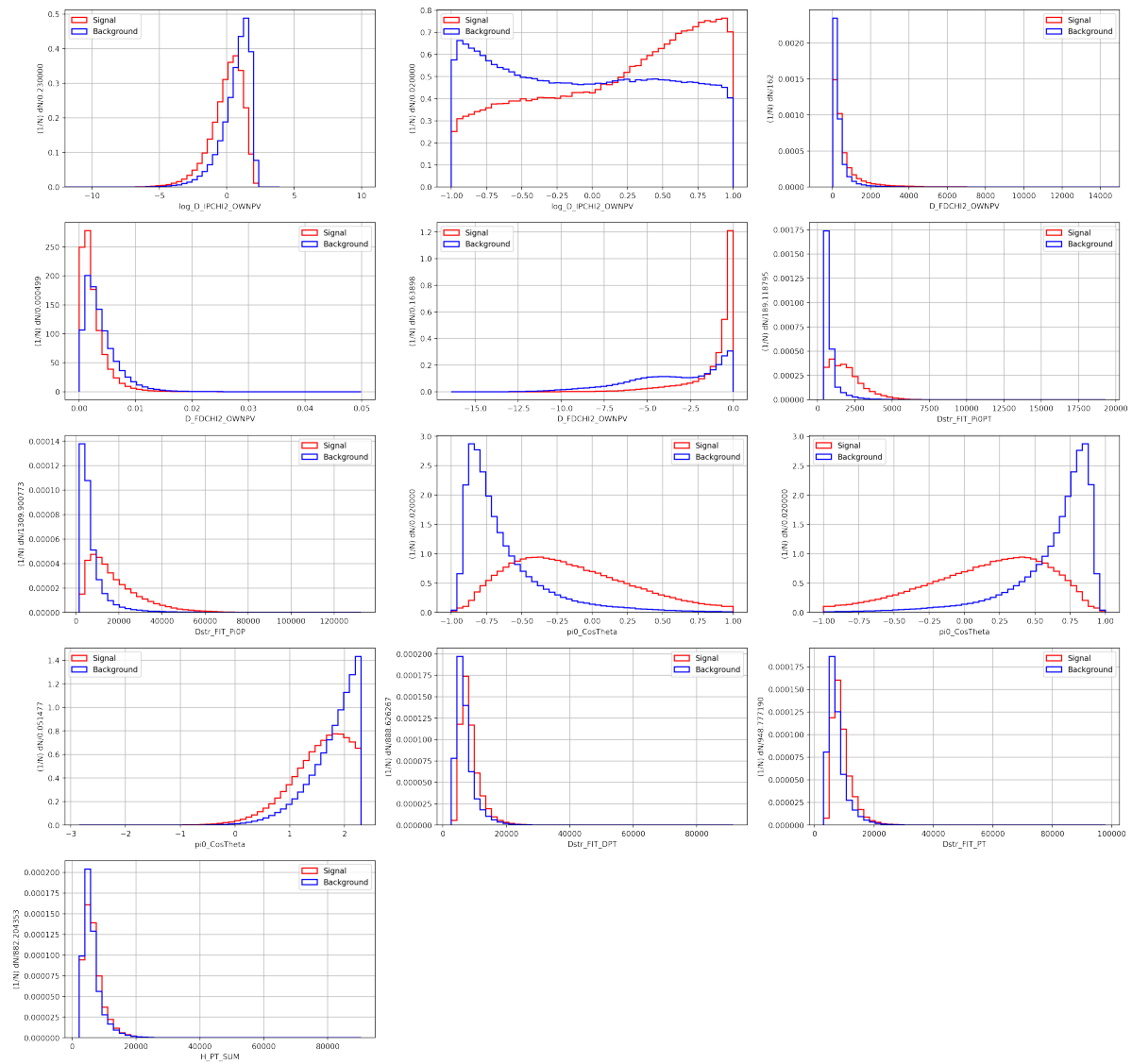
Figure. 5.7:   Normalised distributions of the input variables for the training in the resolved sample.

Though the use of an MVA-based classifier will efficiently discriminate the background contribution, the over-training of the classifier could introduce additional bias into the selection as well as a dissatisfactory result. The Kolmogorov-Smirnov (KS) test [73] is thus applied to the MVA output variables for the training and testing samples, of which the signal and background distribution are compared in the same plot shown in Figure 5.8. The KS test can evaluate the likelihood of whether the two samples originate from the same distribution. A higher KS value is expected to indicate no sign of over-training which can be seen in the plot. The selection of the MVA output value is optimised based on the signal significance $S/\sqrt{S+B}$, where S is the signal yield and B is the background yield in the signal region we choose ($|\Delta m - 145.4| < 1.8 \mathrm{MeV/c^2}$ in this analysis). The signal significance calculated in this step is based on the preliminary Δm binned fit after the preselection shown in Figure 5.4. The scan plot of the signal significance and purity in terms of the MVA output is also shown in Figure 5.8. We choose the MVA output at the maximum significance point of 0.05 as our selection criterion.
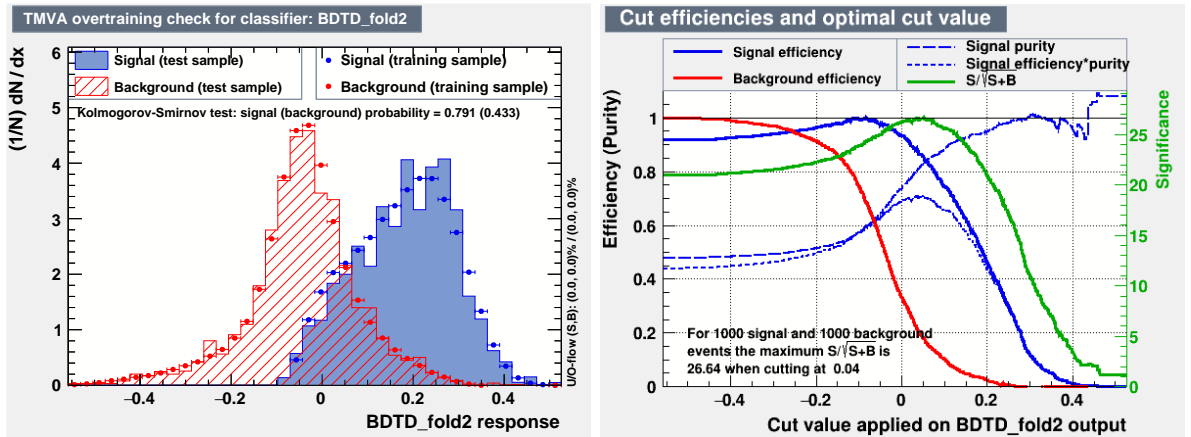
Figure. 5.8: The BDTD output distribution for the signal and background samples (left) and the scan plot on the efficiency, significance and their product (right). All the training and testing samples are based on the 40% resolved sample.

5.5   Final signal sample

After all the trigger, stripping, preselection selection criteria and MVA-based classifi-er are applied to the data sample, we can obtain the signal yield from a final Δm binned fit on the final resolved and merged data samples, which are shown in Figure 5.9. For the Δm fits, the signal component is described by the sum of two independent Gaussian functions and a bifurcated Gaussian which has a different width for its two sides. The background component is still modeled by the empirical formula shown in Equation 56 for both samples. The fit results are summarised in Table 5.6. While we found a not great description of the background tail in the Δm fit on the resolved sample, It has been studied in Ref [66] the sideband does not indicate any significant background asymmetry at the current level of sensitivity, and thus will not affect our measurement too much.

Table. 5.6:   The fit parameters used in the final Δm distributions shown in Figure 5.9 for both the resolved and merged samples after all the selection criteria.

Parameter	Resolved	Merged
N(Signal) [10^3]	1778.66 ± 5.33	800.34 ± 2.69
N(Background) [10^3]	1218.73 ± 5.28	281.87 ± 2.59
σ_1 [MeV/c^2]	0.470 ± 0.016	0.541 ± 0.005
σ_2 [MeV/c^2]	1.277 ± 0.023	1.783 ± 0.042
σ_L [MeV/c^2]	0.578 ± 0.012	1.125 ± 0.075
σ_R [MeV/c^2]	0.545 ± 0.007	0.811 ± 0.021
μ_1 [MeV/c^2]	145.409 ± 0.002	145.402 ± 0.003
μ_2 [MeV/c^2]	145.416 ± 0.008	146.355 ± 0.113
μ_3 [MeV/c^2]	145.490 ± 0.011	145.772 ± 0.021
α	0.884 ± 0.006	0.708 ± 0.012
β	0.176 ± 0.002	0.070 ± 0.003

The final signal sample is selected from the signal region of $|\Delta m - 145.4| < 1.8$ MeV/c^2. For the resolved sample, the signal yield is 1642168 with a purity of 81% and a signifi-cance of 1156.8. For the merged sample, the signal yield is 746619 with a purity of 91% and a significance of 826.
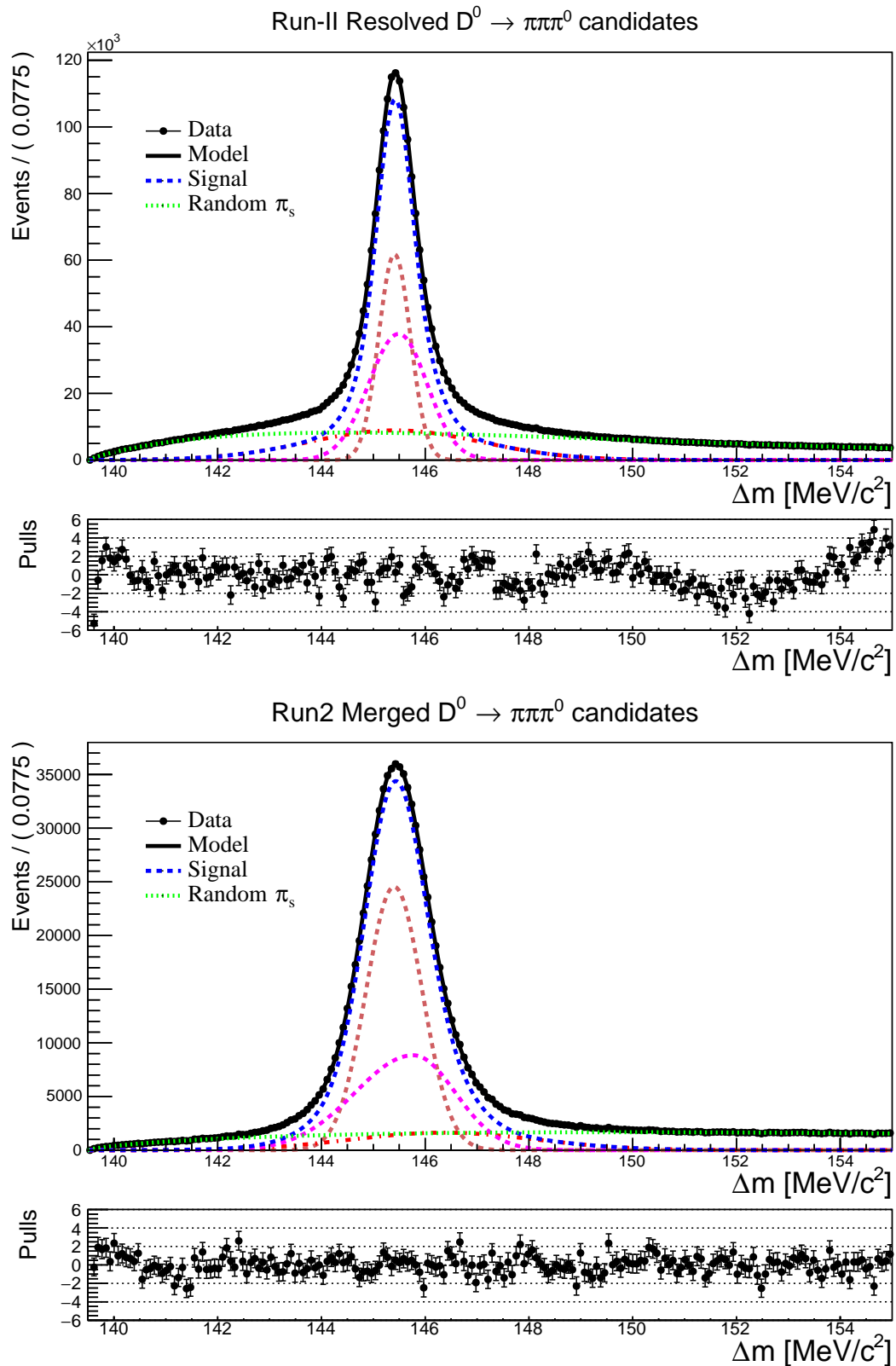
Figure. 5.9: The final fit on the Δm distribution for the resolved (top) and merged (bottom) sample, after all the selection criteria are applied.

5.6   Dalitz plot and projections

Before the amplitude fit, we can have a preliminary grasp of the resonant structure and the potential background contribution to the signal model via the Dalitz plot and the projections of the Dalitz variables. The Dalitz plot and projections for both signal and background regions in Δm are firstly checked, where the background region is defined by the sidebands of Δm in the regions $\Delta m > 150\text{MeV}/c^2$ or $\Delta m < 142\text{MeV}/c^2$. The 2-dimensional (2D) Dalitz Plots in terms of m_{13}^2 and m_{23}^2 for the resolved and merged sample are illustrated in Figure 5.10, while the corresponding 1D Dalitz projections of the three Dalitz variables are shown in Figure 5.11. Here, the ordering of the particles is chosen based on the charge of parent D^{*+}, which means m_{13} (m_{23}) refers to $m_{\pi^+\pi^0}$ ($m_{\pi^-\pi^0}$) for D^0 candidates and $m_{\pi^-\pi^0}$ ($m_{\pi^+\pi^0}$) for $\bar{D}^0$ candidates. All distributions have been normalised for comparison.

A clear difference can be seen from the comparison of the distributions, especially in the Dalitz projection of m_{12}^2, which means that the phase space acceptance for the resolved and merged sample differ a lot.

In addition, The S-weighted Dalitz plots and projections corresponding to the pure signal and background distributions are presented in Figure 5.12 and Figure 5.13, respectively. The S-weights are extracted from the Δm fit on the final data sample indicated by Figure 5.9. As a result, the S-weighted Dalitz plots and projections are illustrated in the full Δm area.

The typical contribution of charged and neutral $\rho(770) \to \pi^+\pi^-$ resonances can be seen in both the signal and S-weighted 1D Dalitz projections and the 2D Dalitz Plot with a two-lobe structure, of which the strong interference effect is also shown. Other possible resonances contributing to the Dalitz distributions, including the wide resonances of $\rho(1450)$ and $\rho(1700)$ showing a significant fraction in the previous amplitude model [17], have relatively lower amplitudes which need further amplitude analysis to resolve them. A possible non-resonant component is expected in the amplitude model which mainly forms the wide tails in the projections. The $\rho(770)$ resonances presented in the background distribution show a broader shape, which suggests that they are
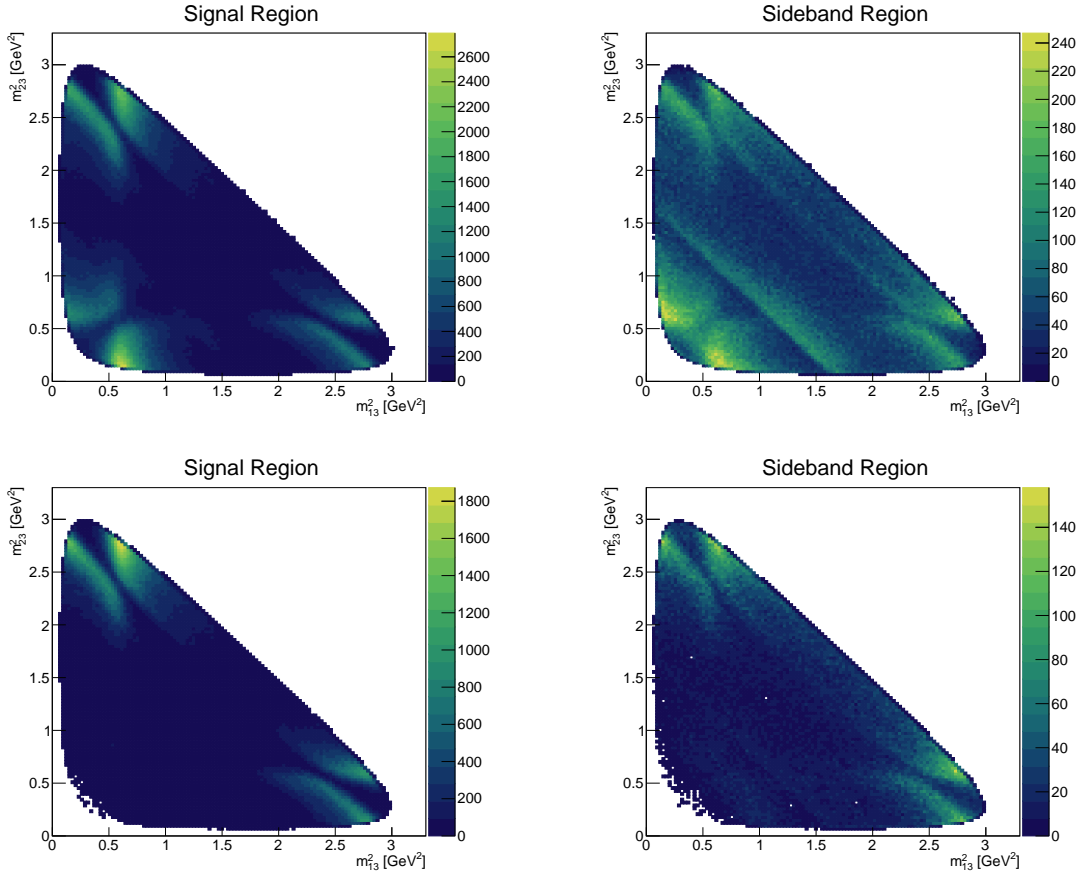
Figure. 5.10: Dalitz plot of m_{13}^2 vs. m_{23}^2 variables for the resolved (top) and merged (bottom) sample in the signal or sideband region of the Δm distribution shown in Figure 5.9.

mis-reconstructed.

An additional bump structure is present in the background distribution in the projection of m_{12}^2, peaking at about 1.8 GeV/c^2 and is most prominent for the resolved sample (top left plot in Figure 5.11 and Figure 5.13). This bump has been studied that this feature originates from the cross-feed of $\rho(770)^\pm$ reconstructed with a random π^0 of higher momentum [16]. However, the improvement on the threshold of the transverse momentum of π^0 as well as the removal of the inclusive HLT2 trigger can both strongly suppress this additional bump, which implies that this feature is associated with a low p_T π^0 candidate. Moreover, the feature could originate from the $D^0 \rightarrow K_S^0(\pi^0\pi^0)\pi^+\pi^-$ decay, where only one of the π^0s is detected. The contamination from this decay can
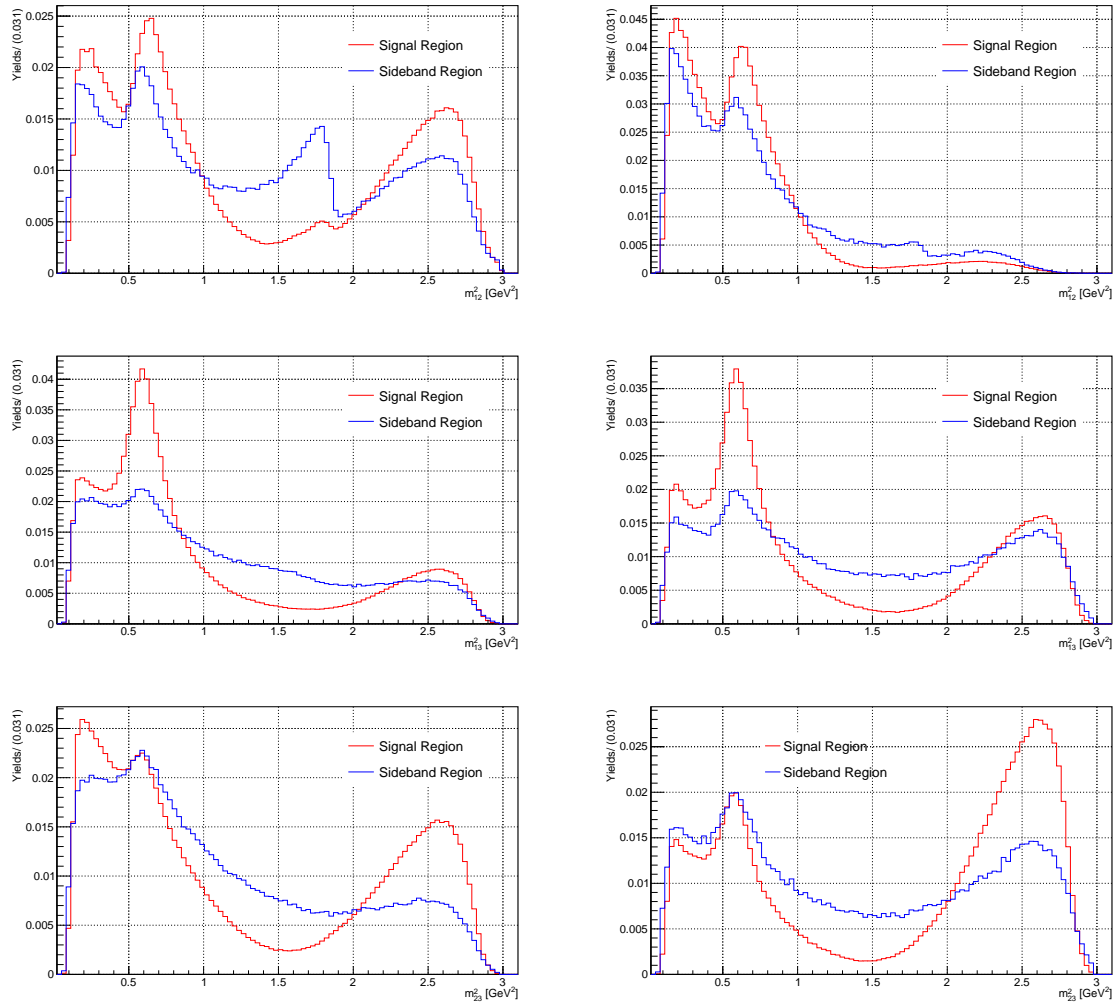
Figure. 5.11: The three Dalitz projections of m_{12}^2 (top), m_{13}^2 (middle), m_{23}^2 (bottom) in the signal or sideband region of the Δm distribution for the resolved (left) and merged (right) sample.
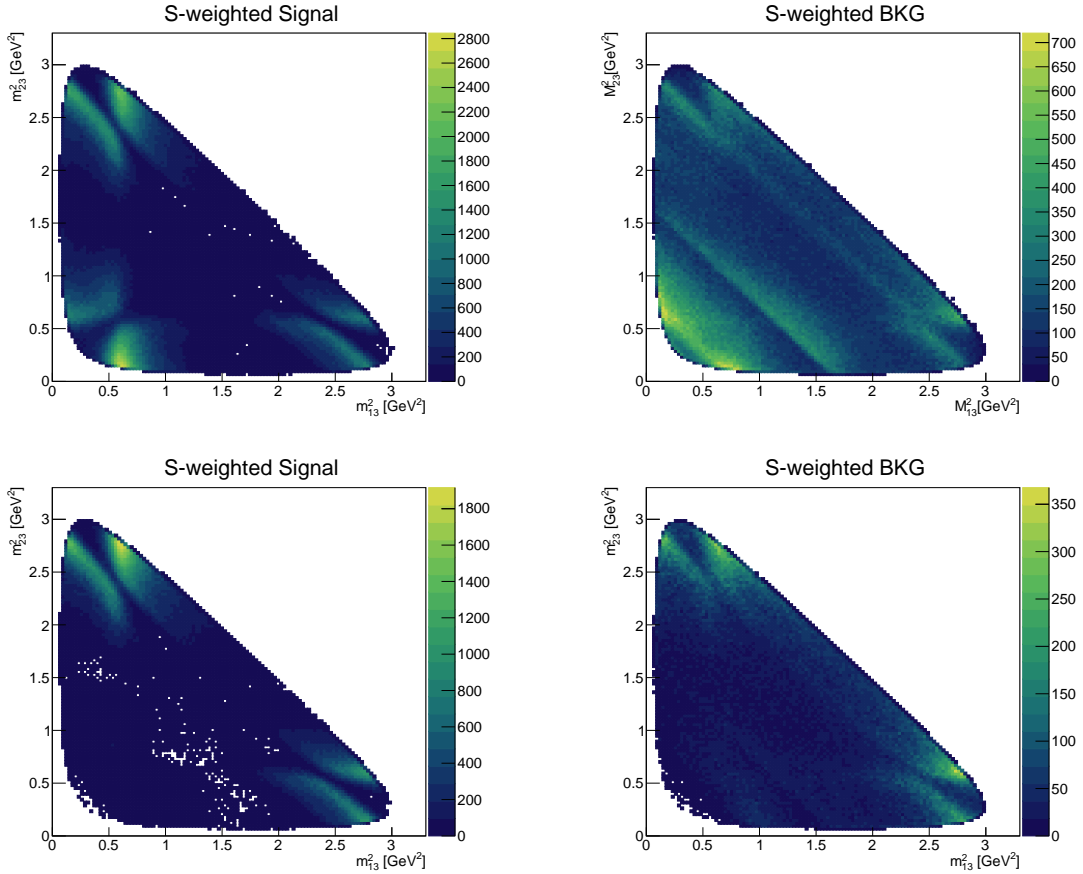
Figure. 5.12: Dalitz plots of m_{13}^2 vs. m_{23}^2 variables for the resolved (top) and merged (bottom) sample with the S-weighted signal (left) or with S-weighted background candidates (right).

be obvious due to its high branching fraction and the same invariant mass region of the $\pi^+\pi^-$ system. We can develop another MVA-based classifier based on the $D^0 \rightarrow K_S^0 \pi^+ \pi^-$ decay to suppress this kind of misidentification background. However, as the tighter selection on the p_T for the π^0 as well as the use of S-weight can effectively suppress this feature, we will not include this in our amplitude fit.

5.7 Phase space acceptance

The final data sample after all the selection criteria will also include various detector effects and possible biases from different stages of the reconstruction. To consider these
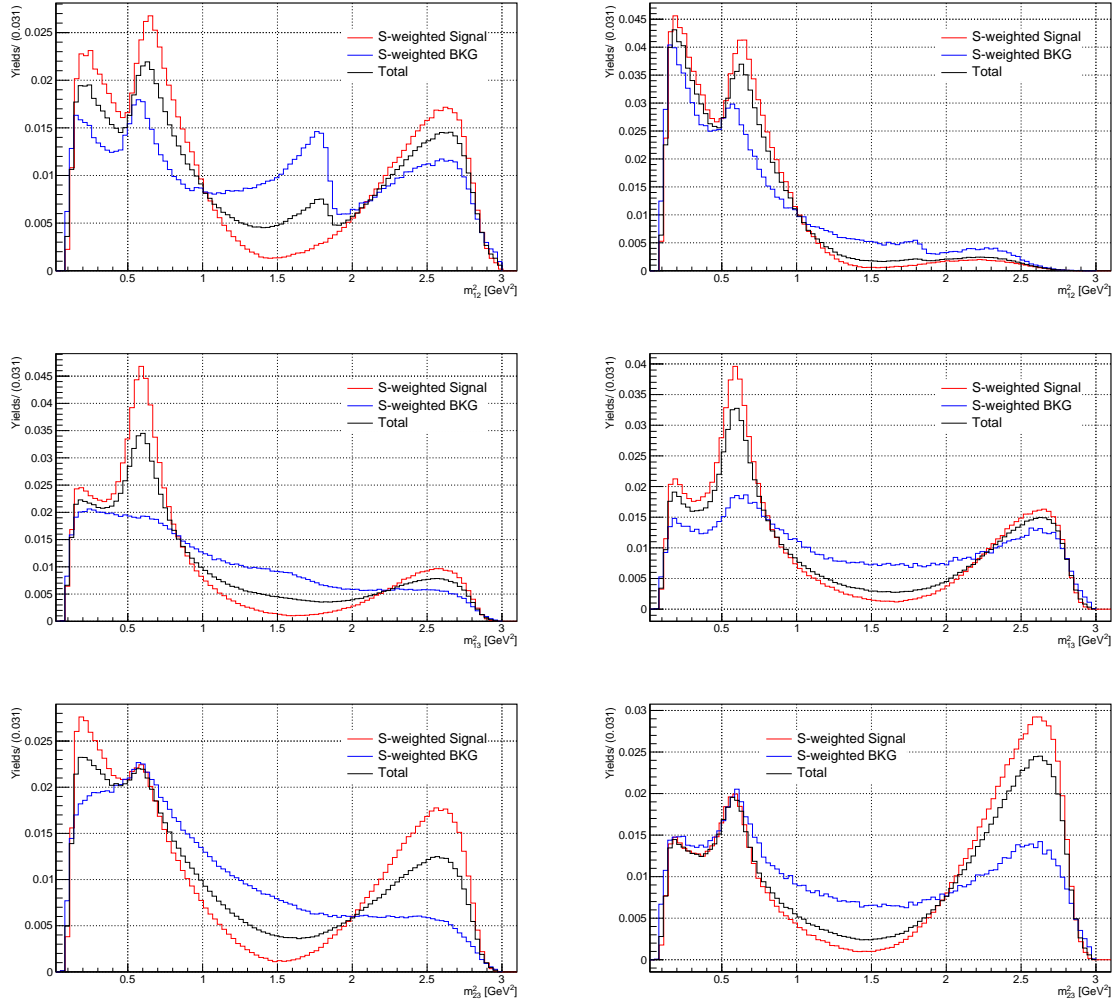
Figure. 5.13: The three Dalitz projections of m_{12}^2 (top), m_{13}^2 (middle), m_{23}^2 (bottom) with S-weight from the Δm distribution for the resolved (left) and merged (right) sample. The red histograms are the S-weighted signal, the blue histograms are the S-weighted background and the black histograms are the total distribution without weight.

84

effects, the variations of the model acceptance across the phase space of the decay, also referred to as the efficiency map, should be accounted for in this analysis. The signal efficiency can be extracted using large MC simulation samples based on the BaBar result shown in Table 4.3, which are simulated under the same detector conditions as the data collected from the year 2015-2018 at a centre-of-mass energy of 13 TeV to ensure the accuracy of the efficiency. The MC simulation samples after the reconstruction are required to pass the same selection criteria as the data samples, with the exceptions of the L0 Trigger and the PID response, which are usually not reproduced well in the simulation. We will not include any correction of the L0 trigger efficiency as it will not affect the accuracy of the efficiency map. The calibration on the PID response in this analysis is not applied yet due to the limit of the current MC sample. It will be assigned in our future work. Each simulated event is also filtered by truth matching, which is done by requiring each reconstructed particle candidate to match its generator-level information. The truth-matching process ensures a low background contamination in the filtered MC simulation sample. After all these steps, the signal efficiency can be directly calculated based on the ratio of the number of reconstructed MC simulated events n_{sig} over the total number of generated events n_{gen}

$$\epsilon = \frac{n_{sig}}{n_{gen}}. \tag{57}$$

The efficiency over the Dalitz plot is shown in Figure 5.14, while the comparison of the Dalitz projection distributions between the candidates after the full selection and the total events at the generator level (including both merged and resolved samples) is shown in Figure 5.14. Here, the efficiency map and the 1D projections are all normalised, as it is the relative scale of the map rather than the specific values in each bin that reflects the non-uniform phase space acceptance due to reconstruction and selection. This effect will be included in the amplitude analysis.
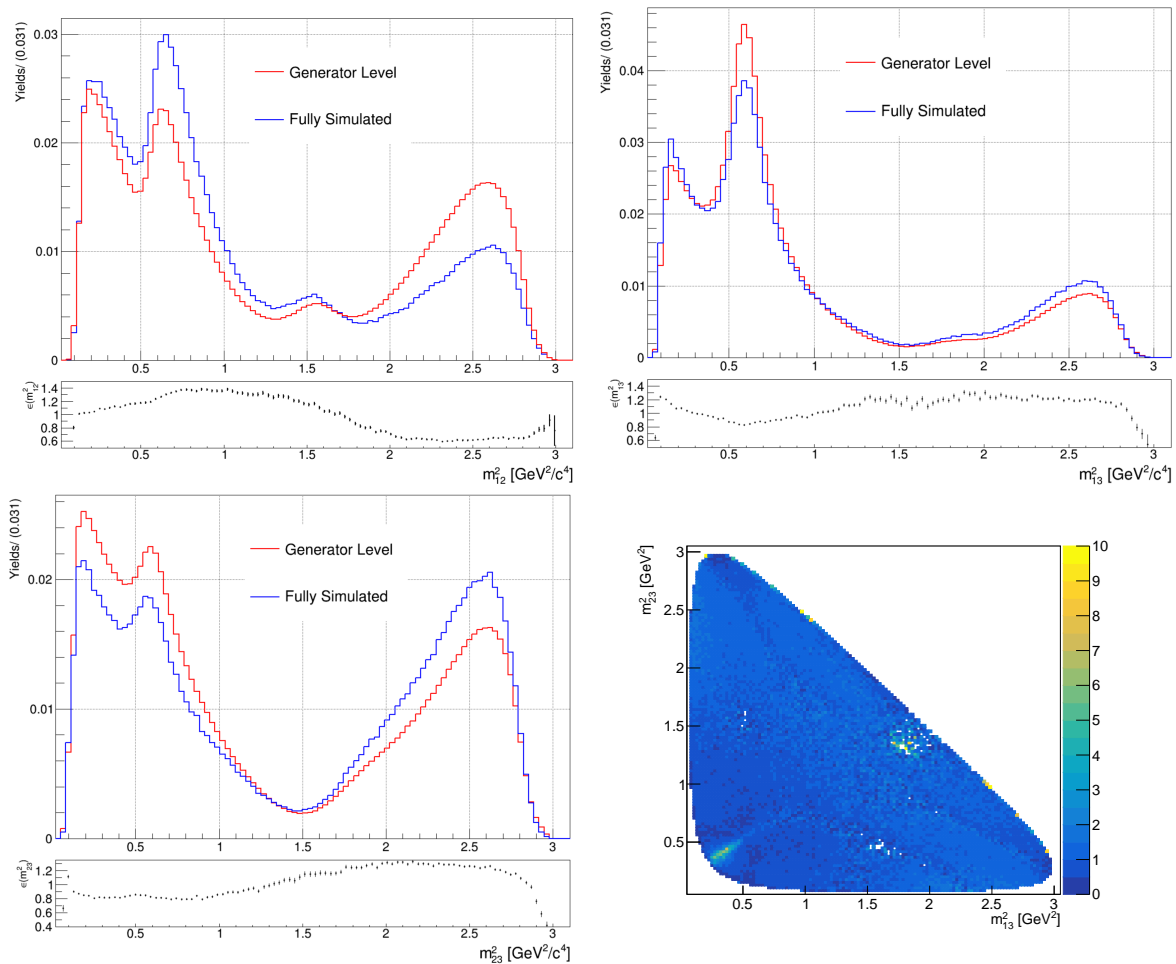
Figure. 5.14: Comparison of the Dalitz projection distributions between the fully simulated MC samples and the total events at the generator level as well as the efficiency on each dimension. Also shown is the 2D efficiency map used in the amplitude fit.

Chapter 6

Amplitude fit

An amplitude analysis describes a complex decay model with a coherent sum of amplitudes, each corresponding to a specific decay chain from the parent particle to the final state, as well as the possible interference between these amplitudes. Such a study aims to construct the decay model with the correct components that contribute to the decay. Their respective fractions are computed based on the extracted magnitude factor of A_r and ϕ_r shown in Equations 23 and 24. In this analysis, the time-integrated amplitude fit is performed on the $D^0 \to \pi^-\pi^+\pi^0$ phase space to obtain an accurate CP averaged model. The model presented in this thesis is only the preliminary model obtained at the first stage. Further improvement of the current model will continue in my future work.

As discussed in Chapter 2, the amplitude for a multibody process is described by the isobar model, which decomposes the total amplitude in terms of a series of quasi-independent two-body processes. The amplitude for an isobar is written as Equation 33, where the Blatt-Weisskopf form factors $F^{(L)}$ and the spin factor based on the Zemach formalism have been introduced in detail. The propagator $\mathcal{T}_r$ describes the dynamics of the resonance decay. Though the general lineshape of the resonance is usually expressed by the RBW propagator given in Equation 44, some amplitudes are not well-characterised due to their complicated dynamics as well as the limit of the RBW function. Other lineshapes used for the two body isobars are thus introduced in this analysis, which we

will describe in the following.

6.1 Gounaris-Sakurai propagator

The Gounaris-Sakurai (GS) propagator [74] is usually used to describe a broad resonance such as $\rho(770)^0$ and $\rho(1450)^0$ in the $\pi\pi$ scattering process. It is a modification of the RBW propagator in which two extra parameters depending on the $\pi\pi$ invariant mass are introduced, and thus shows a better description of these broad resonances than the RBW propagator. It is written as

$$\mathcal{T}_r(m) = \frac{1 + d\frac{\Gamma_0}{m_0}}{(m_0^2 - m^2 + f(m)) - im_0\Gamma(m)}, \tag{58}$$

where m_0 and Γ_0 is the pole mass and width of the resonance, respectively, Γ is the running width defined previously in Equation 45, and the two extra variables $f(m)$ and $d = f(0)/(\Gamma_0 m_0)$ are defined as

$$f(m) = \Gamma_0 \frac{m_0^2}{q_0}\left\{\frac{q^2}{q_0^2}[h(m) - h(m_0)] + (m_0^2 - m^2)\frac{dh}{dm}\Big|_{m_0}\right\}, \tag{59}$$

$$d = \frac{3}{\pi}\frac{m_\pi^2}{q_0^2}\log\left(\frac{m_0 + 2q_0}{2m_\pi}\right) + \frac{m_0}{2\pi q_0} - \frac{m_\pi^2 m_0}{\pi q_0^3}. \tag{60}$$

The function $h(m)$ is given by

$$h(m) = \frac{2q}{\pi m}\ln\left(\frac{m + 2q}{2m_\pi}\right), \tag{61}$$

with

$$\frac{dh}{dm}\Big|_{m_0} = h(m_0)[(8q_0^2)^{-1} - (2m_0^2)^{-1}] + (2\pi m_0^2)^{-1}. \tag{62}$$

The GS propagator is used as the lineshape for the $\rho(770)^0$, $\rho(1450)^0$ and $\rho(1700)^0$ resonances instead of the RBW propagator in this analysis.

6.2 K-matrix

The RBW propagator provides a good description of the resonances only if they are relatively narrow and isolated from other resonances with the same spin, which is also the limit of the traditional isobar model constructed from a series of quasi-two body resonances. When describing the amplitude of overlapping resonances, such as the isoscalar $\pi\pi \to \pi\pi$ scattering involving the contributions of various f_0 resonances, different effects instead of a single resonant contribution have been seen. The description will suffer from the non-resonant amplitude interfering with the resonance. Each resonance can also have a strong coupling between the scattering processes in different channels. For example, the first resonance $f_0(980)$ can strongly couple to the KK scattering channel, which causes a rapid decrease of the amplitude in the $f_0(980)$ mass pole [75]. The sum of the individual resonant contributions can not describe such a system precisely and will violate the unitarity. The K-matrix [76] formalism is then introduced as an alternative, which considers all the possible channels to which the resonance couples, and is constructed to preserve unitarity. The K-matrix was traditionally used for describing the scattering process. For decays, the production process is considered instead, which is described by the production vector. Under such formalism, the propagator describing the production amplitude is written as

$$\mathcal{T} = (I - i\hat{\rho}\hat{K})^{-1}\hat{P}, \tag{63}$$

where I is the identity matrix and $\hat{\rho}$ is the phase space density matrix, of which the elements describe the density behaviour of the coupled channels. $\hat{K}$ is then the $n \times n$ K matrix describing all the resonant components and the non-resonant scattering processes, where n is the number of the coupled channels. $\hat{P}$ is the production vector describing the coupling between the initial state to the pole. It is constrained to have the same pole structure as $\hat{K}$ to ensure that the amplitude will not vanish at the K-matrix pole. For two body channels, $\hat{\rho}$ is expressed as [76]

$$\hat{\rho}(m) = \sqrt{\left(\frac{m_0^2 - (m_1 + m_2)^2}{m_0^2}\right)\left(\frac{m_0^2 - (m_1 - m_2)^2}{m_0^2}\right)}, \tag{64}$$

where m_1 and m_2 are the corresponding masses of the final state particles. In this analysis of the $D^0 \to \pi^-\pi^+\pi^0$ decay, the $\pi\pi$ S-wave is described by the K-matrix in the amplitude model which shows a complicated structure with overlapping resonances. It is mainly constructed with five different poles associated with the $f_0(980)$, $f_0(1300)$, $f_0(1500)$, $f_0(1200 - 1600)$ and $f_0(1750)$ resonances, as well as five coupled channels of $\pi\pi$, KK, $\pi\pi\pi\pi$, $\eta\eta$ and $\eta\eta'$. The K-matrix is then defined as a 5×5 matrix using the parametrisation taken from Ref [77] as

$$\hat{K}_{ij}(m) = f(m)\left(\sum_\alpha \frac{g_{\alpha i}g_{\alpha j}}{m_\alpha^2 - m^2} + f_{ij}^{scatt}\frac{1 \text{ GeV}^2/\text{c}^4 - s_0^{scatt}}{m^2 - s_0^{scatt}}\right), \tag{65}$$

where $i, j(\alpha) = 1, 2, 3, 4, 5$ indicate the five coupled channels (poles). The factors $g_{\alpha i(j)}$ are the relevant coupling constants describing the strength between the coupled channel i and the pole α. The second term of Equation 65 describes the non-resonant scattering contributions in terms of f_{ij}^{scatt}, the parametrisation of which is taken from Ref [78]. In addition to the general production amplitudes, there is also an unphysical singularity under the $\pi\pi$ threshold, sometimes known as the Adler zero [79]. The term $f(m)$ is introduced to suppress such singularity, which is defined as [80]

$$f(m) = \frac{1 \text{ GeV}^2/\text{c}^4 - s_{A0}}{m^2 - s_{A0}}\left(m^2 - s_A\frac{m_\pi^2}{2}\right), \tag{66}$$

where s_{A0} is fixed to be $-0.15 \text{ GeV}^2/\text{c}^4$ and $s_A = 1$. The production vector specific for such process is expressed as

$$\hat{P}_i(m) = \sum_\alpha \frac{\beta_\alpha g_{\alpha i}}{m_\alpha^2 - m^2} + f_i^{prod}\frac{1 \text{ GeV}^2/\text{c}^4 - s_0^{prod}}{m^2 - s_0^{prod}}, \tag{67}$$

where the complex production coupling β_α is used to describe the production strength of the pole α. The f_i^{prod} is the complex parameter used to describe the direct coupling

to channel i. These parameters are all dependent on the experiment. The general
production vector thus has 20 degrees of freedom that should be left floating in the
amplitude fit. The parameters used in the K-matrix are all fixed in the fit based on a
previous dedicated scattering measurement, which is summarised in Table 6.1.

Table. 6.1:   The fixed parameters in the K-matrix, taken from Ref [77].

m_α	$g^\alpha_{\pi^+\pi^-}$	$g^\alpha_{K\bar{K}}$	$g^\alpha_{\pi\pi\pi\pi}$	$g^\alpha_{\eta\eta}$	$g^\alpha_{\eta\eta'}$
0.65100	0.22889	-0.55377	0.00000	-0.39899	-0.34639
1.20360	0.94128	0.55095	0.00000	0.39065	0.31503
1.55817	0.36856	0.23888	0.55639	0.18340	0.18681
1.21000	0.33650	0.40907	0.85679	0.19906	-0.00984
1.82206	0.18171	-0.17558	-0.79658	-0.00355	0.22358
	f^{scatt}_{11}	f^{scatt}_{12}	f^{scatt}_{13}	f^{scatt}_{14}	f^{scatt}_{15}
	0.23399	0.15044	-0.20545	0.32825	0.35412
	f^{scatt}_{21}	f^{scatt}_{31}	f^{scatt}_{41}	f^{scatt}_{51}
	0.15044	-0.20545	0.32825	0.35412
		s^{scatt}_0	s_{A_0}	s_A
		-3.92637	-0.15	1

6.3   Formalism of the amplitude fitting

Considering the large size of the data sample, efficient computing of the amplitude
is necessary for performing the fit within a reasonable timescale. The AmpGen frame-
work [56] is chosen to perform the amplitude fit. This is a software package based on
the Minuit INTerface (MINT) Fitter [81] used for amplitude analyses of three and four
body pseudoscalar decays. It has been developed and is broadly used within the LHCb
collaboration. The AmpGen framework has the advantage of flexible definition of the
free parameters in the dynamic structure of the amplitude (masses, widths, etc.), with a
much faster evaluation than the original MINT fitter [32]. Using the AmpGen package,
a maximum likelihood unbinned fit is then performed on the combined resolved and
merged data sample, where the complex magnitude of each amplitude, as well as the
masses and the widths of the intermediate resonance in some cases, are be extracted as
the result.

The typically used PDFs for the amplitude fit consist of the signal amplitude model as well as the possible background contribution, which is written in terms of the phase space (x) as

$$P(x) = \epsilon(x)R_3(x)[f_s P_s(x) + f_b P_b(x)], \qquad (68)$$

where $\epsilon(x)$ is the phase space acceptance obtained from the simulation sample. $R_3(x)$ is the corresponding three body phase space density and $P_s(x) = |\mathcal{A}(x)|^2$ is the normalised signal PDF based on the total amplitude $\mathcal{A}(x)$, where the normalisation is based on the integral over the phase space. $f_i = \frac{Y_i}{N_i}, (i = s, b)$ represents the fraction for different components obtained from the integral of the PDF over the phase space N_i weighted by the fractional yield Y_i obtained in the Δm fit in Chapter 5.5. $P_b(x)$ generally describes the combinatorial background underneath the signal region, while in this analysis the S-weight is applied to the data sample to avoid the parametrisation of the background component. Thus, the total PDF is written as

$$P(x) = \epsilon(x)R_3(x)(f_s|S(x)|^2). \qquad (69)$$

The likelihood used in the fit is then expressed as

$$\mathcal{L}_{P(x)} = -2 \sum_{x \in data} (\log(P(x)) - \log(R_3(x)\epsilon(x))) = -2 \sum_{x \in data} \log\Big(\frac{P(x)}{R_3(x)\epsilon(x)}\Big). \qquad (70)$$

Such likelihood is used to cancel the effect of the signal efficiency as well the phase space density on $P(x)$, which avoids the explicit parametrisation of the efficiency map across the phase space in the amplitude model and thus simplifies the fitting procedure. The normalisation is then computed based on the MC integration using a fully simulated MC sample, which is written as

$$I = \int \epsilon(x)P(x)dx \approx \frac{1}{N_{mc}} \sum_{i=0}^{N_{mc}} \frac{P(x)}{\mathcal{A}_{gen}(x_i)}, \qquad (71)$$

where N_{mc} represents the number of events in the integration sample. $\mathcal{A}_{gen}$ is the relevant

PDF which the MC sample is generated with. Note that the dependence on the signal efficiency has been cancelled out in the MC sample, which has been propagated through the full reconstruction and the same selection processes as data. The technique of the MC integration avoids the explicit form of the efficiency map, whereas the accuracy of the integration strongly relies on the size of the MC sample and the reliability of $\mathcal{A}_{gen}$. The variance of the normalisation integral is written as

$$\text{Var}(I) = \frac{1}{N_{mc}} \sum_{i=0}^{N_{mc}} \left(\frac{P(x)}{\mathcal{A}_{gen}(x_i)}\right)^2 - \left(\frac{1}{N_{mc}} \sum_{i=0}^{N_{mc}} \frac{P(x)}{\mathcal{A}_{gen}(x_i)}\right)^2. \tag{72}$$

To minimise the uncertainty of the integral given as $\sigma(I) = \sqrt{\text{Var}(I)/I}$, the signal model used in the MC simulation sample is then required to be close to the signal PDF in the data sample as $A_{gen} \approx A(x)$. The current MC simulation sample used in this analysis is generated based on the BaBar model, which is close to the data distribution but shows some discrepancies in the Dalitz projections. In the future, the MC integration will be based on our preliminary amplitude model, which will further reduce the relevant systematic uncertainty.

The complex magnitudes of each amplitude extracted after the fit intrinsically depend on the choice of the convention and normalisation in the formalism, which is inconvenient when compared with the other amplitude model based on different conventions. The fit fraction is then introduced to describe the relative component of each amplitude as a convention-independent variable. It is defined as the integration of the squared modulus of the corresponding amplitude over the phase space normalised by the integral of the coherent sum of all amplitudes over the phase space, which can be written as

$$FF_i = \frac{\int_{DP} |a_i e^{i\delta_i} \mathcal{A}_i(m_{ab}^2, m_{ac}^2)|^2 dm_{ab}^2 dm_{ac}^2}{\int_{DP} |\sum_j a_j e^{i\delta_j} \mathcal{A}_j(m_{ab}^2, m_{ac}^2)|^2 dm_{ab}^2 dm_{ac}^2}. \tag{73}$$

The sum of the total fit fractions could differ from unity as a result of interferences between the amplitudes. The system then extends to the fit fractions for each interference component, which is defined as the integration of two particular components over the phase space with the normalisation used previously. It is expressed as

$$FF_{ij} = \frac{\int_{DP} 2\text{Re}[a_i e^{i\delta_i} a_j e^{j\delta_i} \mathcal{A}_i(m_{ab}^2, m_{ac}^2) \mathcal{A}_j^*(m_{ab}^2, m_{ac}^2)] dm_{ab}^2 dm_{ac}^2}{\int_{DP} |\sum_k a_k e^{i\delta_k} \mathcal{A}_k(m_{ab}^2, m_{ac}^2)|^2 dm_{ab}^2 dm_{ac}^2}. \tag{74}$$

The sum of all fit fractions is then constrained to be 100% by construction. The quality of the amplitude fit is evaluated by performing a χ^2-test over the input Dalitz plot using an adaptive binning method [57], which aims to keep a sufficient number of events in each bin to calculate the χ^2. In such a scheme, the total phase space is firstly split into bins equivalently with the number of 2^{dn}, where d is the degree of the freedom and n is the selected integer. The binning process then loops over every dimension to split the bins with event numbers greater than the minimum population into two smaller bins with approximately the same number of events. This adaptive binning finally ensures all the events are uniformly distributed in each bin, with an adaptive scale corresponding to the event density. The χ^2 is then defined as

$$\chi^2 = \sum_{i \in bins} \frac{(N_i - \langle N_i \rangle)}{N_i + \bar{\sigma}_i^2}, \tag{75}$$

where N_i is the number of data candidates in bin i, and $\langle N+i \rangle$ is the expected number of events in the same bin. $\langle N+i \rangle$ is determined from the MC integration sample weighted by the fitted PDF

$$\langle N_i \rangle = \sum_{j \in bin(i)} \omega_j, \tag{76}$$

where ω_j is the weight for the MC integration event j in bin i, and $\bar{\sigma}_i$ is then the statistical uncertainty of $\langle N_i \rangle$, given by

$$\bar{\sigma}_i = \sum_{j \in bin(i)} \omega_j^2. \tag{77}$$

By convention, the χ^2/ndf is selected to evaluate the quality of the amplitude fit, where the number of degrees of freedom (ndf) is given by

$$N_{dof} = N_{bins} - N_{parameters} - 1. \tag{78}$$

6.4 Model building

The final amplitude model contains the resonant contributions of the ρ, $\omega(782)$ and $f_2(1270)$ resonances, and the non-resonant $\pi\pi$ S-wave contribution described by the K-matrix formalism. Based on the limited spin configurations of each amplitude, all the Blatt-Weisskopf form factors and the Zemach spin factors can be calculated during the construction of the corresponding amplitudes, while the effective radius used in the barrier factor is cited from the PDG [14]. The other lineshape parameters are also fixed to their PDG value, which are summarised in Table 6.2. However, the initial magnitude and phase for each amplitude are unknown at the beginning of the procedure. To constrain the amplitude fit to a reasonable range, the BaBar model is chosen to describe the narrow resonances at the first stage, of which the largest component corresponds to the $\rho^+(770)$ resonance. The magnitude and phase of the $\rho^+(770)$ resonance are thus fixed to one and zero in the following fit, which ensures the measurement of all other magnitudes are all relative to the $\rho^+(770)$ contribution. The further fitting procedure can be described as follows:

1. Perform the initial fit to the data where all the complex coefficients of the narrow resonances described by the BaBar model are set to be free. The coefficients for other amplitudes including the K-matrix are fixed to unity. This step is used to obtain a relatively reasonable agreement between the amplitude model and the data.

2. Based on the initial fit result, fix the coefficients of the resonances and free the K-matrix parameters. This step is used to better describe the non-resonant component.

3. Free all the coefficients for the resonances and K-matrix based on the fit result from the previous step. The optimisation of the model is also performed by refitting the data without components with the least fit fractions. The result with the minimised quantity $FCN = -2\log\mathcal{L}$ is then selected as the final amplitude model.

Table. 6.2: List of resonant contributions including their spin, lineshape used and mass and width according to the PDG values [14]. The RBW in the lineshape indicates the relativistic Breit-Wigner propagator, while the GS indicates the Gounaris-Sakurai propagator.

Resonance	Spin	Lineshape	$m(\mathrm{MeV}/c^2)$	$\Gamma(\mathrm{MeV}/c^2)$
$\rho^0(770)$	1	GS	775.26	149.1
$\rho^\pm(770)$		RBW		
$\rho^0(1450)$	1	GS	1465	400
$\rho^\pm(1400)$		RBW		
$\rho^0(1700)$	1	GS	1720	250
$\rho^\pm(1700)$		RBW		
$\omega(782)$	1	RBW	782.65	8.49
$f_2(1270)$	2	RBW	1275.5	186.7

6.5 Resulting preliminary model

The preliminary fit result is shown in three Dalitz projections in Figure 6.1 compared with the data distribution, where the resulting parameters, as well as the fit fractions of each component, are summarised in Table 6.3. The summary of the fit fractions for each interference component is shown in Appendix B. Note that the contribution from the $\omega(782)$ resonance has been removed due to its extremely small fit fraction. From the comparison with the data sample, reasonable agreement is observed for most distributions, while some discrepancies are found near the $\rho(770)$ resonance and in the tail of the $\pi^+\pi^-$ projection. The large excess of the sum of the fit fractions over 100% implies large interference contributions, which is expected compared with the BaBar model but also possibly shows a sign of non-physical amplitudes cancelling each other.

The main difference with the BaBar model comes from the parametrisation of the non-resonant $\pi^+\pi^-$ S-wave amplitude, which is described by the simple sum of all resonance contributions involving the various f_0 resonances ($\sigma(500)$, $f_0(980)$, $f_0(1370)$, $f_0(1500)$ and $f_0(1710)$). Though such formalism is unsuitable to use, as discussed in Chapter 6.2, we can describe the $\pi^+\pi^-$ S-wave similarly to the Quasi-Model-Independent Partial Wave Analysis (QMIPWA) [82] instead of using the K-matrix. The QMIPWA model describes the $\pi^+\pi^-$ S-wave in terms of sub-intervals (knots). The individual
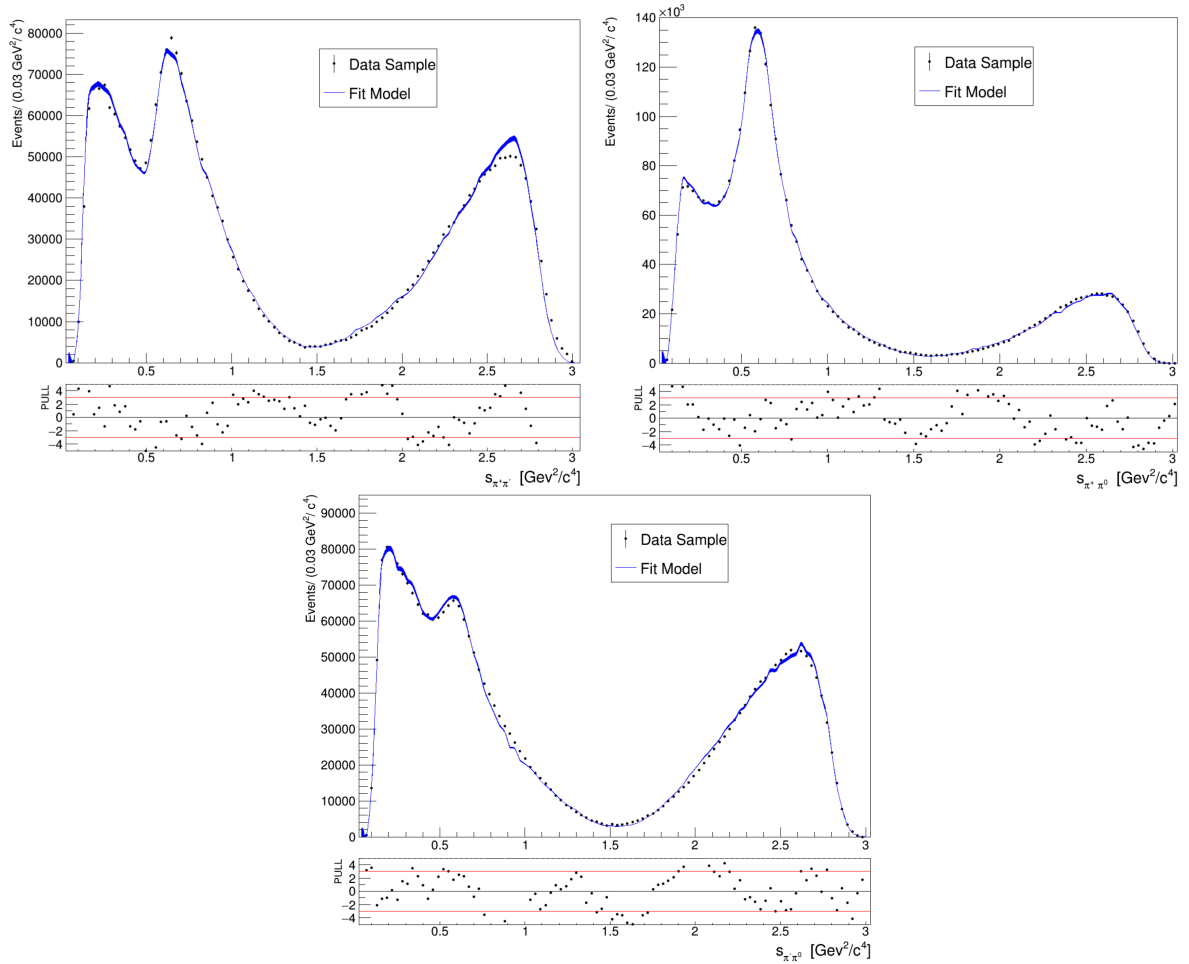
Figure. 6.1: Distribution of the Dalitz projections for data (dots with error bars) and the fit results based on the preliminary amplitude model (blue solid line with smoothed filled area of error bars).

Table. 6.3: The fit fractions, complex magnitudes of each amplitude and other variables obtained from the preliminary fit.

System	Resonance	$\mathcal{R}(a_r)$	$\mathcal{I}(a_r)$	Fit Fraction [%]
	$\rho^+(770)$	1.0 (fixed)	0.0 (fixed)	74.28 ± 0.11
	$\rho^0(770)$	0.5852 ± 0.0010	0.1529 ± 0.0009	26.88 ± 0.08
	$\rho^-(770)$	-0.7021 ± 0.0009	0.0115 ± 0.0011	40.25 ± 0.08
	$\rho^+(1450)$	0.0612 ± 0.0019	0.0303 ± 0.0020	0.34 ± 0.02
	$\rho^0(1450)$	0.0862 ± 0.0021	-0.0927 ± 0.0017	1.25 ± 0.04
	$\rho^-(1450)$	-0.0447 ± 0.0025	0.1662 ± 0.0020	2.10 ± 0.05
	$\rho^+(1700)$	0.1645 ± 0.0037	-0.0281 ± 0.0045	0.47 ± 0.02
	$\rho^0(1700)$	-0.0088 ± 0.0031	-0.1655 ± 0.0040	0.49 ± 0.02
	$\rho^-(1700)$	0.0124 ± 0.0035	0.1729 ± 0.0050	0.51 ± 0.03
	$f_2(1270)$	0.1356 ± 0.0011	0.1508 ± 0.0011	2.20 ± 0.02
$\pi\pi$ S-wave	β_1	0.4597 ± 0.0053	0.1591 ± 0.0060	1.93 ± 0.02
	β_2	0.1705 ± 0.0045	0.2077 ± 0.0051	
	β_3	-0.0458 ± 0.0053	-0.0186 ± 0.0049	
	β_4	-0.2803 ± 0.0094	-0.4619 ± 0.0096	
	f_{11}^{prod}	-0.1722 ± 0.0054	-0.2081 ± 0.0053	
	f_{12}^{prod}	-1.4249 ± 0.0215	0.0094 ± 0.0230	
	f_{13}^{prod}	-1.1596 ± 0.0281	-1.8541 ± 0.0272	
	f_{14}^{prod}	-0.8311 ± 0.0175	-0.5303 ± 0.0182	
	Sum of Fit Fractions	1.5074 ± 0.0017		
	χ^2/ndf	175963/131033 = 1.3429		

amplitude for each knot is then constructed by the isobar model, which refers to the coherent sum of all resonance contributions involving the various f_0 resonances. Though the QMIPWA model shows a good description around the tail with a more uniform distribution, it shows a slight shift over the narrow resonance of the P-wave components as well as a distortion of the shape, particularly in the $\rho^0(770)$ region. Such discrepancy could originate from the limitation of the isobar model to describe the higher components resulting in the mis-parametrisation of the S-wave, or from the inappropriate selection of the binning scheme, which will decrease the fit quality without enough knots, or promote the instability of the S-wave with too many knots in the specific region.

The other characteristic of the fit result is the non-smooth distribution in some specific regions, which indicates a bad normalisation from the MC integration. This

could originates from the limited size of the MC sample used in the analysis, which promotes the statistical instability of some bins in the efficiency map. Finally, the non-perfect agreement between the fully-simulated sample and the data sample can result in an inaccuracy of the efficiency map, as the reconstruction and detector effects strongly depend on the kinematics of the particle candidates.

The current model is in no way final. There are still plenty of alternative models with extra structures or better constraints on the presented amplitudes waiting for further tests, while the complicated interference picture requires a thorough study of the lineshape of each amplitude. The effect of the finite detector resolution will introduce higher uncertainty on the measurement of the invariant mass combination, causing the migration of events between bins over the Dalitz Plot. It will affect the precise description of the efficiency map, especially in the case of the decay involving π^0 as it suffers from a worse resolution of reconstruction. Besides, the loop of amplitude fits with randomised initial values should be also performed for each possible model to avoid local minima, where only the converged fit with the smallest negative likelihood is chosen as the final fitting result. While we have excluded the $\omega(782)$ contribution parameterised by the RBW lineshape, its effect could cause the distortion of the $\rho(770)^0$ lineshape and create an interference pattern. Such effect could be parameterised by implementing the $\rho - \omega$ mass mixing amplitude:

$$\mathcal{T}_{\rho-\omega} = \mathcal{T}_\rho \Big[\frac{1 + \mathcal{T}_\omega \Delta |B| e^{i\phi_B}}{1 - \Delta^2 \mathcal{T}_\rho \mathcal{T}_\omega} \Big], \tag{79}$$

where $\mathcal{T}_\rho$ ($\mathcal{T}_\omega$) is the ρ (ω) lineshape, $|B|$ and ϕ_B are the relative magnitude and phase of the interference pattern, and $\Delta = \delta(m_\rho + m_\omega)$ where δ governs the electromagnetic mixing of ρ and ω from $e^+ e^- \to \pi^+ \pi^-$ []. All of these new effects or models will be included in our future work.

Chapter 7

Systematic uncertainties

In this amplitude analysis, a series of sources are considered as systematic uncertainties. The systematic uncertainties in the fit are mainly from the mis-modelling of the efficiency correction and the description of the resonances, which are all summarised in Tables 7.1 and 7.2. For the uncertainties evaluated by comparing two different fit results based on the same sample, the systematic uncertainties are computed as

$$
\sigma_r^{\text{syst}} = \begin{cases} ||a_r^1| - |a_r^2|| \\ |\arg\left(a_r^1\right) - \arg\left(a_r^2\right)| \\ |\mathcal{F}_r^1 - \mathcal{F}_r^2|, \end{cases} \tag{80}
$$

where $|a_r|$, $arg(a_r)$ and $\mathcal{F}$ are the relevant modulus, phase and fit fraction of the amplitude r.

For the uncertainties evaluated by comparing various slightly different models based on 100 independent fits, the resulting spread of each parameter σ_r is taken as the systematic uncertainty

$$
\sigma_r^{\text{syst}} = \sigma_r. \tag{81}
$$

Note that in this analysis, all the systematic uncertainties are preliminary due to the imperfect construction of the amplitude model. The full analysis of the systematic

uncertainties will be finalised in future work.

7.1   Selection efficiency

The variation of the phase space acceptance has been accounted for by using a MC sample reconstructed after all the same selection criteria as the data sample. However, as the simulation can not perfectly model the data, which means the efficiency correction can introduce possible bias on the amplitude fit, a relevant systematic uncertainty is necessary to be assigned. To study this, we can split the data set into equally populated bins in the transverse momentum distribution of the D^0 candidate, which is a key variable for evaluating the signal efficiency. We can then fit each of these subdata samples individually using the same model and combine the fit results statistically, where the spread of the results is taken as the variation due to the efficiency. The difference between the baseline fit compared with the combined result is then assigned as the relevant systematic uncertainty, which is calculated based on Equation 80.

7.2   Background description

Uncertainties can arise due to the imperfect background cancellation with the S-weight technique, which originates from the imperfect agreement between the signal and background component in the Δm fit. In order to assign a systematic uncertainty to take this effect into account, 100 independent re-fits on the data are performed with the S-weight regenerated by resampling each bin in the original distribution using Poisson fluctuation. The resulting spread of the these fits is then taken as the relevant systematic uncertainty calculated according to Equation 81.

7.3   Resonance description

There are specific choices made for the description of the resonances. To assign the relevant systematic uncertainty to the selection of the resonance model, we use

alternative parametrisation.

- The possible systematic uncertainty due to the Gounaris-Sakurai description for the $\rho(770)^0$, $\rho(1450)^0$ and $\rho(1700)^0$ resonances is tested using the RBW lineshape instead. The difference between the baseline result and the modified one calculated according to Equation 80 is used to compute the systematic uncertainty.

- The K-matrix description of the $\pi\pi$ S-waves is tested using an alternative parametrisation from Ref [77]. The maximum difference between the two parameter sets using Equation 80 is taken as the systematic uncertainty.

- To estimate the systematic uncertainty due to the choice of the resonance masses and widths which are fixed in the fit, 100 independent fits are performed on the data. In each fit, the resonance masses and widths are floated based on a Gaussian distribution with the mean and the width taken as the central value and uncertainty cited from the PDG [14]. The relevant differences computed from Equation 81 are assigned as systematic uncertainties. These mainly originate from the less known resonances with large uncertainties such as $\rho^0(1700)$.

More relevant systematic uncertainties are needed to be studied, including the limited size of the integration sample, the radius used for the D^0 meson, the final choice of amplitude model, the fit bias and the possible systematic uncertainties on the CP violation measurement. All of these uncertainties will be studied in the future after the final CP-averaged model is developed.

Table. 7.1: Statistical and systematic uncertainties on the fit parameters shown for all floating components. Values smaller than 0.0005 are displayed as "0.000". The sources of systematic uncertainty are described in the text in the same order as shown in this table. For each amplitude, the first (second) value quoted is the real (imaginary) part of the complex fit parameter.

Amplitude	Stat.	Total Syst.	Sel Eff	BKG	RBW	Alt K-matrix	Mass width
$D^0 \to \rho^0(770)\pi^0$	0.001	0.027	0.027	0.003	0.001	0.002	0.001
	0.001	0.018	0.008	0.003	0.010	0.011	0.004
$D^0 \to \rho^-(770)\pi^+$	0.001	0.018	0.016	0.001	0.000	0.006	0.004
	0.001	0.021	0.011	0.001	0.003	0.019	0.003
$D^0 \to \rho^+(1450)\pi^-$	0.002	0.030	0.015	0.009	0.000	0.018	0.018
	0.002	0.756	0.168	0.010	0.136	0.048	0.722
$D^0 \to \rho^0(1450)\pi^0$	0.002	0.039	0.019	0.001	0.009	0.015	0.029
	0.028	0.431	0.343	0.001	0.034	0.027	0.255
$D^0 \to \rho^-(1450)\pi^+$	0.003	0.039	0.018	0.003	0.008	0.010	0.031
	0.002	0.311	0.174	0.003	0.024	0.013	0.255
$D^0 \to \rho^+(1700)\pi^-$	0.004	0.059	0.043	0.005	0.016	0.023	0.027
	0.005	0.305	0.297	0.005	0.051	0.044	0.018
$D^0 \to \rho^0(1700)\pi^0$	0.003	0.076	0.047	0.004	0.011	0.026	0.053
	0.004	0.378	0.331	0.004	0.066	0.120	0.120
$D^0 \to \rho^-(1700)\pi^+$	0.004	0.048	0.038	0.001	0.007	0.017	0.022
	0.005	0.245	0.039	0.001	0.100	0.164	0.146
$D^0 \to f_2(1270)\pi^0$	0.001	0.010	0.009	0.001	0.000	0.005	0.000
	0.001	0.049	0.019	0.002	0.003	0.028	0.035

Table. 7.2: Statistical and systematic uncertainties on the fit fractions (%). Values smaller than 0.0005 are displayed as "0.000".

Amplitude	Stat.	Total Syst.	Sel Eff	BKG	RBW	Alt K-matrix	Mass width
$D^0 \to \rho^+(770)\pi^0$	0.112	1.150	0.051	0.238	0.044	1.122	0.013
$D^0 \to \rho^0(770)\pi^0$	0.087	1.883	1.846	0.136	0.131	0.077	0.311
$D^0 \to \rho^-(770)\pi^+$	0.088	2.475	2.433	0.049	0.024	0.159	0.421
$D^0 \to \rho^+(1450)\pi^-$	0.182	0.293	0.177	0.074	0.004	0.085	0.204
$D^0 \to \rho^0(1450)\pi^0$	0.043	0.719	0.401	0.013	0.133	0.268	0.516
$D^0 \to \rho^-(1450)\pi^+$	0.055	0.876	0.417	0.026	0.217	0.274	0.688
$D^0 \to \rho^+(1700)\pi^-$	0.021	0.599	0.139	0.059	0.086	0.119	0.562
$D^0 \to \rho^0(1700)\pi^0$	0.024	0.257	0.163	0.035	0.061	0.137	0.126
$D^0 \to \rho^-(1700)\pi^+$	0.030	0.515	0.487	0.010	0.049	0.121	0.107
$D^0 \to f_2(1270)\pi^0$	0.017	0.267	0.192	0.020	0.007	0.181	0.033
$D^0 \to (\pi^+\pi^-)_{L=0})\pi^0$	0.023	0.458	0.436	0.064	0.000	0.122	0.042

Chapter 8

Conclusions

In this thesis, the preliminary amplitude analysis of the decay $D^0 \to \pi^-\pi^+\pi^0$ is performed. The analysis is based on the data set taken during the LHCb Run-II period from 2015-2018 with $\sqrt{s} = 13$ TeV, corresponding to an integrated luminosity of $\mathcal{L} = 5.7$ fb^{-1}. Using the S-weight technique and an MVA-based classifier to discriminate the signal candidates from the combinational background contamination, we obtain a relatively clean signal sample with 1642168 (746618) and a significance of 1181.5 (810) for the resolved (merged) sample, which is then used as the input to the amplitude fit. The resulting preliminary amplitude model provides a relatively precise description of the $D^0 \to \pi^-\pi^+\pi^0$ intermediate resonant structures. The fit is performed by the AmpGen package using an unbinned maximum likelihood fit. The final data sample distributions will be distorted because of experimental effects. Thus, the variation of the phase space acceptance due to these effects and the reconstruction is extracted from the fully simulated MC samples according to the BaBar model. These samples are used in the determination of the normalisation of the likelihood function based on the MC integration.

In the current model, a total of 11 decay amplitudes have been identified. The most prominent being the decay $D^0 \to \rho^+(770)\pi^0$, followed by the $D^0 \to \rho^-(770)\pi^0$ and $D^0 \to \rho^0(770)\pi^0$ decay, altogether contributing 140% of the total decay rate, which is consistent with the main results found in Ref [17], but gives an improved description

of the amplitude model with a larger data sample. The complicated $\pi^+\pi^-$ S-wave comprising multiple broad overlapping resonances and the coupling to various mass poles is interpreted using the K-matrix formalism, based on global $\pi\pi$ scattering data [77]. The QMIPWA technique is tested as an alternative method to describe the S-wave knots by knots, and this results in a qualitative limited model compared with the K-matrix. The main systematic uncertainties related to the resonance description and the efficiency extraction have been estimated. Some of these uncertainties will suffer from the possible over-estimation due to the imperfect description of the amplitude model. Other relevant uncertainties, including the fit bias, the alternative models and the numerical integration will also be considered in the future.

Due to the fact that the amplitude model can be further improved, the formal search for CP violation based on the LHCb Run-II data set has been postponed until the final amplitude model is selected. However, we have investigated the needed theoretical approach and the relevant experimental techniques to measure the CP asymmetries for each component in the final amplitude model. This analysis developed during the MSc period is the first phase of the project, which will be continued as a PhD project.

8.1   Prospects

Further studies involve a better description of the current model. These are required to identify the high resonant contributions to the interference term as well as the high mass region of the $\pi^+\pi^-$ system ($s_{\pi^+\pi^-} > 1.5\text{GeV}^2/c^4$). In particular, a more precise constraint on the masses and widths of the resonances is necessary to fit the distribution. Other possible high mass resonances such as $f_2'(1525)$ can be introduced further to better describe the tail. In addition, the shift of the mass peak in the $\rho^0(770)$ region has to be further investigated. This could arise due to isospin violating interactions in $\omega(782) \to \pi^+\pi^-$ [83], which will result in a distortion of the $\rho^0(770)$ lineshape.

Except for the resonant structure, one of the necessary further studies is the re-optimisation of the efficiency map, which suffers from the limited sample size of the

current MC simulation sample. The agreement between the simulation and real data distributions can also be improved. A larger MC simulation production request based on our preliminary model is being proposed, and this will significantly improve the accuracy of our efficiency correction used in the future amplitude fit. The search for CP violation based on the final CP averaged model will be the main goal of my PhDs project. Once the best amplitude model is constructed, we will measure the CP asymmetries related to the amplitude modulus, phases and fit fractions, using the method shown in Chapter 4.

Appendix A

Alternative K-matrix description

In addition to the baseline solution of the K-matrix description we use in the default amplitude fitting, two other solutions have been also published in Ref [77]. They are described in Tables A.1, A.2.

Table. A.1: The alternative solution I of the parameters in the K-matrix.

m_α	$g^\alpha_{\pi^+\pi^-}$	$g^\alpha_{K\bar{K}}$	$g^\alpha_{\pi\pi\pi\pi}$	$g^\alpha_{\eta\eta}$	$g^\alpha_{\eta\eta'}$
0.7369	0.31896	-0.49998	0.00000	-0.21554	-0.18294
1.24347	0.85963	0.52402	0.00000	0.38093	0.23788
1.62681	0.47993	0.40254	1.00000	0.21811	0.05454
1.21900	0.45121	0.42769	1.15088	0.22925	-0.06444
1.74932	0.39391	-0.30860	0.33999	0.06919	0.22358
	f^{scatt}_{11}	f^{scatt}_{12}	f^{scatt}_{13}	f^{scatt}_{14}	f^{scatt}_{15}
	-0.050	0.250	-0.540	0.440	0.320
		f^{scatt}_{21}	f^{scatt}_{31}	f^{scatt}_{41}	f^{scatt}_{51}
		0.250	-0.540	0.440	0.320
			s^{scatt}_0	s_{A_0}	s_A
			-3.92637	-0.15	1

Table. A.2: The alternative solution II of the parameters in the K-matrix.

m_α	$g^\alpha_{\pi^+\pi^-}$	$g^\alpha_{K\bar{K}}$	$g^\alpha_{\pi\pi\pi\pi}$	$g^\alpha_{\eta\eta}$	$g^\alpha_{\eta\eta'}$
0.67460	0.26014	-0.57849	0.00000	-0.32936	-0.30906
1.21094	0.95289	0.55887	0.00000	0.39910	0.31143
1.57896	0.46244	0.31712	0.70340	0.22963	0.19802
1.21900	0.41848	0.49910	0.96819	0.24415	-0.00522
1.86602	0.01804	-0.28430	-0.90100	-0.07252	0.17097
	f^{scatt}_{11}	f^{scatt}_{12}	f^{scatt}_{13}	f^{scatt}_{14}	f^{scatt}_{15}
	0.050	0.100	-0.350	0.360	0.320
		f^{scatt}_{21}	f^{scatt}_{31}	f^{scatt}_{41}	f^{scatt}_{51}
		0.100	-0.350	0.360	0.320
			s^{scatt}_0	s_{A_0}	s_A
			-3.92637	-0.15	1

Appendix B

Interference fractions

Table. B.1: The interference fractions [%] between amplitude components. Values smaller than 0.005 are displayed as "0.00"

	$\rho^+(770)$	$\rho^0(770)$	$\rho^-(770)$	$\rho^+(1450)$	$\rho^0(1450)$	$\rho^-(1450)$	$\rho^+(1700)$	$\rho^0(1700)$	$\rho^-(1700)$	$f_2(1270)$	$\pi\pi$ S-wave
$\rho^+(770)$	74.28										
$\rho^0(770)$	-6.01	26.88									
$\rho^-(770)$	-15.51	-4.34	40.25								
$\rho^+(1450)$	0.96	-0.43	-0.86	0.34							
$\rho^0(1450)$	1.16	-2.30	0.71	-0.04	1.25						
$\rho^-(1450)$	2.48	1.84	-3.38	0.06	-0.54	2.10					
$\rho^+(1700)$	-0.82	0.79	-0.82	0.01	-0.29	0.01	0.47				
$\rho^0(1700)$	1.45	-0.82	0.88	0.14	-0.06	0.14	0.00	0.49			
$\rho^-(1700)$	1.48	0.92	-0.12	0.12	-0.08	0.12	-0.01	0.00	0.51		
$f_2(1270)$	0.51	-0.01	-0.36	-0.13	-0.01	-0.14	-0.04	-0.00	-0.18	2.20	
$\pi\pi$ S-wave	-2.01	-0.02	1.43	-0.25	-0.01	-0.25	0.13	0.02	-0.32	0.02	1.93

Bibliography

[1] Y. Fukuda *et al.* (Super-Kamiokande Collaboration), *Evidence for oscillation of atmospheric neutrinos*, Phys. Rev. Lett. **81** 1562 (1998).

[2] Q. R. Ahmad *et al.* (SNO Collaboration), *Direct evidence for neutrino flavor transformation from neutral-current Interactions in the Sudbury Neutrino Observatory*, Phys. Rev. Lett. **89** 011301 (2002).

[3] S. Abe *et al.* (The KamLAND Collaboration), *Precision measurement of neutrino oscillation parameters with KamLAND*, Phys. Rev. Lett. **100** 221803 (2008).

[4] Y. Grossman, A. L. Kagan, Y. Nir, *New physics and CP violation in singly Cabibbo suppressed D decays*, Phys. Rev. D **75** 036008 (2007).

[5] S. Bianco, F. L. Fabbri, D. Benson, I. Bigi, *A cicerone for the physics of charm*, Riv.Nuovo Cim. 26N7, 1 (2003).

[6] R. Aaij *et al.* (LHCb Collaboration), *Observation of CP violation in charm decays*, Phys. Rev. Lett. **122** 21 (2019).

[7] M. Artuso. B. Meadows, A. A. Petrov, *Charm meson decays*, *Ann.Rev.Nucl.Part.Sci.* **58**, (2008) 249.

[8] M. Golden, B. Grinstein, *Enhanced CP violations in hadronic charm decays*, Phys. Lett. B **222**, 501 (1989).

[9] H.-n. Li, C.-D. Lu, and F.-S. Yu, *Branching ratios and direct CP asymmetries in $D \to PP$ decays*, Phys. Rev. D **86** 036012 (2012).

[10] D. Pirtskhalava and P. Uttayarat, *CP violation and flavor SU(3) breaking in D-meson decays*, Phys. Lett. B **712**, 81 (2012).

[11] Y. Grossman and D. J. Robinson, *SU(3) sum rules for charm decay*, JHEP **04** (2013) 067.

[12] F. Buccella, A. Paul, P. Santorelli, *SU(3)F breaking through final state interactions and CP asymmetries in $D \to PP$ decays*, Phys. Rev. D **99** 113001 (2019).

[13] E. Franco, S. Mishima, L. Silvestrini, *The Standard Model confronts CP violation in $D^0 \to \pi^+\pi^-$ and $D^0 \to K^+K^-$*, JHEP **05** (2012) 140.

[14] P. A. Zyla *et al.* (Particle Data Group), *Review of particle physics*, *PTEP* **2020** (2020) 083C01.

[15] R. Aaij *et al.* (LHCb Collaboration), *Measurements of CP violation in the three-body phase space of charmless $B^\pm$ decays*, Phys. Rev. D **90** 112004 (2014).

[16] R. Aaij *et al.* (LHCb Collaboration), *Search for CP violation in $D^0 \to \pi^-\pi^+\pi^0$ decays with the energy test*, Phys. Lett. B **740**, 158 (2015).

[17] B. Aubert *et al.* (BaBar Collaboration), *Measurement of CP violation parameters with a Dalitz plot analysis of $B^\pm \to D(\pi^+\pi^-\pi^0)K^\pm$*, Phys. Rev. Lett. **99** 251801 (2007).

[18] B. Aubert *et al.* (BaBar Collaboration), *Search for CP violation in neutral D meson Cabibbo-suppressed three-body decays*, Phys. Rev. D **78** 051102 (2008).

[19] Y. S. Amhis *et al.* (HFLAV), *Averages of b-hadron, c-hadron, and τ-lepton properties as of 2018*, Eur. Phys. J. C **81**, 226 (2021); arXiv:2206.07501 [Updates].

[20] S. L. Glashow, J. Iliopoulos, and L. Maiani, *Weak interactions with lepton-hadron symmetry*, Phys. Rev. D **2** 1285 (1970).

[21] C. S. Wu, E. Ambler, R. W. Hayward, D. D. Hoppes, and R. P. Hudson, *Experimental test of parity conservation in beta decay*, Phys. Rev. **105** 1413 (1957).

[22] J. H. Christenson, J. W. Cronin, V. L. Fitch, and R. Turlay, *Evidence for the 2π Decay of the K_2^0 Meson*, Phys. Rev. Lett. **13** 138 (1964).

[23] V. A. Kuzmin, V. A. Rubakov, M. E. Shaposhnikov, *On the anomalous electroweak baryon number nonconservation in the early universe*, Phys. Lett. B **155**, 36 (1985).

[24] A. G. Cohen, D. B. Kaplan, A. E. Nelson, *Progress in electroweak baryogenesis*, *Ann.Rev.Nucl.Part.Sci.* **43**, (1993) 27.

[25] A. D. Sakharov, *Violation of CP invariance, C asymmetry, and baryon asymmetry of the universe*, Soviet Physics Uspekhi **34** 392 (1991).

[26] B. Aubert *et al.* (Belle II Collaboration), *Measurement of CP violating asymmetries in B^0 decays to CP eigenstates*, Phys. Rev. Lett. **86** 2515 (2001).

[27] B. Abi *et al.* (DUNE Collaboration), *Prospects for beyond the Standard Model physics searches at the Deep Underground Neutrino Experiment*, Eur. Phys. J. C **81**, 322 (2021).

[28] B. Abi *et al.* (DUNE Collaboration), *CP properties of higgs boson interactions with top quarks in the $t\bar{t}H$ and tH processes using $H \to \gamma\gamma$ with the ATLAS detector*, Phys. Rev. Lett. **125** 061802 (2020).

[29] A. Hocker and Z. Ligeti, *CP violation and the CKM matrix*, Annual Review of Nuclear and Particle Science **56** 501 (2006)..

[30] O. Lupton, *Study of $D^0 \to K_s^0 h^+ h'^-$ decays at the LHCb experiment*, PhD thesis, University of Oxford, Jul 2016. Presented 14 Sep 2016.

[31] D. J. Herndon, P. Söding, and R. J. Cashmore, *Generalized isobar model formalism*, Phys. Rev. D **11** 3165 (1975).

[32] T. Evans, *Studies of the decays $D^0 \to K^\mp \pi^\pm \pi^\pm \pi^\mp$ at CLEO-c and LHCb*, PhD thesis, University of Oxford, Jul 2016. Presented 13 Sep 2017.

[33] K. Nakamura *et al.* (Particle Data Group), *Review of particle physics*, J. Phys. G **37**, 075021 (2010).

[34] F. von Hippel, C. Quigg, *Centrifugal-barrier effects in resonance partial decay widths, shapes, and production amplitudes*, Phys. Rev. D **5** 624 (1972).

[35] C. Zemach, *Three-Pion decays of unstable particles*, Phys. Rev. **133** B1201 (1964).

[36] V. Filippini, A. Fontana, A. Rotondi, *Covariant spin tensors in meson spectroscopy*, Phys. Rev. D **51** 2247 (1995).

[37] S. Dobbs *et al.* (CLEO Collaboration), *Dalitz analysis of the decay $D^0 \to K^-\pi^+\pi^0$*, Phys. Rev. D **63**, 092001 (2001).

[38] G. Breit, E. Wigner, *Capture of slow neutrons*, Phys. Rev. **49** 519 (1936).

[39] R. Aaij *et al.* (LHCb Collaboration), *The LHCb detector at the LHC*, *JINST* **3** (2008) S08005.

[40] G. Aad *et al.* (ATLAS Collaboration), *The ATLAS Experiment at the CERN Large Hadron Collider*, *JINST* **3** (2008) S08003.

[41] R. Adolphi *et al.* (CMS Collaboration), *The CMS experiment at the CERN LHC*, *JINST* **3** (2008) S08004.

[42] K. Aamodt *et al.* (ALICE Collaboration), *The ALICE experiment at the CERN LHC*, *JINST* **3** (2008) S08002.

[43] C. Elsasser, *$b\bar{b}$ production angle plots*, provided by the LHCb Speakers' Bureau.

[44] M. Alexander *et al.*, *Mapping the material in the LHCb vertex locator using secondary hadronic interactions*, *JINST* **13** (2018) P06008.

[45] R. Aaij *et al.* (LHCb Collaboration), *Design and performance of the LHCb trigger and full real-time reconstruction in Run 2 of the LHC*, *JINST* **14** (2019) P04013.

[46] R. Aaij *et al.* (LHCb Collaboration), *LHCb detector performance, Int.J.Mod.Phys.A* **30** (2015) 1530022.

[47] R. Aaij *et al.* (LHCb Collaboration), *Measurement of prompt charged-particle production in pp collisions at $\sqrt{s}$ = 13 TeV*, JHEP **01** (2022) 166.

[48] J. Gassner, M. Needham, O. Steinkamp, *Layout and expected performance of the LHCb TT station*, Technical Report: LHCb Note 2003-140, CERN, Geneva, Mar 2017.

[49] R. Arink *et al.* (LHCb Outer Tracker group), *Performance of the LHCb outer tracker*, *JINST* **9** (2014) P01002.

[50] C. A. Beteta *et al.* (LHCb Calorimeter group†), *Calibration and performance of the LHCb calorimeters in Run 1 and 2 at the LHC*, arXiv:2008.11556.

[51] F. Archilli, W. Baldini *et al. Performance of the Muon Identification at LHCb*, *JINST* **8** (2013) P10020.

[52] M Anelli, R. A. Nobrega *et al. Performance of the LHCb muon system with cosmic ray*, *JINST* **5** (2010) P10003.

[53] A.A. Alves, Jr., L. Anderlini *et al. Performance of the LHCb muon system, JINST* **8** (2013) P02022.

[54] F. Dordei (on behalf of the LHCb Collaboration), *LHCb detector and trigger performance in Run II, EPJ Web Conf.* **164** (2017) 01016.

[55] I. Bird, *Computing for the Large Hadron Collider*, Annual Review of Nuclear and Particle Science **61** (2011) 99.

[56] LHCb gitlab page of AmpGen, https://gitlab.cern.ch/lhcb/Gauss/tree/master/Gen/AmpGen.

[57] R. Aaij *et al.* (LHCb Collaboration), *Studies of the resonance structure in $D^0 \to K^{\mp}\pi^{\pm}\pi^{\pm}\pi^{\mp}$ decays*, Eur. Phys. J. C **7786**, 443 (2018).

[58] R. Aaij *et al.* (LHCb Collaboration), *Search for CP violation through an amplitude analysis of $D^0 \to K^+ K^- \pi^+ \pi^-$ decays*, JHEP **02** (2019) 126.

[59] R. Aaij *et al.* (LHCb Collaboration), *Studies of the resonance structure in $D^0 \to K_S^0 K^{\pm} \pi^{\mp}$ decays*, Phys. Rev. D **93** 052018 (2016).

[60] N. Pivk, F. R. Le Diberder, *SPlot: A Statistical tool to unfold data distributions*, Nucl. Instrum. Meth. A **555**, 356 (2005).

[61] M Clemenci *et al.*, *The LHCb simulation application, Gauss: Design, evolution and experience,* J. Phys. Conf. Ser. 331 (2011) 032023.

[62] T. Sjöstrand, S. Mrenna, P. Skands, *A brief introduction to PYTHIA 8.1*, Comput.Phys.Commun. **178** (2008) 852.

[63] D.J. Lange, *The EvtGen particle decay simulation package*, Nucl. Instrum. Meth. A **462** , 152 (2001).

[64] S. Agostinelli *et al.* (GEANT4 Collaboration), *GEANT4–a simulation toolkit*, Nucl. Instrum. Meth. A **506**, 250 (2003).

[65] J. Allison, K. Amako, J. Apostolakis *et al.*, *Geant4 developments and applications*, IEEE Trans.Nucl.Sci. **53**, 270 (2006).

[66] S. Taneja, J. L. Cobbledick, private communication, Sep. 2022.

[67] M. D. Cian, S. Farry, P. Seyfert, S. Stahl, *Fast neural-net based fake track rejection in the LHCb reconstruction*, Technical Report: LHCb-PUB-2017-011 ; CERN-LHCb-PUB-2017-011, CERN, Geneva, Mar 2017.

[68] V.V. Gligorov, M. Williams, *Efficient, reliable and fast high-level triggering using a bonsai boosted decision tree, JINST* **8** (2013) P02013.

[69] W. D. Hulsbergen, *Decay chain fitting with a Kalman filter*, Nucl. Instrum. Meth. A **552** , 566 (2005).

[70] D. Berrar, *Cross-validation*, Encyclopedia of Bioinformatics and Computational Biology **1** (2019) 542.

[71] B. P. Roe, H.-J Yang, J. Zhu *et al.*, *Boosted decision trees, an alternative to artificial neural networks*, Nucl. Instrum. Meth. A **543** , 577 (2005).

[72] A. Hoecker, P. Speckmayer, J. Stelzer *et al.*, *TMVA - Toolkit for multivariate data analysis*, arXiv:physics/0703039.

[73] A. Justel, D. Peña, and R. Zamar, *A multivariate Kolmogorov-Smirnov test of goodness of fit*, Statistics & Probability Letters **35(3)**, 251 (1997).

[74] G.J. Gounaris, J.J. Sakurai, *Finite width corrections to the vector meson dominance prediction for $\rho \to e^+e^-$*, Phys. Rev. Lett. **21** 244 (1968).

[75] M.P. Locher, V.E. Markushin, H.Q. Zheng, *Structure of $f_0(980)$ from a coupled channel analysis of S wave $\pi\pi$ scattering*, Eur. Phys. J. C **4**, 317 (1998).

[76] S.U. Chung, J. Brose, R. Hackmann *et al.*, *Partial wave analysis in K matrix formalism*, Annalen Phys. **4**, 404 (1995).

[77] S.-U. Chung, J. Brose, R. Hackmann *et al.*, *K matrix analysis of the $(IJ^{PC} = 00^{++})$-wave in the mass region below 1900 MeV*, Eur. Phys. J. A **16**, 229 (2003).

[78] B. Aubert *et al.* (BaBar Collaboration), *Improved measurement of the CKM angle γ in $B^{\mp} \to D^{(*)}K^{(*\mp)}$ decays with a Dalitz plot analysis of D decays to $K_S^0\pi^+\pi^-$ and $K_S^0K^+K^-$* , Phys. Rev. D **78** 034023 (2008).

[79] S. Weinberg, *Pion scattering lengths*, Phys. Rev. Lett. **17** 616 (1966).

[80] S. L. Adler, *Sum rules for the axial vector coupling constant renormalization in beta decay*, Phys. Rev. **140** B736 (1965).

[81] M. Artuso *et al.* (CLEO Collaboration), *Amplitude analysis of $D^0 \to K^+K^-\pi^+\pi^-$*, Phys. Rev. D **85** 122002 (2012).

[82] G. Bonvicini *et al.* (CLEO Collaboration), *Dalitz plot analysis of the $D^+ \rightarrow K^- \pi^+ \pi^+$ decay*, Phys. Rev. D **78** 052001 (2008).

[83] Y.-H. Chen, D.-L. Yao, and H.-Q. Zheng, *A study of $\rho - \omega$ mixing in resonance chiral theory*, Communications in Theoretical Physics **69** (2018) 50.